Studies on Microscopic Solvation Dynamics for Clusters Containing Metal Atoms/Ions

Masaomi SANEKATA

Doctor of Philosophy

Department of Functional Molecular Science
School of Mathematical and Physical Science
The Graduate University for Advanced Studies

1994

Acknowledgments

The present work was carried out at Instrument Center of Institute for Molecular Science (IMS) in Okazaki, and was achieved under Professor Kiyokazu Fuke. The author would like to express his gratitude to Professor Kiyokazu Fuke for his continuing guidance, encouragement and discussion during this work. The author also wishes to thank Dr. Fuminori Misaizu for his advice and encouragement.

The author is sincerely grateful to Professor Suehiro Iwata of IMS for his continuing interest, suggestions and valuable discussions. The author wishes to acknowledge Professor Kenro Hashimoto of Tokyo Metropolitan University and Mr. Hidekazu Watanabe of the Graduated University for Advanced Studies (GUAS) for their theoretical studies and fruitful discussions.

The author wishes to thank Mr. Norio Okada of National Astronomical Observatory and all members of the Equipment Development Center in IMS for the technical assistance. Special thanks are due to all members of the Instrument Center in IMS and the 3rd term students of the Department of Structural/Functional Molecular Science in GUAS.

Finally, the author is grateful to my family for their support and encouragement over many years.

Masaomi SANEKATA

Contents

Chapter I
General introduction

Preface

Electrons and metal ions in fluids play important roles in many aspects of chemical and biological phenomena and have been the subject of numerous investigations for many years. Although experimental and theoretical studies have attempted to understand the nature and the dynamics of solvation for these species, its microscopic aspect has not yet been fully understood. Recently, advances in molecular beam technique allow us to prepare various kinds of the gas-phase clusters and open new approaches to a microscopic investigation of the excess electrons and metal ions in fluids. The study of successively large clusters is analogous to modeling the process of solvation and provides us information on microscopic solvation. Thus, Cluster research may offer an opportunity to bridge the gap between the gas and condensed phases.

The purpose of this thesis is to investigate the geometrical structure, electronic structure, reactivity, and the energy dissipation process of the clusters containing metal atoms/ions to get information on the dynamics of microscopic solvation process.

In this chapter, first, the backgrounds, problems, and interests for the study on these clusters are described, and secondly, the contents of each chapter are addressed.

I-1. Electrons and metal ions in bulk solution

Studies of the properties of solutions have been recorded since antiquity. However, a concept of solvation as mutual interaction of a solute and a solvent is of much more recent origins in the early 19th century. Since then the solvation process has been the subject of intensive studies, because it is one of the most widespread phenomena on the earth. Many concepts have been established for the solvation phenomena, however, the details are beyond the scope of this chapter.

The solvation of electrons and metal ions has been the central issue among these studies. It has been generally accepted that there is a real boundary between the ion present in the solution surrounding the molecules nearest to it and the remaining mass of the solvent. And also, it is usually assumed that two solvation shells are situated around the ion, namely, the first and the second. The first solvent shell contains the molecules of the solvent in the direct vicinity of the ions, and this shell moves in the solvent together with the ion. The structure of this region is more orderly than the bulk solvent. The number of molecules of the solvent is termed the coordination number of the given ion. The second shell provides an intermediate zone between the first solvent shell and the bulk solvent.

As for the metal-ion solvation, the coordination number and the structure of the first solvent shell have been extensively studied using various spectroscopic methods such as optical spectroscopy, magnetic resonance, dielectric spectroscopy, EXAFS, X-ray diffraction, and neutron diffraction [1]. However, in many cases more than one structural model may be compatible with the data obtained by these method and the structural information are available in limited concentration ranges or for a special region within the time scale of dynamical processes. Perhaps the mass-

spectrometric gas-phase solvation studies may provide the most valuable information as mentioned in the next section.

Electrons in polar fluids have intrigued scientists nearly over 100 years since the first observation of the solvated electrons in liquid ammonia [2]. Injection of electrons into liquid or solid water and ammonia gives rise to a localization of excess electrons in sites, which have been described as clusters of H_2O and NH_3 molecules within the bulk [3]: Though the molecules themselves have no stable negative-ion states. Their broad absorption spectrum and other properties suggest a structure similar to an F-center in alkali halide crystals.

Despite much experimental and theoretical interests, the microscopic structure of these bulk phase states remains unclear. In 1946, Ogg introduced a cavity model to account for a number of observations pertaining to dilute solutions of alkali metals in liquid ammonia [4-7]. In this model, solvated electrons and dielectrons occupy cavities within the solvent, analogous to the F-center known to be single electrons and electron pairs, respectively, occupying anion vacancies in the crystals. This model was widely accepted, however, much of the evidence that Ogg used to support his proposal has turned to be incorrect or unsubstantiated. More recently, solvated solvent-anion complex (SAC) models of solvated electrons have been proposed to account for a number of their properties not adequately accounted for by the cavity model [8-10]. These models are based on the observation that measured paramagnetic shifts of nuclear resonances in dilute alkali metal-ammonia solutions indicate the existence of a large unpaired electron ^{14}N contact interaction [11]; this fact is attributable to solvated electrons in close association with ammonia molecules in spite of the extremely narrow single line observed in the EPR spectrum of the electron. And also, the EPR spectra of $e^-(aq)$ produced by irradiation of ice and glassy mixed-water have found to

contain structural information and typically show an electron environment of 4-6 nearly equivalent H atoms [12]. A hydrated, highly distorted H_2O^- species have been suggested most recently to account for the results of photokinetic experiments on ultrafast time scale [13,14]. Although these studies provided us some insights into the intrinsic nature of solvated electrons, they also indicate implicitly that it seems to be impossible to get a definitive understanding for these issues with the bulk experiments alone. Under these circumstances, a new approach such as the cluster research for the solvated electron seem to be quite informative as mentioned in the next section.

I-2. Cluster researches on solvated electrons and solvated metal ions

Technological advances in the last decade have made possible the intensive exploration of a new realm of matter, to which has now been arisen widespread attention for a variety of reasons. This realm is given various names such as clusters, small particles, etc. depending on one's point of view. Our new ability to explore this intermediate range of matter causes us to reassess our understanding of its limiting forms, molecules or atoms versus bulk solids and liquids. Up to now, the physical and chemical properties of clusters have been extensively investigated for the purpose to bridge the gap between molecular or atomic systems and the condensed phase [15-17]. One of the remarkable aspects of cluster research pertains to the exploration of microscopic solvation phenomena of an electron or a metal ion embedded in a cluster of solvent molecules. The experimental and theoretical studies of such heteroclusters allow for the investigation of specific cluster size effect, i.e., the buildup of the solvation shell in small- and medium sized clusters, and the

exploration of the gradual transition from the finite system to the infinite bulk medium for large clusters. In particular, the microscopic solvation of electrons and metal ions is of central importance for the understanding of the structure, energetics, spectroscopy, dynamics, and reaction kinetics in clusters.

As for the electron solvation, negatively charged free water $(H_2O)_n^-$ (for $n \geq 11$) and ammonia $(NH_3)_n^-$ (for $n \geq 30$) clusters have been recently prepared by localization during the cluster nucleation process or via capture of very low-energy electrons by cold water clusters [18-22]. More recently, the photoelectron spectra of $(H_2O)_n^-$ (for n=2,6,7 and n=2-69) and $(NH_3)_n^-$ (for n=41-1100) have been examined, and vertical detachment energies (VDEs) were determined form the spectra [23,24]. For both systems, the cluster anion VDEs increase smoothly with increasing sizes and depend with $n^{-1/3}$. The VDE ($n=\infty$) value obtained by extrapolation is found to be very close to the photoelectric threshold energy for the corresponding solvated electron system in the condensed phase. After these studies, the excess electron states in these clusters have been examined theoretically by employing the quantum path-integral molecular dynamics method [25-32]. These studies revealed that electron localization in polar molecular clusters occurs via surface or internal modes depending on cluster size and chemical composition, yielding results in agreement with the experimental observations; water cluster anions to be surface states for $n<32$ and internal states for $n>64$, with the transition occurring between n=32-64.

As mentioned in the previous section, the solvated electron was observed traditionally in dilute solutions of alkali metals. Preparation of molecular clusters in supersonic beams allows us to study such aggregates as free species and thus to follow the building up of the liquid phase from its constituents. Recently, the ionization potentials (IPs) of neutral Na [33-35]

and Cs [36-37] atoms embedded in polar molecular clusters were studied by Hertel and his co-workers and also by the present author and his co-workers. Interestingly, for both metal atoms, the limiting value of water clusters for $n \geq 4$ coincides with the estimated IP of an excess electron solvated in bulk water. The details will be described in Chapter III.

As for the metal ion solvation, the gas-phase experiments on cluster ions have been used to study solvent shell structure [38-42]. Accurate characterization of cluster ions properties will help us to develop the fundamental metal ion-neutral interaction potentials needed for structural modeling. Especially for the structural aspects of clusters containing metal and non-metal ions, high-pressure mass spectroscopy (HPMS) was perhaps the first experimental method proved to be successful [38]. These investigations have yielded a wealth of thermodynamic information such as enthalpies, entropies, and free energies of association for ion-neutral complexes. Sharp changes in the enthalpy of association as a function of cluster size were used to infer the number of molecules in the first solvent shell. Since the temperature of the solvated ions is well characterized in the HPMS technique, the results can be readily compared with solution studies or theoretical simulations [43]. However, with successively larger cluster ions, the enthalpy of association rapidly approaches the value of the enthalpy of vaporization of the bulk solvent. This has limited the application of HPMS to solvation studies of ions with small ion radii and low solvation numbers (typically $n \leq 6$).

Although the spectroscopic studies are expected to provide a much more detailed look into the properties of cluster ions, they are quite limited in number. Negative-ion photoelectron spectroscopy of clusters have had a direct impact on the questions concerning the nature of the solvated electron as mentioned previously [23,24]. As for the spectroscopic studies on solvated

metal cluster ions, it is only most recently that measurements of the photoelectron spectra of metal ions (such as Cu^- and Cu_2^-) embedded in water clusters have been made; though the photoelectron spectroscopy was applied for various systems such as metal clusters [44-46], semiconductor clusters [47], and molecular clusters [48]. IR spectroscopy has been also used to study the gas-phase solvation of Cs^+ ion [49-52]. On the other hand, Farrar's and the present author's groups have performed electronic photodissociation experiments on clusters containing monovalent alkaline-earth metal ions [53-62]. In these studies, stabilization of the ion-pair state as a function of the cluster size was examined by photodissociation spectroscopy. For $Sr^+(NH_3)_n$, Farrar and his co-workers discussed the possibility of a Rydberg-type ion pair state from the large redshift of the absorption band. The photodissociation of $Mg^+(H_2O)_n$ and $Ca^+(H_2O)_n$ clusters studied in this thesis provides some clues of the ion-pair state for this system. The details of these studies will be described in Chapter IV-VI.

I-3. Scope for chapters

In order to reveal microscopic aspects of solvation dynamics in fluids, the size-dependent properties of the solvated metal atom clusters and its ions were examined in the present studies. The photoionization experiments for the clusters containing neutral alkali metal atoms and the photodissociation experiments for the clusters containing alkaline-earth metal ions are carried out using a reflectron type time-of-flight mass spectrometer combined with a laser spectroscopic technique. The details of the apparatus and the principles of the mass spectrometry are described in Chapter II. The details for the

experimental methods are described in the experimental section of each chapter.

In Chapter III, the photoionization processes of solvated Cs atom clusters, $Cs(H_2O)_n$, $Cs(NH_3)_n$, and $Cs(CH_3CN)_n$, are discussed in relation to the solvated electrons produced in the dilute alkali atom solution. The ionization potentials (IPs) of these clusters are determined as a function of cluster size. The results show the convergence of IPs to the bulk limits with increasing n. The features of IPs are discussed in conjunction with the ion-pair state formation [36-37].

In Chapter IV and V, the electronic structures and the photodissociation processes of hydrated alkaline-earth metal ions, $M^+(H_2O)_n$ for M=Mg and Ca, are discussed. The photodissociation spectra are found to show a clear evolution of the solvation shell and provide us information on the metal ion-solvent interactions. As for the photodissociation processes, two channels such as the evaporation of water molecules and the photoinduced intracluster reaction to produce the hydrated MOH^+ ions are observed both in the Mg^+-H_2O and Ca^+-H_2O systems [58-60,62].

During the course of these studies, an anomalous product distribution is found to occur for the $M^+ + (H_2O)_n$ (M=Mg and Ca) reactions. Both the $M^+(H_2O)_n$ and $MOH^+(H_2O)_{n-1}$ ions are produced with characteristic size distribution; the product switchings are observed at two critical sizes. In Chapter VI, the dynamics of the reaction and the mechanism for the product switching are discussed on the basis of the results for the photodissociation experiments [61].

References for Chapter I

[1] B. E. Conway, *Ionic Hydration in Chemistry and Biophysics* (Elsevier, Amsterdam 1981).

[2] C. A. Kraus, *J. Am. Chem. Soc.* **30**, 1323 (1908).

[3] J. W. Boag and E. J. Hart, *J. Am. Chem. Soc.* **84**, 4090 (1962).

[4] R. A. Ogg, Jr., *Phys. Rev.* **69**, 668 (1946).

[5] R. A. Ogg, Jr., *Phys. Rev.* **69**, 243; 544 (1946).

[6] R. A. Ogg, Jr., *J. Am. Chem. Soc.* **68**, 155 (1946).

[7] R. A. Ogg, Jr., *J. Chem. Phys.* **14**, 295 (1946).

[8] D. -F. Feng and L. Kevan, *Chem. Rev.* **80**, 1 (1980).

[9] H. F. Hameka, G. W. Robinson, and C. J. Marsden, *J. Phys. Chem.* **91**, 3150 (1987).

[10] T. R. Tuttle, Jr. and S. Golden, *J. Phys. Chem.* **95**, 5725 (1991).

[11] S. Golden, C. Guttman, and T. R. Tuttle, Jr., *J. Chem. Phys.* **44**, 3791 (1966).

[12] L. Kevan, *Acc. Chem. Res.* **14**, 138 (1981).

[13] J. C. Alfano, P. K. Walhout, Y. Kimura, and P. F. Barbara, *J. Chem. Phys.* **98**, 5996 (1993).

[14] Y. Kimura, J. C. Alfano, P. K. Walhout, and P. F. Barbara, *J. Phys. Chem.* **98**, 3450 (1994).

[15] A. W. Castleman, Jr. and R. G. Keesee, *Science* **241**, 36 (1988).

[16] J. Jortner, *Ber. Bunsenges. Phys. Chem.* **88**, 188 (1984).

[17] *Physics and Chemistry of Small Clusters*, edited by P. Jena, B. K. Rao and S. N. Khanna, vol. **158** of *NATO ASI Series B* , (Plenum, New York, 1987).

[18] H. Haberland, C. Ludewigt, H. -G. Schindler and D. R. Worksnop, *Surf. Sci.* **156**, 157 (1985).

[19] H. Haberland, H. -G. Schindler and D. R. Worksnop, *J. Chem. Phys.* **81**, 3742 (1984).

[20] M. Knapp, O. Echt, D. Kreisle, and E. Recknagel, *J. Chem. Phys.* **85**, 636 (1986).

[21] M. Knapp, O. Echt, D. Kreisle, and E. Recknagel, *J. Phys. Chem.* **91**, 2601 (1987).

[22] H. Haberland, H. -G. Schindler and D. R. Worksnop, *Ber. Bunsenges. Phys. Chem.* **88**, 270 (1984).

[23] J. V. Coe, G. H. Lee, J. G. Eaton, H. W. Sarkas, K. H. Bowen, C. Ludewigt, H. Haberland and D. R. Worsnop, *J. Chem. Phys.* **92**, 3980 (1990).

[24] G. H. Lee, S. T. Arnold, J. G. Eaton, H. W. Sarkas, and K. H. Bowen, *Z. Phys.* D **20**, 9 (1991).

[25] R. N. Barnett, U. Landman, C. L. Cleaveland, and J. Jortner, *Phys. Rev. Lett.* **59**, 811 (1987).

[26] R. N. Barnett, U. Landman, C. L. Cleaveland, and J. Jortner, *J. Chem. Phys.* **88**, 4421, 4429 (1987).

[27] U. Landman, R. N. Barnett, C. L. Cleaveland, D. Scharf, and J. Jortner, *J. Phys. Chem.* **91**, 4890, (1987).

[28] R. N. Barnett, U. Landman, C. L. Cleaveland, N. R. Kestner and J. Jortner, *J. Chem. Phys.* **89**, 6670 (1988).

[29] R. N. Barnett, U. Landman, C. L. Cleaveland, N. R. Kestner and J. Jortner, *Chem. Phys. Lett.* **148**, 249 (1988).

[30] R. N. Barnett, U. Landman, and A. Nitzan, *J. Chem. Phys.* **89**, 2242 (1988).

[31] R. N. Barnett and U. Landman, *Phys. Rev. Lett.* **70**, 1775 (1993).

[32] G. J. Martyna and M.L. Klein, *J. Chem. Phys.* **96**, 7662 (1992).

[33] C. P. Schulz, R. Haugstätter, H. -U. Tittes and I. V. Hertel, *Phys. Rev. Lett.* **57**, 1703 (1986).

[34] C. P. Schulz, R. Haugstätter, H. -U. Tittes and I. V. Hertel, *Z. Phys.* D**10**, 279 (1988).

[35] I. V. Hertel, C. Hüglin, C. Nitsch and C. P. Schulz, *Phys. Rev. Lett.* **67**, 1767 (1991).

[36] F. Misaizu, K. Tsukamoto. M. Sanekata, and K. Fuke,*Chem. Phys. Lett.* **188**, 241 (1992).

[37] K. Fuke, M. Misaizu, K. Tsukamoto, and M. Sanekata, In *Physics and Chemistry of Finite Systems*; edited by P. Jena, S. N. Khanna, and B. K. Rao, Vol. **II**, pp 925 (Kluwer, Dordrecht, 1992).

[38] P. Kebarle, *Ann. Rev. Phys. Chem.* **28**, 445 (1977).

[39] T. D. Mark and A. W. Castleman, Jr., *Adv. Rev. Mol. Phys.* **20**, 65 (1986).

[40] R. G. Keesee and A. W. Castleman, Jr.,*J. Phys. Chem. Ref. Data.* **15**, 1011 (1986).

[41] P. B. Armentrout, *Ann. Rev. Phys. Chem.* **41**, 313 (1990).

[42] E. J. Bieske and J. P. Maier, *Chem. Rev.* **93**, 2603 (1993).

[43] E. Kochanski and E. Constantin, *J. Chem. Phys.* **87**, 1661 (1987).

[44] J. Hoe, K. M. Ervin, and W. C. Lineberger, *J. Chem. Phys.* **93**, 6987 (1990).

[45] G. Gantefer, M. Gansa, K. -H. Meiwes-Broer, and H. O. Lutz, *J. Chem. Soc. Faraday Trans.* **86**, 2483 (1990).

[46] O. Cheshnovsky, K. J. Taylor, J. Conceicao, and R. E. Smalley, *Phys. Rev. Lett.* **64**, 1785 (1990).

[47] S. H. Yang, C. L. Pettiette, J. Conceicao, O. Cheshnovsky, and R. E. Smalley, *Chem. Phys. Lett.* **139**, 233 (1987).

[48] L. A. Posey and M. A. Johnson, *J. Chem. Phys.* **88**, 5383 (1988).

[49] W. -L. Liu and J. M. Lisy, *J. Chem. Phys.* **89**, 605 (1988).

[50] J. A. Draves, Z. Luthey-Schulten, W. -L. Liu, and J. M. Lisy, *J. Chem. Phys.* **93**, 4589 (1990).

[51] F. Huisken and A. Kulcke, C. L. Laush, and J. M. Lisy, *J. Chem. Phys.* **95**, 3924 (1991).

[52] T. S. Selegue, N. Moe, J. A. Draves, and J. M. Lisy, *J. Chem. Phys.* **96**, 7268 (1992).

[53] M. H. Shen, J. W. Winniczek, and J. M. Farrar, *J. Phys. Chem.* **91**, 6447 (1987).

[54] M. H. Shen and J. M. Farrar, *J. Phys. Chem.* **93**, 4386 (1989).

[55] M. H. Shen and J. M. Farrar, *J. Chem. Phys.* **94**, 3322 (1991).

[56] S. G. Donnelly and J. M. Farrar, *J. Chem. Phys.* **98**, 5450 (1993).

[57] C. A. Schumuttenmaer, J. Quan, S. G. Donnelly, M. J. DeLuca, D. F. Varley, L. A. DeLouise, R. J. D. Miller, and J. M. Farrar, *J. Phys. Chem.* **98**, 3077 (1993).

[58] F. Misaizu, M. Sanekata, K. Tsukamoto, K. Fuke, and S. Iwata, *J. Phys. Chem.* **96**, 8259 (1992).

[59] K. Fuke, F. Misaizu, M. Sanekata, K. Tsukamoto, and S. Iwata, *Z. Phys.* D**26**, S180 (1993).

[60] F. Misaizu, M. Sanekata, K. Fuke, and S. Iwata, *J. Chem. Phys.* **100**, 1161 (1994).

[61] M. Sanekata, F. Misaizu, and K. Fuke, *J. Am. Chem. Soc.*, in press.

[62] M. Sanekata, F. Misaizu, and K. Fuke, to be submitted.

Chapter II
Experimental

II-1. Vacuum chamber

Figure II-1 shows an experimental apparatus used in the present study. It consists of three-stage differentially evacuated chambers which contain a cluster source and a reflectron time-of-flight (TOF) mass spectrometer with static or pulsed extraction fields. The first chamber, where the cluster beam source is placed, is composed of the 400×400×400 mm rectangular stainless steel and is evacuated with two 10 in. bore diffusion pumps (ULVAC, ULK-10A; 3000 l/s) backed with a mechanical booster pump (ULVAC YM-300). The background pressure in this chamber is typically 1×10^{-6} Torr. The second chamber containing ion optics is composed of the 400×400×600 mm rectangular stainless steel is evacuated with a 250 mm bore diffusion pump (Edwards, Diffstak250; 2000 l/s) backed with a mechanical booster pump (ULVAC YM-100C). The cluster beam is collimated with a skimmer (ϕ1~5 mm) placed between the first and second chambers. The background pressure in the second chamber is typically ~5×10^{-7} Torr. The last chamber which is the flight tube of the reflectron TOF mass spectrometrer tube is 800 mm in length and evacuated with a 100 mm bore diffusion pump (Edwards, Diffstak100; 280 l/s) backed with a rotary pump (ULVAC D-330D). The background pressure in the last chamber is typically 5×10^{-8} Torr. The total flight length of the ions traveling from the extraction grid to a dual MCP detector is ca. 2000 mm. The principle of the reflectron TOF mass spectrometer is described in next sections. Details of the cluster sources and

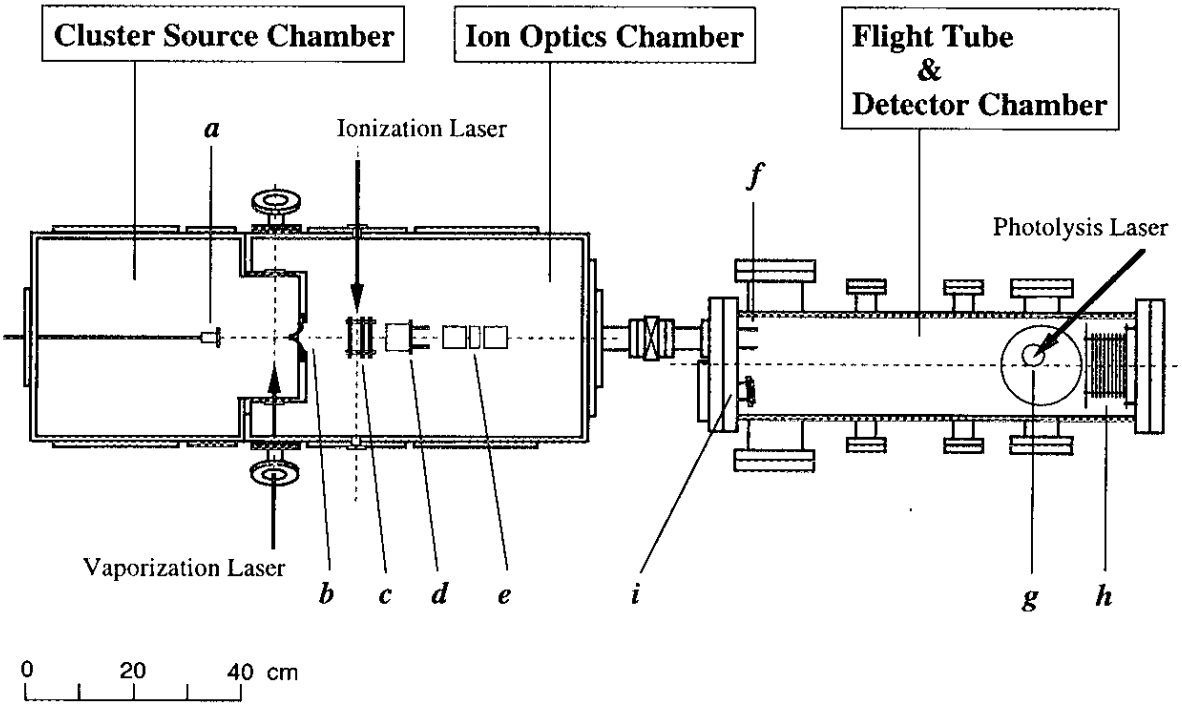

Figure II-1. Schematic top view of the experimental appratus. The diagram shows the reflectron type time-of-flight mass spectrometer used for photoionization and photodissociation spectroscopy. The compornents of the instrument are as follows: (*a*) pulsed nozzle, (*b*) skimmer, (*c*) extraction electrodes, (*d*) deflector-1, (*e*) einzel lens, (*f*) deflector-2, (*g*) spatial focal point, (*h*) ion reflector, (*i*) detector.

measurement procedures are described in the experimental section of each chapter.

II-2. Reflectron time-of-flight (TOF) mass spectrometer

The reflectron TOF mass spectrometer is composed of the following parts; the double acceleration region which was firstly developed by Wiley and McLaren [1], the first field-free ion drift region with ion deflectors and einzel lens, the ion deceleration and reflection regions, the second drift region for the reflected ions, and the microchannel plate detector. The principle of the TOF mass spectrometer, which was firstly reported in 1948 [2], is quite simple. The bunch of ions entering into or produced at the source region is accelerated with a single, constant electric field, E, in the source region with s in length. The ions with a constant translational energy are introduced to a field free region with l in length. A TOF, t, of an ion with mass M and charge e from the source region to the detector is given by

$$t = \left(\sqrt{\frac{2s}{eE}} + \frac{l}{\sqrt{2eE}} \right) \cdot \sqrt{M} . \qquad \text{(II.1)}$$

The mass, M, is proportional to t^2 and thus can be determined from the observed TOF according to eq.(II.1). The resolution, R, of the mass spectrometer is defined by the maximum mass number that can be resolved with an unit mass. By using eq. (II.1), R can be expressed as

$$R = \frac{t_R}{2\Delta t}, \qquad \text{(II.2)}$$

where t_R is the TOF of the ion with mass R and Δt is the difference between the TOF of mass R and R+1.

II-2.1. Principle of Wiley-McLaren type TOF mass spectrometer

Although the single-acceleration-field mass spectrometer firstly developed has several advantages, for example, (1) obtainable mass range is unlimited, and (2) the total mass spectrum is obtained with high efficiency in short acquisition times, it has one inevitable defect of the poor mass resolution. This problem is caused by the two factors: the spatial and the velocity distributions of ions in the source region. It has turned out that the former factor in this problem is resolved by using a Wiley-McLarlen type TOF mass spectrometer with double-electric fields [1]. In the double acceleration system as illustrated in Figure II-2, the ions are accelerated by two independent electric fields, E_s and E_d, in the regions given s and d in length, respectively. The total TOF, t, is the sum of the TOFs, t_s, t_d, and t_l, of each region, s, d, and l, respectively, i.e.,

$$t = t_s + t_d + t_l. \tag{II.3}$$

The TOF of each region is

$$t_s = \sqrt{\frac{2M}{e}} \cdot \sqrt{\frac{s}{E_s}}, \tag{II.4}$$

$$t_d = \sqrt{\frac{2M}{e}} \cdot \frac{1}{E_d}(\sqrt{U} - \sqrt{sE_s}), \tag{II.5}$$

and

$$t_l = \sqrt{2M} \cdot \frac{l}{2\sqrt{U}}, \tag{II.6}$$

where U is the total acceleration voltage expressed as

$$U = sE_s + dE_d, \tag{II.7}$$

under the approximation that the initial velocity of the ions are equal to zero. The condition of space focusing, which is defined by the condition that the ions with spatial distribution in the source reach the detector with minimum time distribution in the first order, is obtained by

$$\left(\frac{dt}{ds}\right)_{s=s_0} = 0, \tag{II.8}$$

where s_0 is the average first acceleration length of ions, which is typically equal to the half of the length between the first and second acceleration plates (see Figure II-2). From eqs. (II.3)-(II.8), we obtain the relation,

$$l = 2s_0 k_0^{3/2}\left[1 - \frac{d}{s_0\left(k_0 + k_0^{1/2}\right)}\right], \tag{II.9}$$

where

$$k_0 = (s_0E_s + dE_d) / s_0E_s. \tag{II.10}$$

In the design for the double-acceleration TOF mass spectrometer, the parameters of the mass spectrometer are given by eq.(II.9): The parameters are the strengths of the acceleration fields, E_s and E_d, the distance between the first and second acceleration plates, $2s_0$ and d, and the total flight length of ions, l.

II-2.2. Principle of reflectron type TOF mass spectrometer

The second factor of the problem that limits the resolution in the TOF mass spectrometer, i.e., the velocity distribution of ions, has been overcome

by using the reflectron TOF mass spectrometer [3-5]. The mass resolution is highly improved by using an ion reflector which is able to compensate an initial ion-velocity distribution originated in a cluster source, and this mass spectrometer has turned out to be useful for the cluster research. The reflectron mass spectrometer has another intrinsic advantages that it can be operated as a tandem type TOF mass spectrometer. For example, the masses of the fragment ions produced by the photodissociation of size-selected cluster ions in the first drift region can be resolved in the reflection region and the second field-free regions.

Schematic diagram of the reflectron TOF mass spectrometer is shown in Figure II-2. In this mass spectrometer, an ion reflector is placed between the Wiley-McLaren type mass spectrometer and the detector. Two electric fields, the deceleration and eflection fields, are applied in the ion reflector. The potential differences and interelectrode distances are U_T and d_T for the electric field of deceleration, and U_K and d_K for the field of reflection, respectively. The reflection grids consist of 17 guiding plates, which are placed at regular intervals and interconnected by resistors in order to make a uniform electric field.

The trajectories of ions in the ion reflector are schematically shown in Figure II-3. The principle of the energy focusing in the reflectron TOF mass spectrometer, defined by the condition that the ions with energy distribution reach the detector with minimum time spread up to the second order, can be visualized in the extreme case as shown in the figure. Consider the pair of ions with the same mass, M, and the same initial kinetic energy, $e\delta U$, but with the opposite direction of velocity; one has a velocity with a direction to the drift region and the other with an opposite direction. In the first field free region, l, the ions have different kinetic energies, $e(U_0+\delta U)$ and $e(U-\delta U)$, respectively. The difference in arrival times to a detector is decreased by

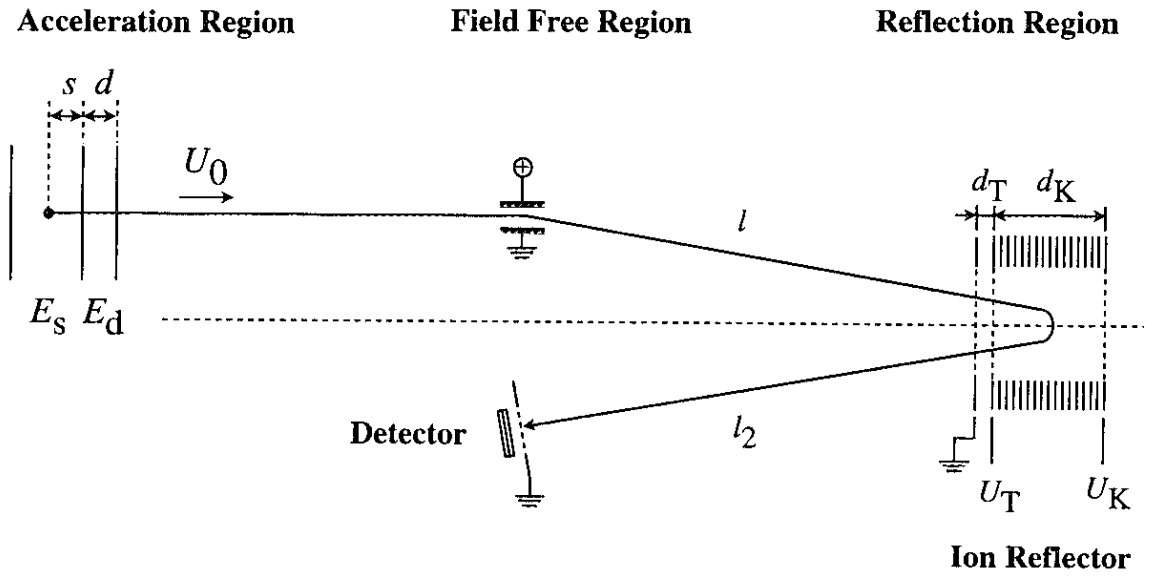

Figure II-2. Geometry and parameters of the reflectron type time-of-flight mass spectrometer. These parameters in this figure are noted in the text.

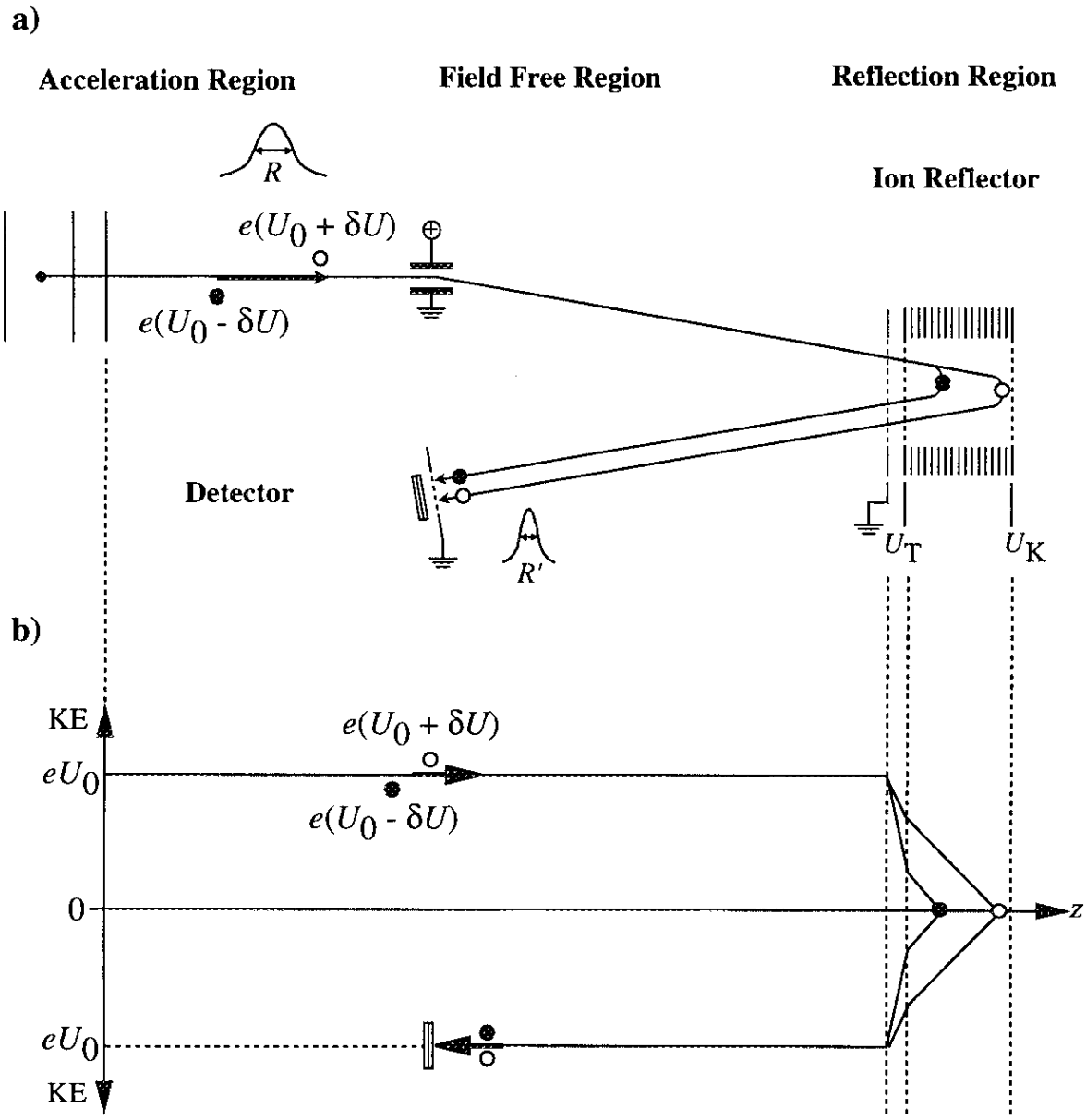

Figure II-3. (a) Schematic drawing of the different trajectories of ions with the kinenetic energies, $e(U_0+\delta U)$ and $e(U_0-\delta U)$, respectively. (b) The electric field potentials as seen by ions. The turning points depend on the final kinetic energy of the ion and the electric potentials applied.

optimizing the condition of electric fields, so as to the one ion with $e(U_0+\delta U)$ turns back at a deeper point in the ion reflector, and so as to the another ion with $e(U_0-\delta U)$ turns back at a shallower point.

The time-of-flight of the ions after acceleration, t, in Figure II-2 is written by the sum of the TOFs of the first and second drift region, t_L, of the deceleration region, t_T, and of the reflection region t_K, i.e.,

$$t = t_L + t_T + t_K . \tag{II.11}$$

Consider the condition that the energy of the accelerated ions, eU, has a distribution with an average energy of eU_0. The TOFs of the three regions are written as

$$t_L = \frac{L}{\sqrt{2eU_0/M}} \cdot \frac{1}{\sqrt{k}}, \tag{II.12}$$

$$t_T = \frac{4d_T}{\sqrt{2eU_0/M}} \cdot \frac{U_0}{U_T} \cdot \left(\sqrt{k} - \sqrt{k - \frac{U_T}{U_0}} \right), \tag{II.13}$$

and

$$t_K = \frac{4d_K}{\sqrt{2eU_0/M}} \cdot \frac{U_0}{U_K} \cdot \left(\sqrt{k - \frac{U_T}{U_0}} \right), \tag{II.14}$$

where k is a factor defined by $k=U/U_0$, and L is total length of the two field free regions, i.e., $L=l+l_2$. The energy focusing condition is expressed as

$$\left(\frac{dt}{dU} \right)_{U=U_0} = 0, \tag{II.15}$$

and

$$\left(\frac{d^2t}{dU^2}\right)_{U=U_0} = 0. \qquad \text{(II.16)}$$

From eqs. (II.11-16) we obtain

$$\frac{L}{4d_K}\cdot\frac{U_K}{U_0} \approx \sqrt{3}, \qquad \text{(II.17)}$$

and

$$\frac{U_T}{U_0} \approx \frac{2}{3}. \qquad \text{(II.18)}$$

II-2.3. Experimental parameters of the reflectron TOF mass spectrometer used in the present study

The geometrical parameters of our homemade reflectron TOF mass spectrometer are as follows:

s_0=10 mm,
d=10 mm,
$L=l+l_2$=2000 mm,
l=1400 mm; l_2=600 mm,
d_T=12 mm; d_K=100 mm.

In the typical experimental condition for the observation of the mass spectrum of the ions initially produced in a cluster source, the source paramerters after optimization are as follows;

E_s=200 V/cm,

E_d=2900 V/cm,

and

U_0=3100 V.

Under this condition, the plane of the space focusing is estimated to be 116 cm from the end of acceleration region, by using eq.(II.9). In the present apparatus, the focal point under a thin condition lies just in front of the the ion reflector, where the photolysis laser is crossed with the ion beam at this point in the photodissociation studies. In fact, this condition is suitable for the photodissociation experiment: The parent ions efficiently interact with photons as a result of focusing. The electric potentials of the ion reflector can also be determined from eqs.(II.17) and (II.18) as

U_T (calc) =1074 V

and

U_K(calc) =3141 V.

These parameters are optimized experimentally as

U_T(exp)=960 V

and

U_K(exp)=3280 V.

These results show the validity of the consideration of the mass resolution noted in Sections II-2.2 and II-2.3. Under these conditions, the mass resolution, R, of ca. 800 is achieved. A typical mass spectrum obtained with these conditions is shown in Figure IV-3.

References for Chapter II

[1] W. C. Wiley and I. H. McLaren, *Rev. Sci. Instrum.* **26**, 1150 (1955).

[2] A. E. Cameron and D. F. Eggers, Jr., *Rev. Sci. Instrum.* **19**, 605 (1948).

[3] V. I. Karataev, B. A. Mamyrin, and D. V. Shmikk, *Sov. Phys. -Tech. Phys.* **16**, 1177 (1972).

[4] B. A. Mamyrin, V. I. Karataev, D. V. Shmikk, and V. A. Zagulin, *Sov. Phys. JETP* **37**, 45 (1973).

[5] H. Shinohara, *Shitsuryo bunseki* **38**, 43 (1990).

Chapter III

Photoionization of solvated alkali atom clusters

III-1. Introduction

Electrons in fluids play important roles in many aspects of chemical phenomena and have been the subject of numerous investigations [1,2]. Especially, the process of excess electron solvation in the alkali metal-polar solvent systems have been one of the central issues. Experimental and theoretical studies have attempted to understand the nature of solvated electrons and the dynamics of electron solvation in these systems. However, the microscopic aspect of solvated electrons has not yet been fully understood.

Advances in molecular beam techniques have opened new approaches to a microscopic investigation of the excess electrons in fluids. Recently, negatively charged water and ammonia clusters, $(H_2O)_n^-$ and $(NH_3)_n^-$, were prepared via capture of low-energy electrons by solvent clusters [3-7]. The vertical detachment energies were obtained for $(H_2O)_n^-$ and $(NH_3)_n^-$ with n up to $\approx$ 70 [6,7]. The excess electron states were also examined using quantum pass integral molecular dynamics simulations [8,9]. On the other hand, Hertel and his co-workers have prepared prototypes such as solvated sodium atom clusters, i.e. $Na(H_2O)_n$ and $Na(NH_3)_n$ [10-12], which enable us to link the macroscopic to microscopic properties of alkali metal-solvent systems. In analogy to the bulk behavior of an alkali atom in polar fluids [1,2], the valence electron of the alkali metal atom is transferred to a solvent cluster with sufficiently large n, and the ground state may have an ion-pair character. Therefore, the electron-photoejection threshold as a function of n

is expected to include size-dependent information on the stability of the solvated atom, and also, on the excess electron state in clusters.

In this chapter, I present the results on the photoionization-threshold measurements of $Cs(NH_3)_n$ ($n \leq 31$), $Cs(H_2O)_n$ and $Cs(CH_3CN)_n$ with $n \leq 21$. In the bulk, solvent molecules used here have distinct characteristics in dissolving the alkali atom and stabilizing excess electrons. In bulk ammonia and water, the alkali metal is dissolved and produces stable solvated electrons. In the case of acetonitrile, the dimer-radical anion has been reported to be a stable species instead of the solvated electron. These three clusters examined in this study are found to show individual features in the size dependence of the ionization thresholds. The features are discussed in connection with the stability of the excess electron in molecules, clusters, and the bulk phases of these solvents.

III-2. Experimental

III-2.1. Pickup cluster source

The pickup-type cluster source was used to produce solvated Cs atom clusters. The cluster source was composed of two pulsed valves arranged at right angles [11]. The pulsed valve for Cs-atom beam is a modified fuel injector suitable for high-temperature experiments up to 500 °C. A cross-section of the valve is shown in Figure III-1. The spring and the parts 10, 11, 12, and 13 were taken from the original fuel injector. The driving solenoid is protected from heat by a water jacket mounted on the main tube. Figure III-2 illustrates the setup of the cluster source used. Solvent molecular clusters were produced by supersonic expansion of 2 atm Ar gas mixed with the sample gas from the first pulse valve (General Valve, series 9) at room

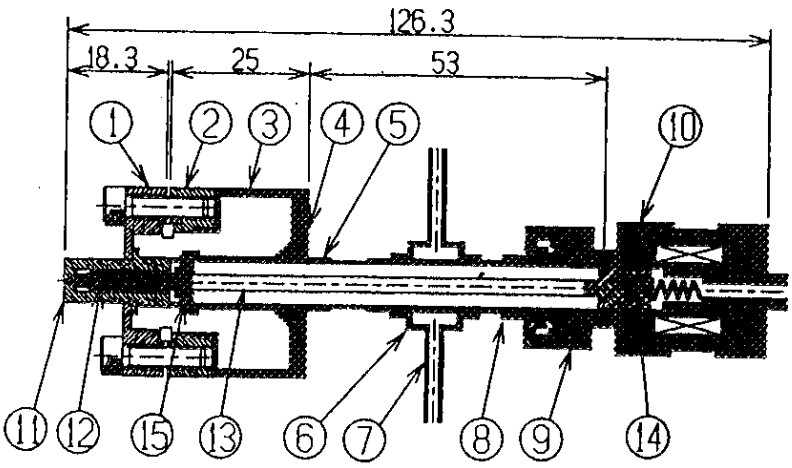

Figure III-1. Cross-section of high temperature pulsed valve.

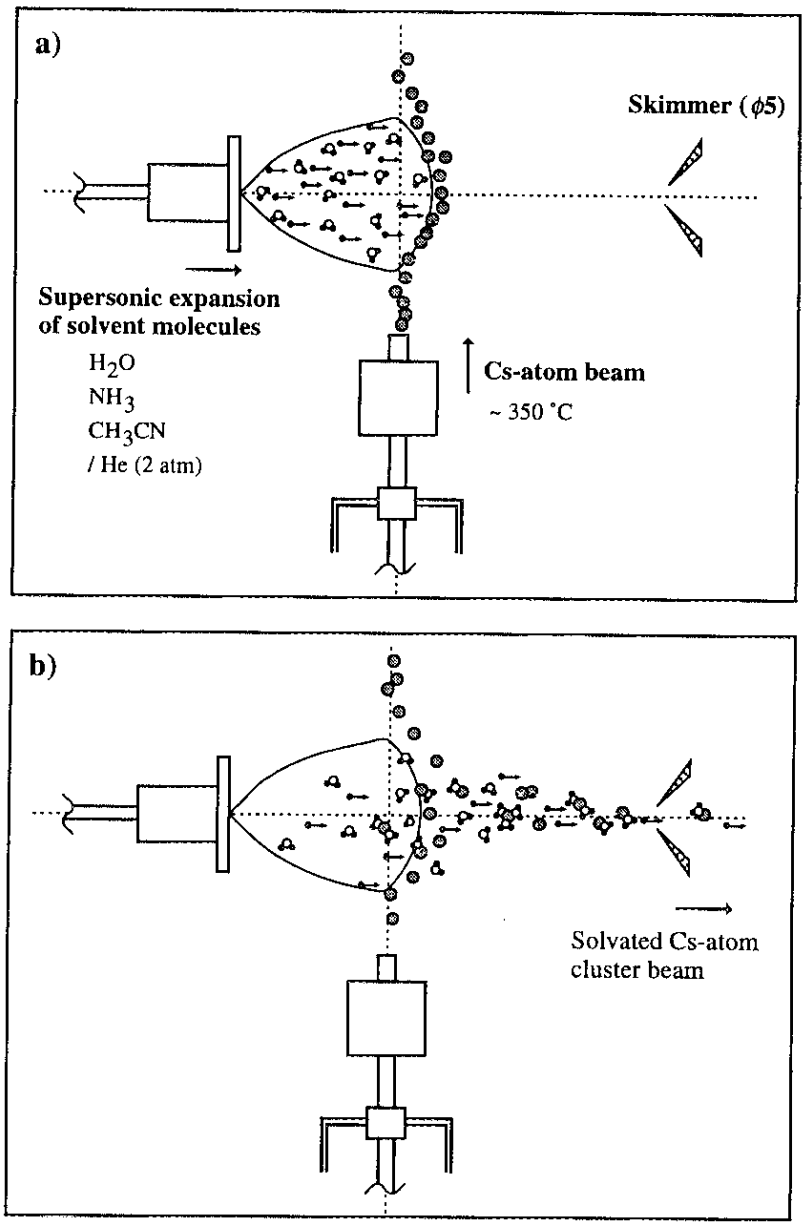

Figure III-2. Schematic drawings of the pickup-type cluster source and schematic snapshots for the formation of the solvated Cs atom clusters: (a) Immediately after opening of the pulsed valve for the solvent molecules; (b) a few μs later. Cs atoms: (●); Solvent molecules: (●); Ar atoms: (●).

temperature. A pulsed Cs-atom beam was formed by expansion of neat vapor from the second valve which was heated to about 350 °C. The Cs-atom beam was injected at 10-15 mm downstream from the first nozzle. Solvated Cs clusters, CsS_n (S = H_2O, NH_3, and CH_3CN), produced by subsequent multiple collisions (see Figure III-2), were collimated with a skimmer (ϕ1~5 mm) and introduced into the mass spectrometer.

III-2.2. Experimental setup

Details of the experimental apparatus used in the present study are shown in Chapter II. The system consists of a three-stage differentially evacuated chamber which includes a cluster source and a reflection type time-of-flight (TOF) mass spectrometer. Figure III-3 shows a block diagram of the apparatus used in the present study. Solvated Cs clusters produced by the pickup source were ionized by crossing an excimer-pumped dye laser (Lambda Physik, EMG103/FL2002) 250 mm downstream from the first nozzle. The laser power was attenuated to less than 1 mJ/pulse in order to avoid multiphoton ionization. Cluster ions produced were accelerated at right angles to the incident neutral beam and introduced to the field-free region of the reflectron TOF mass spectrometer. The ions were reflected by electric fields at the end of the TOF chamber and were detected by dual microchannel plates (Hamamatsu, F1552-23S) after flying back into the field-free region. The output signals were fed into a digital storage oscilloscope (LeCroy 9450) after being amplified by a wide-band amplifier (NF Electronic Instruments, BX-31).

Mass spectra were obtained by scanning the photon energy with an interval of 0.03 eV in the region 3.65-2.14 eV (340-580 nm). The ionization thresholds were determined within ±0.06 eV by analyzing the mass spectra.

The error caused by field ionization is estimated to be about 0.01 eV in the present experimental conditions.

The cesium sample (Rare Metallic Co., 99.95 %) was filled into the pulse valve under nitrogen atomosphere without further purification. Ammonia gas (Nippon Sanso, 99.99 %) was mixed with Ar gas in a stainless-steel reservoir. Liquid samples were placed in a reservoir where Ar gas was bubbled at room temperature. Water was used after distillation and ion exchange. Acetonitrile (Wako, >99%) was used without further purification.

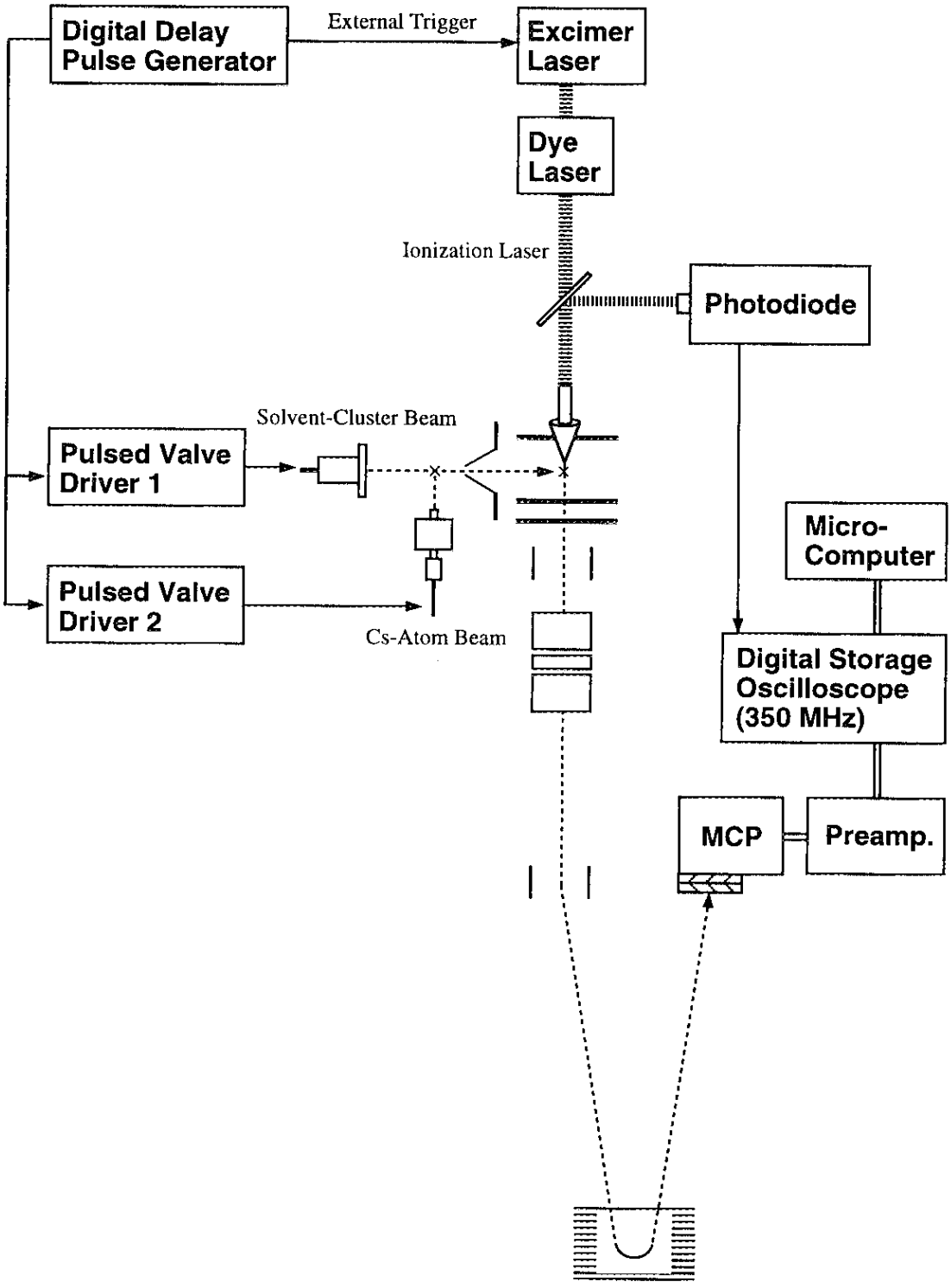

Figure III-3. Block diagram of the laser system and the measurement devices for the study of photoionization of solvated alkali atom clusters.

III-3. Results

III-3.1. $Cs(H_2O)_n$ clusters

The typical photoionization mass spectra of $Cs(H_2O)_n$ clusters are shown in Figures III-4a and III-4b. These spectra were obtained at the laser wavelength of 360 nm. No evaporation of constituent H_2O molecules from the cluster is expected after ionization at this photon energy. An anomalously enhanced peak is observed at n=20 (Figure III-4b). This magic number agrees with the enhanced stabilities observed in the mass spectra of $H_3O^+(H_2O)_n$ [13,14] and $NH_4^+(H_2O)_n$ [15]. The ionization potential thresholds, IP(n), determined for n=1-21 are plotted in Figure III-5a as a function of $(n+1)^{-1/3}$, which is approximately inversely proportional to the cluster radius (see Appendix). However, IP(n) is almost constant at 3.12 eV for n=4-21. This constant IP value, which agrees with that of $Na(H_2O)_n$ [11], is nearly equal to the bulk limit of the vertical detachment energies (VDEs) determined by the photoelectron spectroscopy of $(H_2O)_n^-$ [6].

III-3.2. $Cs(NH_3)_n$ clusters

Figure III-4c shows a typical one-photon ionization mass spectrum of $Cs(NH_3)_n$ clusters obtained by irradiation of a XeCl laser beam of 308 nm. Cluster ions, $Cs(NH_3)_n$, were observed up to n=50. A step in the size distribution at $n\approx10$ is observed at any laser wavelength between 308 and 480 nm. This step may correspond to the filling of the first coordination shell around the cesium atom according to the theoretical work by Klein and his co-workers [16]. Figure III-5b shows IP(n) versus $(n+1)^{-1/3}$ plots determined by changing the ionization laser wavelength. The observed IP(n) value coincides closely with a theoretically predicted one [17] for n=1, though it is higher for n=4, 6 and 8. The features of the IP(n) versus $(n+1)^{-1/3}$ plots

observed for $Cs(NH_3)_n$ are rather different from those for $Cs(H_2O)_n$. IP(n) decreases almost linearly with $(n+1)^{-1/3}$ for $n \geq 3$. The intercept of the fitted line at $(n+1)^{-1/3}=0$ ($n \rightarrow \infty$) is 1.4 eV. This value, which agrees also in this case with the results of a photoionization experiment for $Na(NH_3)_n$ [12], is higher than the heat of solution of the electron in liquid ammonia, 0.99 eV [18,19], which is determined thermodynamically. Instead, it coincides with the intercept value from the fitted line of VDEs for $(NH_3)_n^-$ [7].

III-3.3. $Cs(CH_3CN)_n$ clusters

In contrast to the case of ammonia- and water-solvated clusters, the IP(n) values determined for $Cs(CH_3CN)_n$ show an anomalous dependence upon $(n+1)^{-1/3}$ for $n \leq 11$, as shown in Figure III-5c. The IP(n) values for n=2 and 3 are lower than those for n=4-6, and the value for n=9 is lower than those for n =10 and 11. For n=12-21, the IP(n) versus $(n+1)^{-1/3}$ plots show a plateau behavior, as observed for $Cs(H_2O)_n$ ($n \geq 4$), and give a constant value of 2.40 eV.

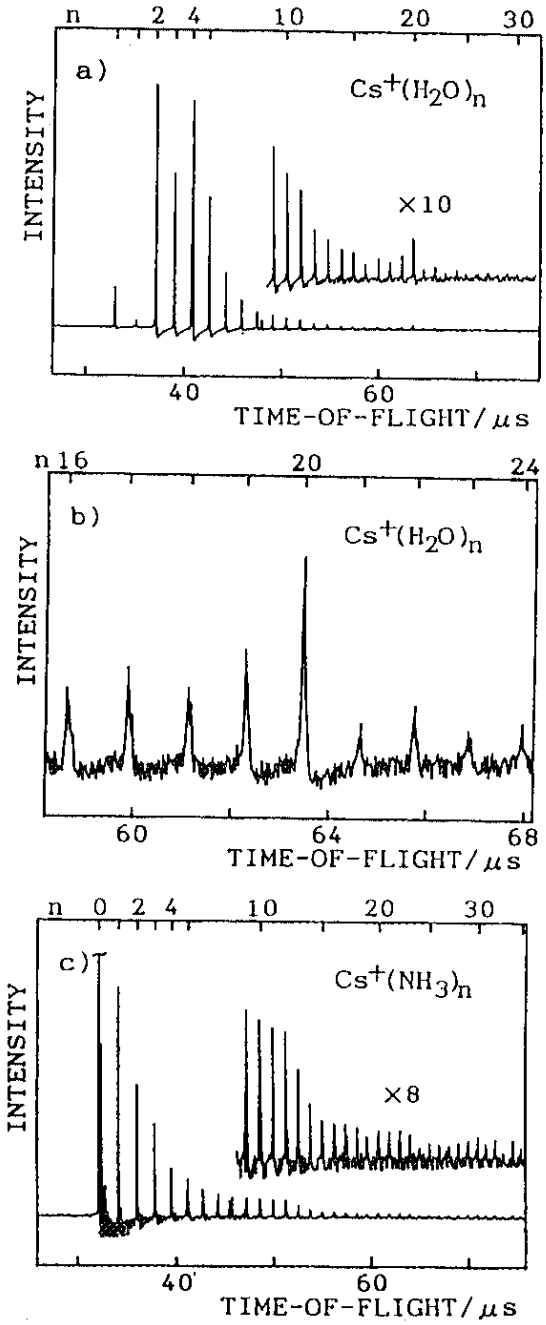

Figure III-4. Typical photoionization mass spectra of solvated Cs atom clusters. (a) $Cs(H_2O)_n$ with n up to 30. Ionization laser wavelength (λ) is 360 nm. (b) $Cs(H_2O)_n$ with n around 20. λ=360 nm. An outstanding peak is observed at $n = 20$. (c) $Cs(NH_3)_n$ with n up to 35. $\lambda = 308$ nm.

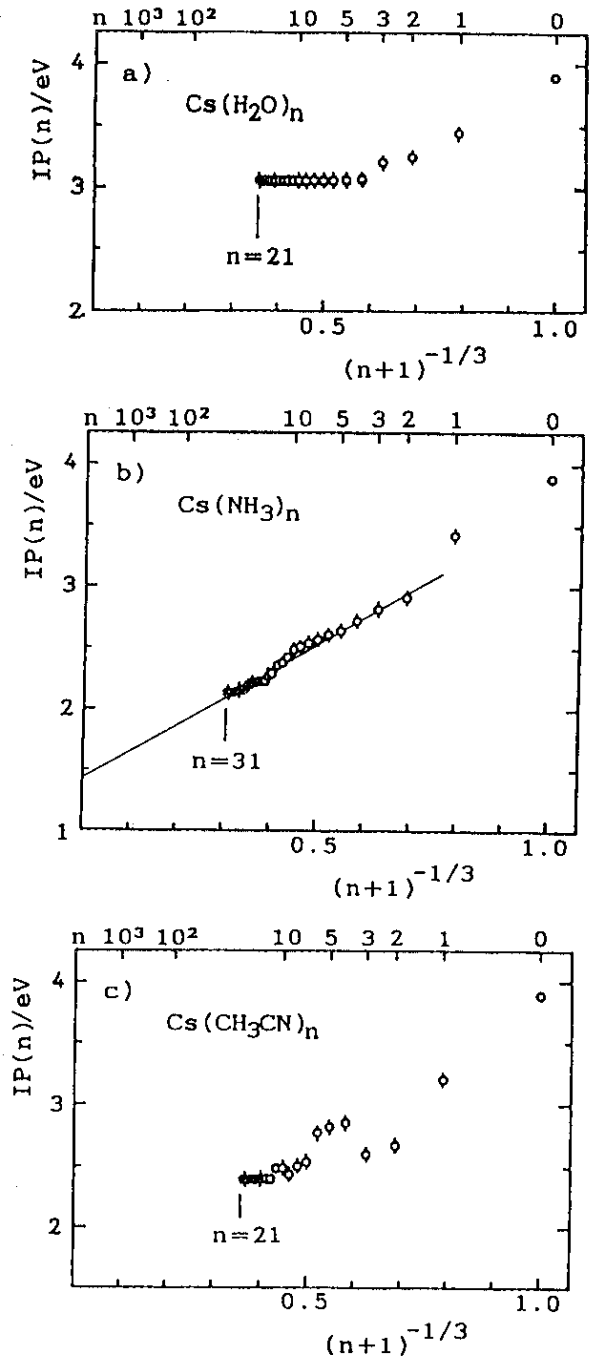

Figure III-5. Ionization potentials (IP(n)) of CsM_n clusters plotted versus $(n+1)^{-1/3}$. Error bars, indicated at each point for $1 \leq n \leq 10$ and at 5 point intervals for $n \geq 10$, include the uncertainty in determining IP(n) and the deviation caused by field ionization. (a) M = H_2O ($n \leq 21$). (b) M = NH_3 ($n \leq 31$). The results of the least-squares fitting for $n \geq 2$ are also shown. The extrapolated value to $(n+1)^{-1/3} = 0$ ($n \rightarrow \infty$) is 1.41 eV. The correlation coefficient of the fitted line, r, is 0.990. (c) M = CH_3CN ($n \leq 21$).

III-4. Discussion

III-4.1. $Cs(H_2O)_n$ clusters

The present results of the n dependence of IP(n) for $Cs(H_2O)_n$ (Figure III-5a) show that the IP(n) values decrease linearly with decreasing $(n+1)^{-1/3}$ for $n \leq 4$ and become constant (IP(∞) = 3.12 eV) for $n \geq 4$. $Na(H_2O)_n$ clusters have been found to show a similar trend in the ionization threshold with the same limiting value (IP(∞) = 3.17 eV) [11]. As suggested by Coe *et al.* [6], this limiting value corresponds to the bulk photoelectric threshold of ice (3.2 eV). These results seem to indicate that, for the alkali atom surrounded by more than four water molecules, the IP does not depend on the metal atom but on the solvent species. In the case of $Cs(H_2O)_n$ ($n \geq 4$) clusters, the IP values decrease by only 0.8 eV from that of an isolated atom (3.89 eV), though the solvation energies are reported to be more than 2 eV for $Cs^+(H_2O)_n$ ($n>4$) [20]. Thus, the present results of the IP measurement imply that the solvated alkali atom in the ground state is fully screened for $n \geq 4$. Kestner and Dhar have recently reported theoretical studies for sodium water clusters in which they predicted the geometrical and electronic structures of clusters in the ground and ionized states [21]. According to their results for the sodium atom surrounded by four water molecules, the electron density of the 3*s* electron is very diffuse and extends over the region occupied by the solvent molecules. As a result, the sodium atom interacts with H_2O molecules by an ionic-type bonding. They also predicted that the energy for the fully optimized neutral $Na(H_2O)_4$ cluster is similar to that for the optimized geometry of the sodium ion-water cluster plus electron. These predictions are consistent with the above observations.

An alkali-metal atom has been known to be ionized spontaneously in a polar solvent and converted to a contact ion-pair of a solvated alkali-atom ion

plus a solvated electron [1, 2]. This state in a bulk fluid may correspond to the lowest ion-pair (or a Rydberg-like) state of the clusters. Then, this bulk behavior can be related to the properties of solvated alkali-atom clusters as follows. Figure III-6 draws schematically the energy levels of the covalent, ion-pair, and ion ground states for a Cs atom-solvent cluster as a function of the cluster size. The energy levels of the ion ground states decrease monotonically with increasing number of solvent molecules, as can be seen from the enthalpies of solvent for the Cs^+ ion [20]. For small clusters, the neutral ground state is of the covalent type and is expected to be stabilized very slowly with increasing number of solvent molecules (Figure III-6). On the other hand, the energy level of the ion-pair state is more sensitive to the number of solvent molecules. When the screening of the solvated alkali atom is effective as mentioned previously, this state is stabilized much more rapidly than that of the covalent-type state. Since the ion-pair state correlates with the ground state of the solvated electron plus the solvated Cs^+ ion in a bulk fluid, the electronic character of clusters in the ground state is expected to change from the covalent type to the ion-pair type at a certain critical cluster size (n^*). Based on the above theoretical results, the curvature of the E versus n curve for the ion-pair state (Figure III-6) is expected to be similar to that of the ionic state for clusters with more than four water molecules; the interaction in both states is mostly electrostatic in nature. Therefore, the observed plateau in the IP(n) versus $(n+1)^{-1/3}$ plot for the $Cs(H_2O)_n$ clusters (Figure III-5a) can be understood by the cluster size dependence of the ion-pair and ionic levels, which suggests that $n^* = 4$.

The mass spectrum shows the enhanced stability of the $Cs(H_2O)_{20}^+$ cluster (Figure III-4b). This value of n often appears as the magic number in mass spectra of $H_3O^+(H_2O)_n$ cluster [14]. There are several possible explanations for the $Cs(H_2O)_{20}^+$ dominance, such as (1) the predominance of

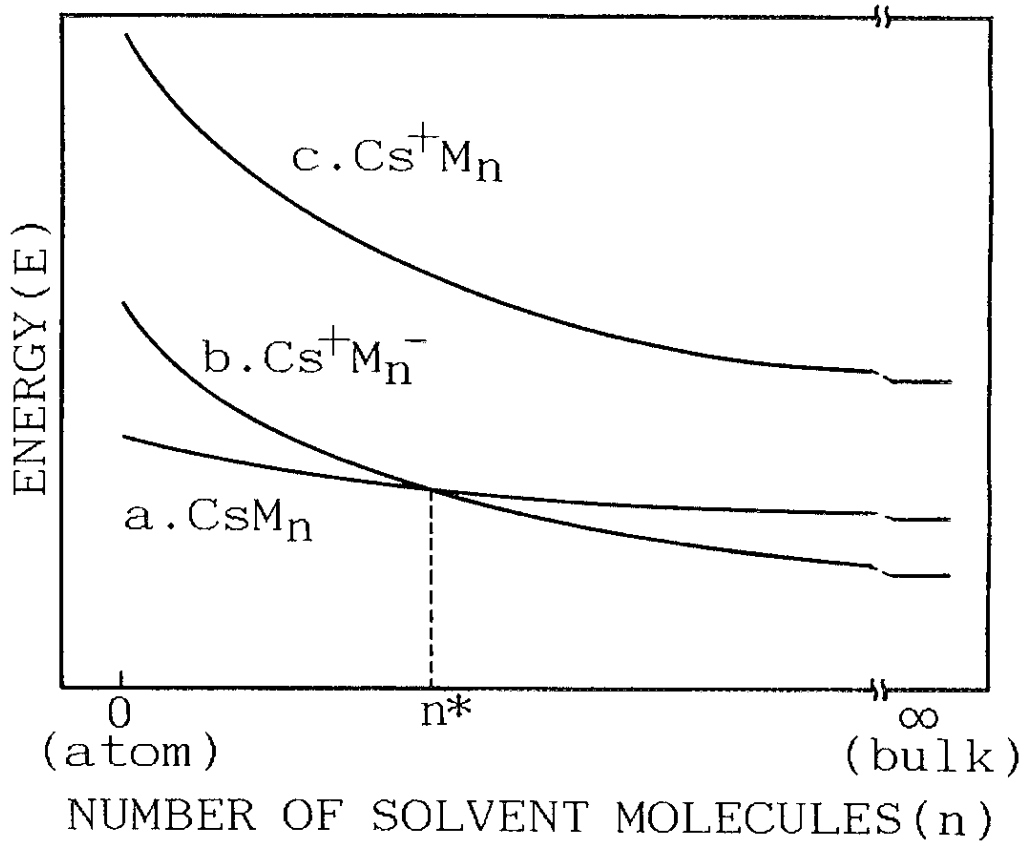

Figure III-6. Schematic diagram of the energies of (a) the lowest covalent, (b) ion-pair, and (c) the ion-ground state for CsM_n (M: solvent molecules) versus n. The ion-pair state is expected to correlate with the ground state of the solvated electron plus the solvated Cs^+ ion in bulk fluids. The ground-state electronic character of the neutral cluster changes from covalent to ion-pair type at a size n^*.

the preformed $(H_2O)_n$ clusters and (2) the special stability of $Cs(H_2O)_{20}^+$ or (3) that of $Cs(H_2O)_{20}$. The photoionization of the $(H_2O)_n$ clusters has been studied extensively and the distribution of the neutral clusters has been known to have no anomaly in the size range discussed here [14]; this may rule out explanation (1). Since the radius of the Cs^+ ion (1.65 Å) is close to that of the H_3O^+ ion (1.7 Å), one can expect the enhanced stability of $Cs^+(H_2O)_{20}$ by analogy to the $H_3O^+(H_2O)_n$ clusters. However, this possibility can also be excluded because the enhanced stability at n=20 is observed even at the photoionization energy close to the ionization threshold (3.1 eV), where the fragmentation due to the excess energy at ionization seems to be negligible. On the other hand, the theoretical calculations for sodium-water clusters for $n \geq 4$ has an ionic character. As with sodium, Cs is expected to interact with water molecules by an ionic-type bonding. Therefore, it is reasonable to ascribe the observed anomaly to the enhanced stability of the $Cs(H_2O)_{20}$ cluster in the ground state (explanation (3)); this observation seems to support the scheme shown in Figure III-6. It is believed from both experimental [15] and theoretical [14] studies that the $H_3O^+(H_2O)_n$ cluster forms a clathrate structure (deformed pentagonal dodecahedron) with the H_3O^+ ion in the center of the hydrogen-bonding networks of 20 water molecules. Thus, the $Cs(H_2O)_{20}$ cluster is expected to be in the ion-pair state in which the ion core has an ion-clathrate structure and the excess electron is distributed outside the core.

III-4.2. $Cs(NH_3)_n$ and $Cs(CH_3CN)_n$ clusters

The results of the IP(n) dependence on n for $Cs(NH_3)_n$ (Figure III-5b) show that the IP(n) value decreases linearly with decreasing $(n+1)^{-1/3}$ for $n \leq 30$. As in the case of $Na(NH_3)_n$ [11], the intercept of the fitted line at $n=\infty$ is 1.4 eV, which agrees with the bulk photoelectric threshold estimated from

the electron binding energies of $(NH_3)_n^-$ clusters [7]. These results imply that the n^* value of the alkali atom-ammonia cluster is expected to be larger than 35. However, the observed IP(n) versus $(n+1)^{-1/3}$ plots indicate that the IP values of small clusters can be extrapolated smoothly to that of the bulk value. Therefore, an alternative explanation is that, in the case of ammoniated alkali-atom clusters, the electronic character of the ground state may change from the covalent type to the ion-pair type with the increasing cluster size.

The intriguing feature of the IP(n) versus $(n+1)^{-1/3}$ plots of the $Cs(CH_3CN)_n$ clusters is the anomalous change of IP(n) for $n \leq 11$ (Figure III-5c). The rises near the threshold in the ionization efficiency curves for n=4-6 are found to be as steep as that for n=1, while those for n=2, 3 and for $n \geq 7$ are much less steep. These results suggest that the differences in the geometry of neutral and ionic clusters for n=4-6 are much closer than those for n=2 and 3. These anomalous change in the geometry may be due to the large permanent dipole moment of acetonitrile. As in the case of the $Cs(H_2O)_n$ clusters, the IP(n) versus $(n+1)^{-1/3}$ plots of the $Cs(CH_3CN)_n$ show a plateau for $n \geq 12$ (n^*=12), which gives the bulk value of 2.4 eV. The behavior of electrons in the bulk acetonitrile has been known to be rather different from those for water and ammonia, where electrons are delocalized over scores of solvent molecules. According to the ESR studies for γ-irradiated acetonitrile crystal, a dimer radical anion, $(CH_3CN)_2^-$, is found to be stable; electrons are trapped by a deep potential well formed in the dimer and a well-defined anisotropic hyperfine structure is observed in the ESR spectrum [22]. Thus, the behavior of the electrons in the bulk is consistent with the finding that the solvated Cs atom is fully screened by a rather small number of acetonitrile molecules as seen in the IP(n) versus $(n+1)^{-1/3}$ plots (Figure III-5c). In order to understand the n dependence of IP for $Cs(CH_3CN)_n$, it seems necessary to carry out an

elaborate theoretical calculation for the neutral and ionic states of these clusters.

The critical number n^* observed in the present study may have some correlation with the cluster size, n_{th}, at which the negatively charged molecular cluster starts to be observed. Several groups have reported n_{th} observed by electrons attachment to molecular clusters: Stable negative ions are produced from n=2 for $(H_2O)_n$ [4], n=10 for $(CH_3CN)_n$ [23] and n=35 for $(NH_3)_n$ [4].

III-5. Conclusion

Cesium atoms solvated with polar solvents, $Cs(H_2O)_n$, $Cs(NH_3)_n$, and $Cs(CH_3CN)_n$, have been studied by one-photon ionization and time-of-flight mass spectroscopy. The solvated Cs atom clusters have been produced by a pickup type cluster source. Ionization potentials of these clusters are determined by the observation of photoionization efficiency curves as a function of the laser photon energy. The ionization potentials of $Cs(H_2O)_n$ and $Cs(CH_3CN)_n$ are found to be constant for $n \geq 4$ (3.1 eV) and $n \geq 12$ (2.4 eV), respectively, while that for $Cs(NH_3)_n$ decreases monotonically with increasing n to a limit of 1.4 eV, which coincides with the bulk value. These results have been discussed in connection with the stability of solvated electrons in these polar solvents. Especially, the behavior of the ionization potentials for $Cs(H_2O)_n$, which exhibit the bulk value only at n=4, is ascribed to the stabilization of an ion-pair state; a spontaneous ionization of metal atom occurs even in the small clusters.

III-6. Appendix

According to a classical calculation, the ionization potential IP_m of a spherical droplet consisting of m particles is written as

$$IP_m = WF + 3e^2/8R, \quad \text{(III.1)}$$

where WF is the work function of the planer solid, and R is the radius of the droplet [24]. Because R is written using the number density ρ as

$$R = [(3\rho/4\pi)m]^{1/3}, \quad \text{(III.2)}$$

IP_m is proportional to $m^{1/3}$ for a cluster with large m sufficient to be approximated as a sphere. Therefore, for CsM_n cluster the IP(n) values are expected to be proportional to $(n+1)^{-1/3}$ (Cs atom plus n solvent molecules).

References for Chapter III

[1] *Electrons in fluids,* edited by J. Jortner and N.R. Kestner (Springer, Berlin, 1973).

[2] *The chemical physics of solvation*, Part C, edited by R. R. Dogonadze, E. Kalman, A. A. Kornyshev, and J. Ulstrup, (Elsevier, Amsterdam, 1988).

[3] H. Haberland, H. -G. Schindler and D. R. Worksnop, *Ber. Bunsenges. Phys. Chem.* **88**, 270 (1984).

[4] H. Haberland, C. Ludewigt, H. -G. Schindler and D. R. Worksnop, *Surf. Sci.* **156**, 157 (1985).

[5] P. J. Campagnola, L. A. Posey and M. A. Johnson, *J. Chem. Phys.* **92**, 3980
(1990).

[6] J. V. Coe, G. H. Lee, J. G. Eaton, H. W. Sarkas, K. H. Bowen, C. Ludewigt, H. Haberland and D. R. Worsnop, *J. Chem. Phys.* **92**, 3980 (1990).

[7] G. H. Lee, S. T. Arnold, J. G. Eaton, H. W. Sarkas, K. H. Bowen, C. Ludewigt and H. Haberland, *Z. Phys.* D **20**, 9 (1991).

[8] R. N. Barnett, U. Landman, C. L. Cleaveland and J. Jortner, *Chem. Phys. Lett.* **145**, 382 (1988).

[9] R. N. Barnett, U. Landman, C. L. Cleaveland, N. R. Kestner and J. Jortner, *Chem. Phys. Lett.* **148**, 249 (1988).

[10] C. P. Schulz, R. Haugstätter, H. -U. Tittes and I. V. Hertel, *Phys. Rev. Lett.* **57**, 1703 (1986).

[11] C. P. Schulz, R. Haugstätter, H. -U. Tittes and I. V. Hertel, *Z. Phys.* D**10**, 279 (1988).

[12] I. V. Hertel, C. Hüglin, C. Nitsch and C. P. Schulz, *Phys. Rev. Lett.* **67**, 1767 (1991).

[13] J. Q. Searcy and J. B. Fenn, *J. Phys. Chem.* **61**, 5282 (1974).

[14] U. Nagashima, H. Shinohara, N. Nishi and H. Tanaka, *J. Chem. Phys.* **84**, 209 (1986).

[15] H. Shinohara, U. Nagashima, H. Tanaka and N. Nishi, *J. Chem. Phys.* **83**, 4183 (1985).

[16] M. Marchi, M. Sprik and M. L. Klein, *J. Phys.* C**2**, 5833 (1990).

[17] G. J. Martyne and M. L. Klein, *J. Phys. Chem.* **95**, 515 (1991).

[18] G. Lepoutre and J. Jortner, *J. Phys. Chem.* **76**, 683 (1972).

[19] U. Schindewolf, *J. Phys.Chem.* **88**, 3820 (1984).

[20] R. G. Keesee and A. W. Castleman Jr., *J. Phys. Chem. Ref. Data* **15**, 1016(1986).

[21] N. R. Kestner and S. Dhar, in *Large finite system*, edited by J. Jortner, p. 209, (Reidel, Dordrecht, 1987) .

[22] F. Williams and E. D. Sprangue, *Acc. Chem. Res.* **15**, 408 (1982).

[23] T. Kondow, *J. Phys. Chem.* **91**, 1307 (1987).

[24] D. M. Wood, *Phys. Rev. Lett.* **46**, 749 (1981).

Chapter IV

Photodissociation of $Mg^+(H_2O)_n$ cluster ions

IV-1. Introduction

The physical and chemical properties of molecular clusters have been studied extensively for the purpose of bridging those in the gas phase and in the bulk liquid. Especially, excess electrons in the clusters consisting of polar solvent molecules such as water and ammonia have been one of the central targets of this field in relation to the bulk solvated electron [1-15].

The alkaline-earth metal ion-solvent systems, M^+S_n ($S=H_2O$ and NH_3), have also been investigated for the same purpose as the solvated alkali atom clusters discussed in Chapter III. The alkaline-earth atomic ion has a configuration isoelectronic with the alkali metal atoms, with one valence electron in the *s* orbital. The anomaly in IPs for alkali atom-water clusters was interpreted in terms of the stabilization of the ion-pair state, $M^+S_n^-$, corresponding to the solvated electron state of bulk water. The alkaline-earth metal ion-water clusters interest in analogy of alkali atom-water clusters: That is whether the ion-pair state, $M^{2+}L_{n-m}^-L_m$, is stabilized with increasing the number of water molecules, *n*, or not. This type of ion-pair state was first suggested for Sr^+-NH_3 clusters; the strong size dependence of the photodissociation spectrum was ascribed to the stepwise solvation of the ion-pair state [43]. However, the theoretical calculations reported recently suggested another interpretation with the large redshift of the absorption band ascribed to the mixing of states derived from those correlating to ^2P and ^2D of Sr^+ [32].

It is important to elucidate the energetics and dynamics of the ion-molecule reaction, because it has close connection with solution chemistry, atmospheric chemistry, flame chemistry, and interstellar chemistry. The studies on metal-solvent cluster ions in the gas phase provide insights into ion-molecular interactions such as charge-dipole and charge-induced dipole interactions. In order to get information on the microscopic aspect of solvation, thermochemical properties of monovalent metal cations solvated with water have been extensively studied for the last decades [16-36]. These studies were devoted to determining the successive binding energies by high pressure mass spectrometry [16-22], collision-induced dissociation (CID) [23-25], and photodissociation experiments. The binding energies obtained experimentally have found to be in agreement with the results of theoretical studies [28-36].

In the present chapter, we examine the photodissociation of $Mg^+(H_2O)_n$ cluster ions with n up to 5. As for n=1, Duncan and his co-workers reported high resolution photodissociation spectra of $Mg^+(H_2O)$ and $Mg^+(D_2O)$ [37,38]. The stretching and bending vibrational modes between the metal ion and water were analyzed for the two low-lying excited electronic states. They estimated the dissociation energies of the excited state by extrapolation of the vibrational progression. On the other hand, though the photodissociation spectra presented here for n=1-5 have lower resolution, including insufficient cooling of the parent ions, they are still of advantage to survey the electronic structure of these cluster ions in the broad wavelength region from UV to near IR. The photodissociation spectra for n=1-5 are assigned to the transitions having a ^2P-^2S character of the free Mg^+ ion with the aid of *ab initio* CI calculations. The mass spectra of the photofragment ions show the existence of two dissociation processes: the evaporation of H_2O molecules from parent ions and the photoinduced intracluster reaction to produce hydrated $MgOH^+$

ions, $MgOH^+(H_2O)_m$. The branching fraction between the two processes depends strongly on the solvent number n and also on the photolysis wavelength. A possible dissociation mechanism is discussed on the basis of the results of laser fluence dependence and branching ratio of the fragment ions.

IV-2. Experimental

IV-2.1. Photodissociation of size-selected ions

The principle of the reflectron time-of-flight mass spectrometer (TOFMS) was described in Chapter II. In order to detect the photofragment ions produced by size-selected photodissociation, we used the reflectron TOFMS as a tandem type mass spectrometer. The method of the mass-selected photodissociation is illustrated schematically in Figure IV-1. The parent ion (mass M_p) with the initial kinetic energy, eU_0, travels to the first field free region. The arrival time to an interaction point of the parent ion with the photolysis laser is easily calculated by eqs.(II.3) to (II.6). The irradiation of the photolysis laser is synchronized with the arrival time of parent ion, and decomposes the parent ion into the fragment ion (mass m_f). The kinetic energy of fragment ion, eU_f, is expressed as

$$eU_f = \frac{m_f}{M_p} \cdot eU_0. \qquad \text{(IV.1)}$$

Then the parent and fragment ions are reaccelerated back into the second field free region by deceleration and reflection potential, U_T and U_K, respectively. In the case of $U_K > U_0 > U_f > U_T$, the reflector plays a role as second mass spectrometer to resolve the parent and fragment ions: the fragment ions with

a) Timing chart of photodissociation of size-selected ions

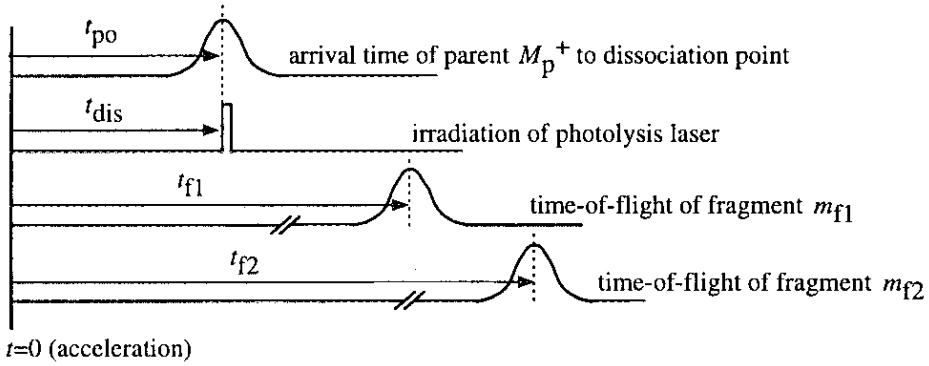

b) Method I ($U_0 > U_K > U_{f2} > U_{f1} > U_T$)

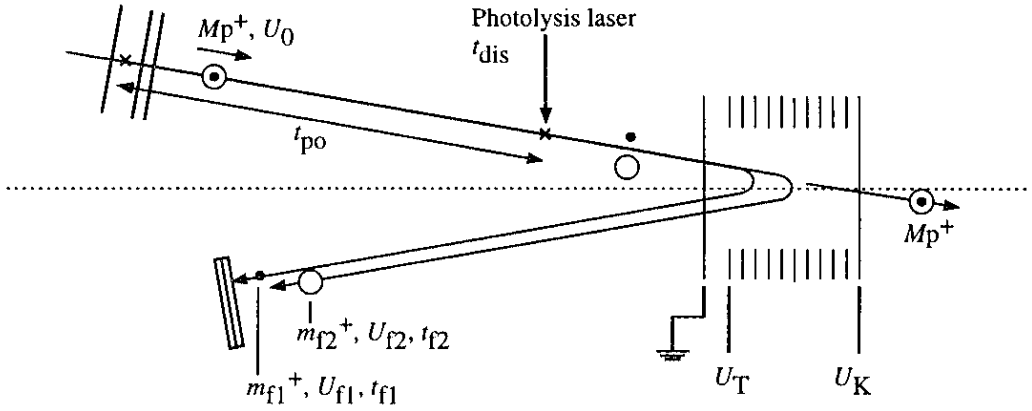

c) Method II ($U_K > U_0 > U_{f2} > U_{f1} > U_T$)

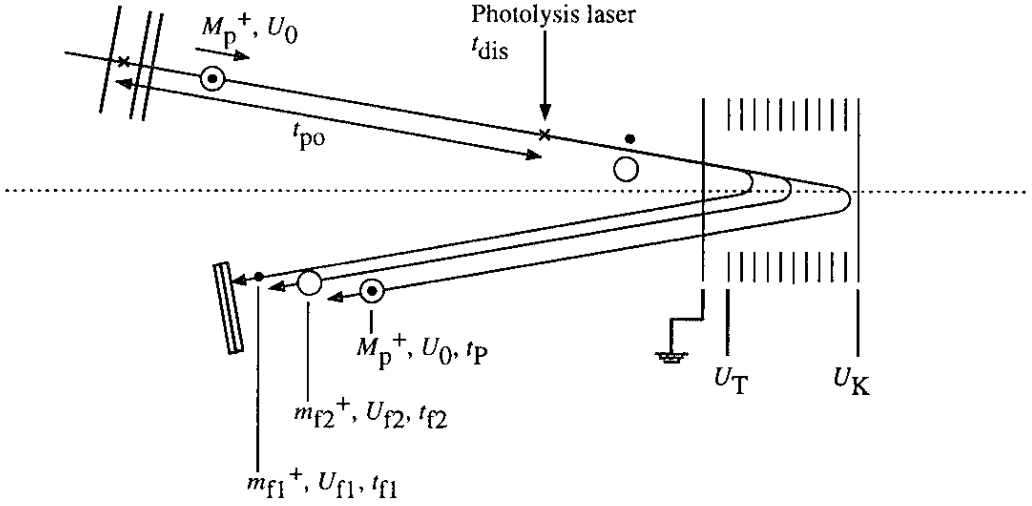

Figure IV-1. Schematic diagrams of the photodissociation experiments of size- selected cluster ions. The potentials of fragment ions, $U_{f1,2}$, are determined by eq. (IV.1).

smaller kinetic energies arrive at detector faster than the parent ion. Under the potential conditions of $U0>U_K>U_f>U_T$, only the fragment ions arrive at detector.

IV-2.2. Photodissociation spectrum

The parent ion (M_p^+) decomposes into the fragment ions (m_f^+) and neutral fragments (m_o) by the laser irradiation.

$$M_p^+ + h\nu \rightarrow m_{f1}^+ + m_{f2}^+ + \ldots + m_{fn}^+ + m_o. \qquad \text{(IV.2)}$$

The yield of fragment ions is represented in the thin target limit. The ratio, A, of photodestruction is given by the relationship as a function of laser fluence

$$A = \frac{I}{I_0} = \exp(-\sigma_{dis}\Phi), \qquad \text{(IV.3)}$$

where, I and I_o are the final and initial intensities of the parent ions, respectively, and σ_{dis} is the photodissociation cross section in cm^2, and Φ is the laser fluence in units of photon cm^{-2}. The laser fluence must be carefully attenuated to avoid saturation and multiphoton dissociation process. On the other hand, the photoemission processes may not contribute to the relaxation processes of the $Mg^+(H_2O)_n$ ions: Generally speaking, the significant fluorescence quantum yields are not expected, because the radiative lifetime should be comparable to that for free ion, $\sim 10^{-8}$ s, while the lifetime for dissociation, which should be comparable to molecular vibration and rotational periods, may be ranging from 10^{-14} to 10^{-12} s. Therefore, under this condition of the laser fluence, the absorption cross section, σ_{abs}, is substituted by using the dissociation cross section, σ_{dis}. Furthermore, the dissociation

cross section is represented by the total yields of fragment ions produced in the dissociation process as given by eq.(IV.2). That is,

$$\sigma_{abs.} \propto \sigma_{diss.} \propto \sum_{n} I_{fn}, \qquad \text{(IV.4)}$$

where, I_{fn} is the intensity of n'th fragment ion in eq.(IV.2).

The photodissociation spectrum is obtained by plotting the total yield of fragment ions as a function of the photon energy. The total yield is normalized by both the laser fluence and the parent ion intensity.

IV-2.3. Experimental setup

Details of the experimental setup have been described in Chapter II. The apparatus is composed of a solvated metal cluster ion source, a reflectron time-of-flight (TOF) mass spectrometer and laser systems for photolysis of size-selected cluster ions as shown in Figure IV-2.

The magnesium-water cluster ions were formed in a pick-up type cluster source; magnesium ions were produced by laser irradiation of a rotating Mg rod (ϕ 5 mm) which was placed about 10 mm downstream from a pulsed valve (General Valve, Series 9). The ions were picked up by water clusters formed by expansion of water vapor seeded in He gas from the valve. Typical pressures of H_2O vapor and He were 20 Torr (vapor pressure at room temperature) and 4 atm, respectively. Resultant ions were injected into the TOF mass spectrometer after being collimated with a skimmer. The ions were accelerated colinearly with the incident cluster ion beam by pulsed electric fields in the acceleration grids of the Wiley-McLaren type TOF mass spectrometer. After mass-separating in the first drift region of the reflectron (1400 mm flight length), cluster ions of a given mass-to-charge ratio were irradiated with a photolysis laser at a right angle to the beam direction just

prior to entering the deceleration and reflection grids. Photofragment ions were mass-analyzed in those grids and in the second field-free region (650 mm flight length) and detected by dual microchannel plates (Hamamatsu, F1552-23S). Ion signals were stored in a digital storage oscilloscope (LeCroy 9450) and were typically averaged over 500 laser shots.

Output of a pulsed Nd:YAG-pumped dye laser (Quanta-Ray, DCR-2A/PDL-3) was used for photolysis with wavelengths of 430-720 nm. Also the second harmonic of the dye laser output, and the sum-frequency output of the Nd:YAG fundamental (1064 nm) and dye laser were used for photodissociation in the wavelength regions of 270-360 nm and 360-430 nm, respectively, by utilizing KDP crystals mounted on a wavelength extension system (Quanta-Ray, WEX). For 250-270 nm, the second harmonic was generated by using BBO
crystal mounted on another frequency doubling system (Inrad, Autotracker II). The photolysis laser fluence was attenuated to less than 1 mJ/cm^2 in order to prevent saturation and nonresonant multiphoton processes.

Photofragment ion yield is very sensitive to the conditions of the ion source and the ion acceleration optics. In order to improve the signal-to-noise ratio of the dissociation spectra, fragment ion intensity at some fixed wavelength was monitored alternately as a reference by irradiation with a XeCl excimer laser (Lambda Physik, EMG103) at 308 nm. Each fragment ion intensity in the mass spectrum was normalized by the reference signal. Relative photodissociation cross sections and fragment ion yields were determined by averaging the normalized intensity of more than three independent measurements.

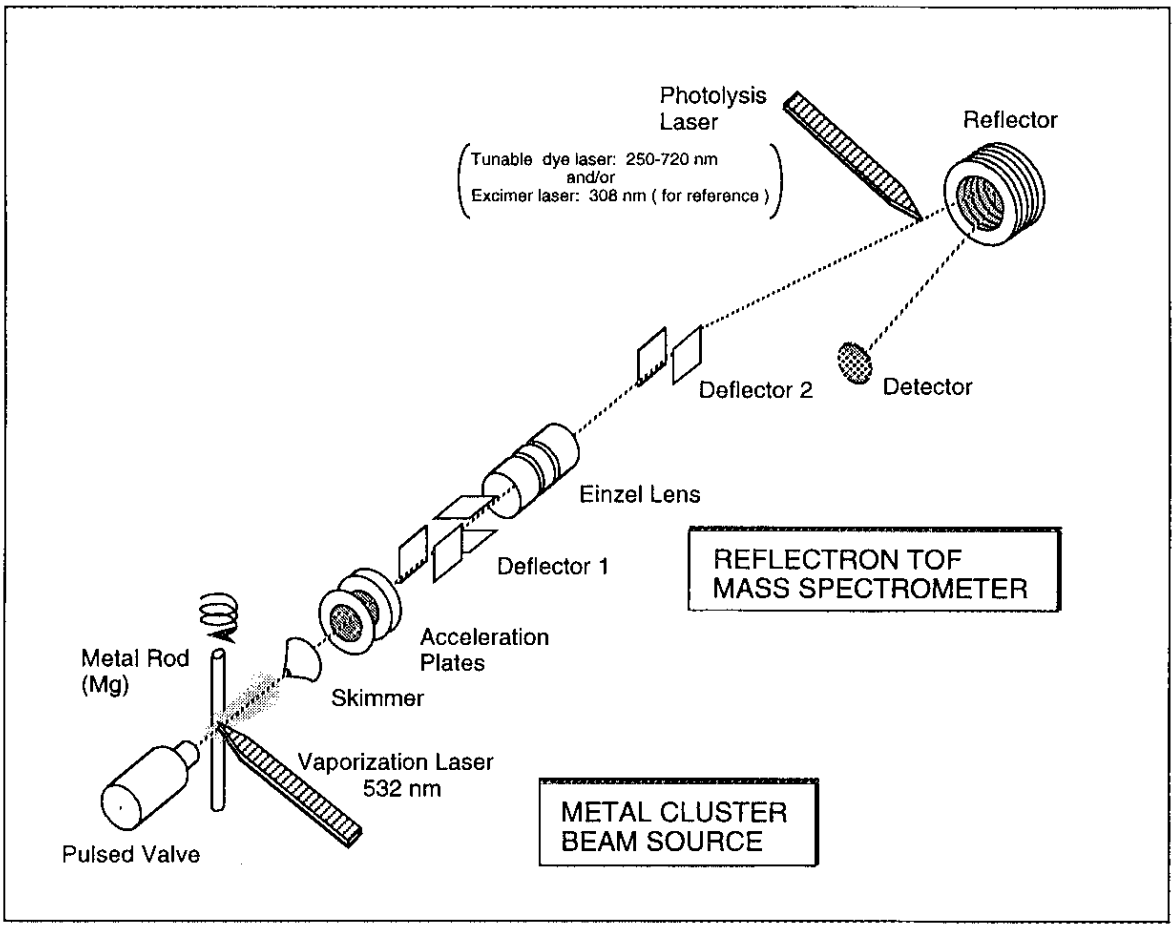

Figure IV-2. Schematic drawing of the apparatus. The ion source chamber, the ion acceleration chamber, and the TOF tube are differentially pumped to $1x10^{-5}$, $6x10^{-7}$, and $8x10^{-8}$ Torr, respectively, during the measurement.

IV-3. Results

IV-3.1. Size distribution of parent ions

As mentioned in the experimental section, the parent cluster ions are produced by the collision reaction between the laser-vaporized Mg^+ ions and water clusters. A typical TOF mass spectrum of Mg-water cluster ions directly produced in the source is shown in Figure IV-3. Mass resolution, $M/\Delta M$, of about 800 is achieved in this mass spectrum, and thus, the author can distinguish the three isotopes of Mg^+ such as ^{24}Mg, ^{25}Mg, and ^{26}Mg (hereafter, Mg^+ refers to the most abundant $^{24}Mg^+$ ion). Both $Mg^+(H_2O)_n$ and $MgOH^+(H_2O)_{n-1}$ ions are found to be produced by collision of Mg^+ ion with water clusters in the cluster source. Though the magnesium atom has three isotopes, the author can estimate the abundances of the above two series of cluster ions, which appear with intervals of unit mass in the mass spectrum, from the known isotopic abundances. Figure IV-4 shows the relative abundances of $Mg^+(H_2O)_n$ and $MgOH^+(H_2O)_{n-1}$ determined from the mass spectrum. Unusual size distribution is observed: For $1 \leq n \leq 5$ and $n \geq 15$, the $Mg^+(H_2O)_n$ ions are dominantly produced. In contrast, $MgOH^+(H_2O)_{n-1}$ are exclusively observed for $6 \leq n \leq 14$. These results clearly show the product switching at two critical sizes. Although I measured the mass spectrum of nascent cluster ions with different stagnation pressure and different fluence of vaporization laser, the critical size is found to be not affected by the experimental conditions. The similar size dependence is also observed for Mg^+-D_2O, Ca^+-H_2O, and Ca^+-D_2O systems, though they are found to be affected by deuterium and metal substitutions. Details of these observations will be presented in Chapter VI.

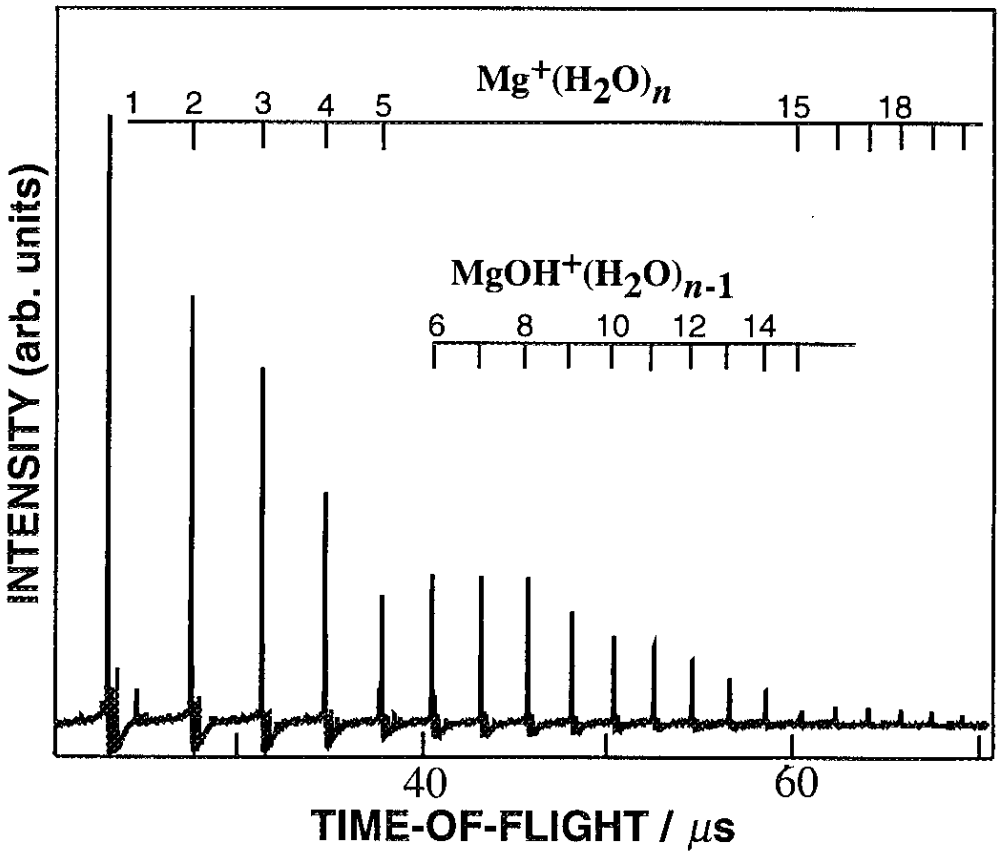

Figure IV-3. Typical time-of-flight mass spectrum of the nascent cluster ions produced by laser vaporization. The $Mg^+(H_2O)_n$ ions are dominantly produced for $1 \leq n \leq 5$ and $n \geq 15$, while $MgOH^+(H_2O)_{n-1}$ is observed exclusively for $6 \leq n \leq 14$.

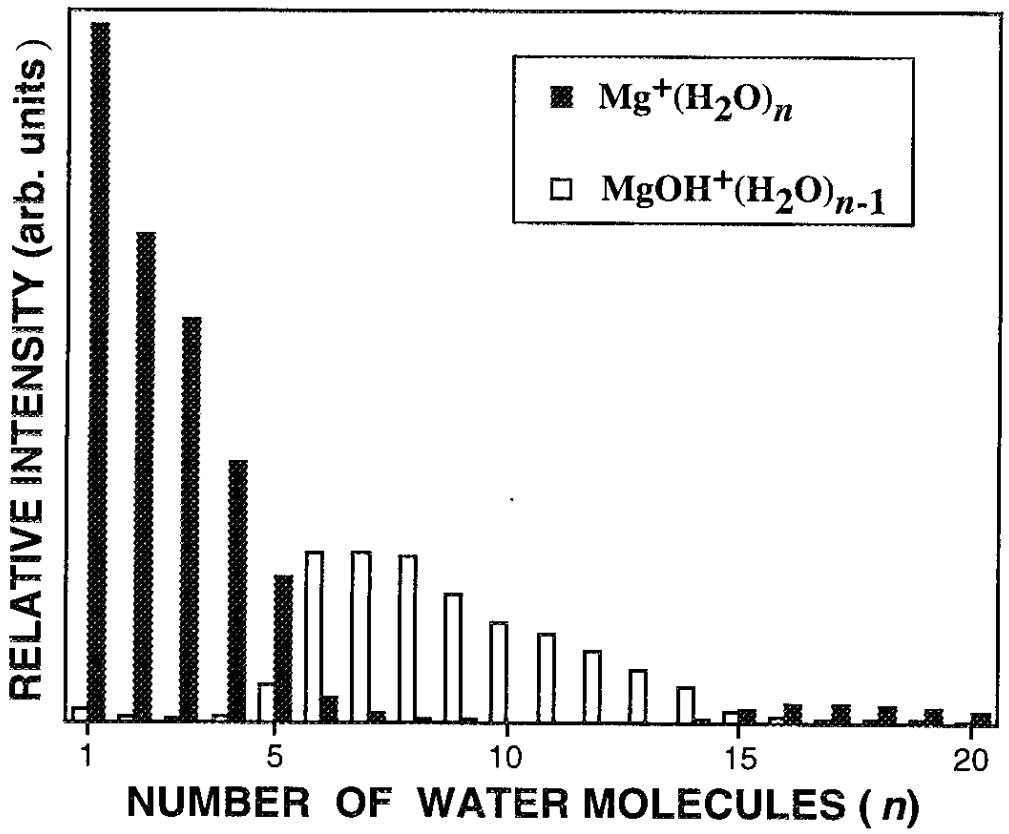

Figure IV-4. Relative abundances of the $Mg^+(H_2O)_n$ and $MgOH^+(H_2O)_{n-1}$ ions estimated from the mass spectrum in Figure IV-3. The $Mg^+(H_2O)_n$ ions are dominant for $n \leq 5$ and $n \geq 15$, whereas the hydrated $MgOH^+$ ions are almost uniquely produced for $6 \leq n \leq 14$.

IV-3.2. Photofragment ion mass spectra

In order to identify the fragment ions in the photodissociation process, the author measured the mass spectrum by carefully adjusting the electric potential of the decelerator and reflector of the reflectron. As an example, the mass spectra of daughter ions produced by dissociation of $Mg^+(H_2O)_2$ (mass number M_p=60) at various wavelengths are displayed in Figure IV-5. These spectra were obtained with a reflector voltage, U_K, of 2.6 keV, while an acceleration voltage of the parent ions, U_0, was 3.3 keV. Under this condition, only the fragment ions with mass numbers smaller than $(U_K/U_0)M_p$=(2.6/3.3) × 60=47.3 were reflected and detected (Method I). Three peaks are observed in these mass spectra: The peaks at 24.6 and 23.4 μs are assigned to the $Mg^+(H_2O)$ and the Mg^+ ions, respectively, by using the simple electrostatic calculation. In addition to these fragment ions produced by evaporation of water molecules, the peak assignable to the $MgOH^+$ ion, which is produced by photodissociation of the ligated H_2O, is observed at a flight time of about 70 ns shorter than $Mg^+(H_2O)$ (left-hand side of the peaks observed at 24.6 μs). The mass assignment of these fragment ions was confirmed by comparison with the results of $Mg^+(D_2O)_2$ photodissociation. These results indicate that the photodissociation process of $Mg^+(H_2O)_2$ include not only the evaporation of one or more water molecules but also the photoinduced chemical reaction to produce hydrated $MgOH^+$ ions. The latter ions are produced by an H-atom elimination reaction. In order to identify the primary product of this reaction, the author also measured the fragment-ion mass spectrum with different condition that the electric potential of the reflection plate in the reflectron TOF mass spectrometer was adjusted so that both the parent and fragment ions were reflected and detected (Method II). Figure IV-6 shows TOF mass spectra obtained by the photodissociation of $Mg^+(H_2O)_2$ under this condition. As it is seen in this figure, the

$MgOH^+(H_2O)$ is also detected at one mass unit smaller than the parent ion. These results clearly show that the primary product of this reaction is the $MgOH^+(H_2O)$ ion and the $MgOH^+$ ion seen in Figure IV-6 is generated by the evaporation of a water molecule from the primary product. The TOF mass spectra in the dissociation of $Mg^+(H_2O)_3$ taken with method I is also shown in Figure IV-7. This method is found to have an advantage to detect the smaller fragment ions sensitively without any intense signals of the parent ions.

The similar photodissociation experiment is also carried out for n=1, 4, and 5. The primary products, those are the H-atom loss product, are detected for n=1-3, but not for n=4 and 5 as shown in the next section. The depletion of the parent $Mg^+(H_2O)_n$ ions was not detected within the present experimental accuracy, though more than 10 % depletion was observed for Ar_3^+ at 532 nm under the same experimental conditions. Thus the photodissociation cross section at the absorption maxima for $Mg^+(H_2O)_{1,2}$ is estimated to be ca. 10^{-17} cm^2, which is at least one order of magnitude smaller than that of Ar_3^+ at 532 nm [39]; the cross section estimated here seems to be consistent with those for $Sr^+(H_2O)_{1,2}$ [42].

IV-3.3. Branching ratios of photofragment ions

As mentioned in the previous section, the photoexcitation of $Mg^+(H_2O)_n$ induces the intracluster reaction to produce the H-atom loss products as well as the simple evaporation of water molecules. In order to clarify the mechanisms

of these processes, we measured the branching ratio of the photofragment ions for $Mg^+(H_2O)_n$, n=1-5, as a function of excitation energy. In addition, the laser fluence dependence on each fragment ions was also examined.

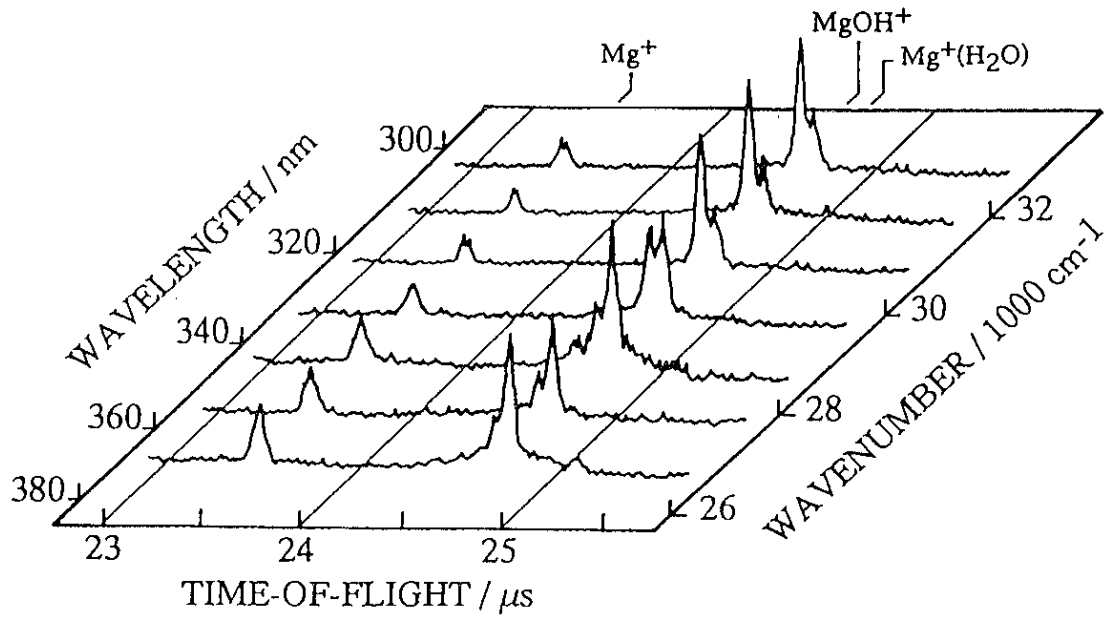

Figure IV-5. TOF mass spectra in the photodissociation of $Mg^+(H_2O)_2$ taken at several wavelengths. These were obtained under the condition (Method I) that the voltage of the reflection plate was adjusted so as to reflect only the fragment ions of the mass number smaller than 47. The parent ions and the larger fragment ions ran through the plate and were not detected.

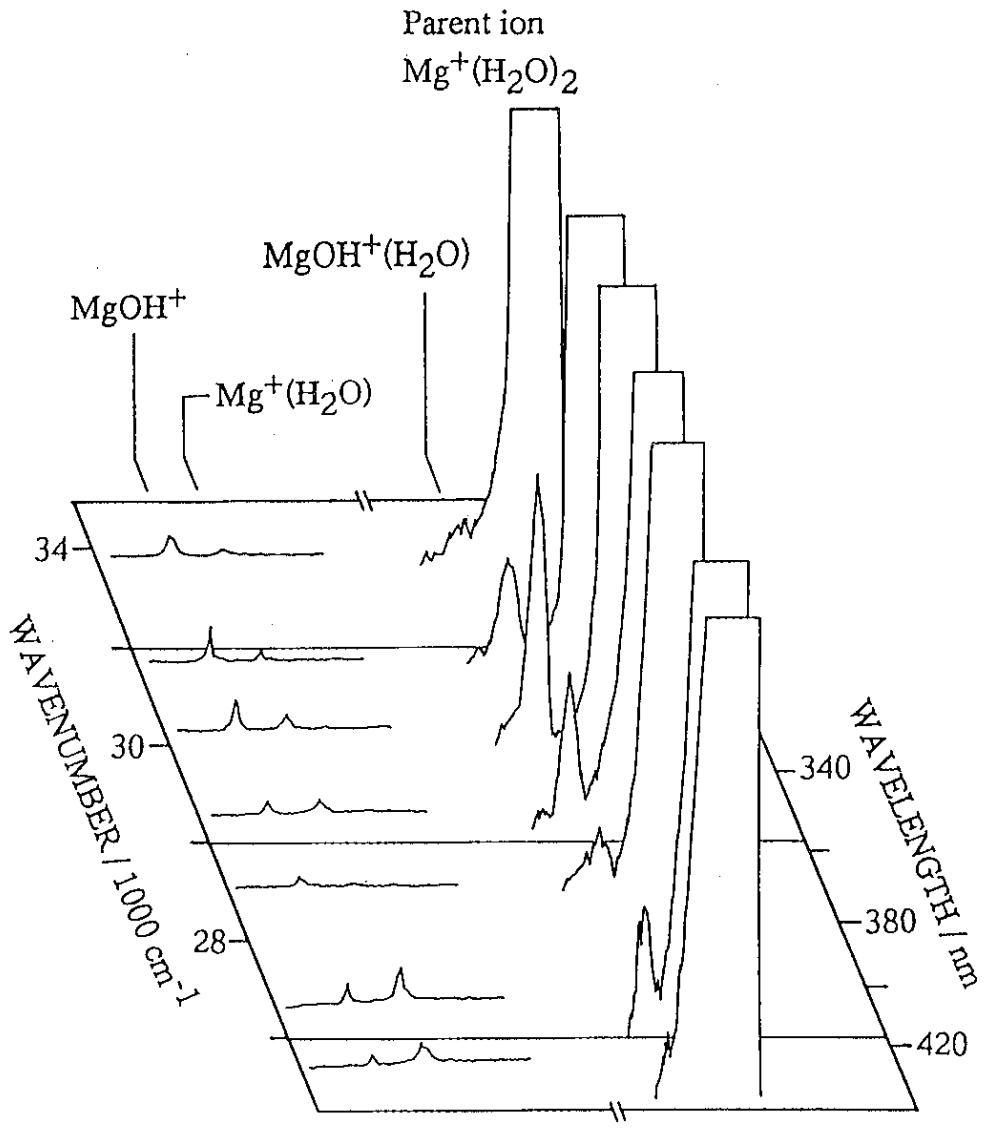

Figure IV-6. TOF mass spectra in the photodissociation of $Mg^+(H_2O)_2$ taken at several wavelengths. These were obtained under the condition of Method II. Therefore, both the parent and fragment ions were reflected and detected. The voltage of the deceleration plate was also regulated in order to separate the TOF signals of the fragment ions from those of the parent ions.

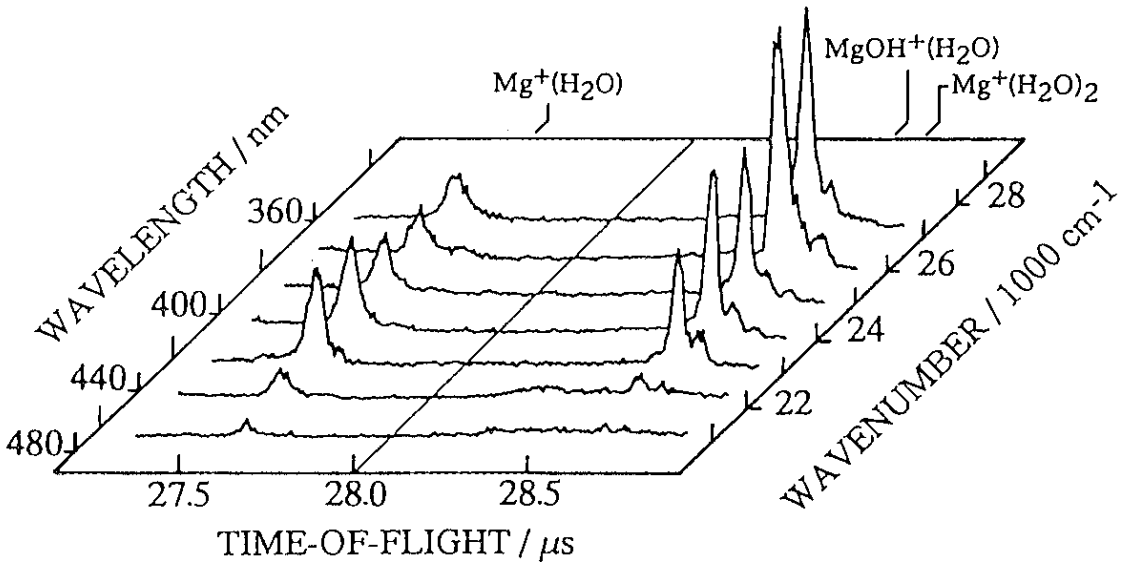

Figure IV-7. TOF mass spectra in the $Mg^+(H_2O)_3$ photodissociation taken at several wavelengths. These were obtained under the condition (Method I) that the voltage of the reflection plate was adjusted so as to reflect only the fragment ions of the mass number smaller than 61. The parent ions and the larger fragment ions penetrated through the plate and were not detected.

Photodissociation for n=1 In the dissociation of $Mg^+(H_2O)$, the Mg^+ and $MgOH^+$ ions are formed as the evaporation and reaction products, respectively. Branching ratio between the process to produce $MgOH^+$ and Mg^+ is ca. 93:7 and is almost constant for photolysis energy of 28000-40000 cm^{-1} as shown in Figure IV-8.

Photodissociation for n=2 For n=2, four kinds of product ions were observed such as $Mg^+(H_2O)$, Mg^+, $MgOH^+(H_2O)$, and $MgOH^+$ as depicted in Figures IV-5 and IV-6. Figures IV-9 and IV-10 show the branching fractions and the relative dissociation cross sections of these fragment ions as a function of photon energy, respectively. In the energy below 27000 cm^{-1}, both the evaporation and reaction processes were detected with nearly the same amount, while the H-atom loss to produce $MgOH^+(H_2O)$ was found to be dominant in the higher energy region. As seen in Figure IV-9, $MgOH^+(H_2O)$ is the primary product of the intracluster reaction and the evaporation of a water molecule from this ion is also detected in the energy region above 29000 cm^{-1}: the $MgOH^+$ yield shows a clear onset. The laser fluence dependence of the fragment ion intensity was measured for these fragment ions at several photolysis wavelengths. The examples of the measurements are displayed in Figure IV-11. The fragment Mg^+ and $Mg^+(H_2O)$ ions are found to be produced by one photon process at any wavelength examined. In contrast, for the production of $MgOH^+$, two photons are needed at lower energy than 29000 cm^{-1} (3.60 eV), though at higher energy only one photon is needed. The two photon process could not be excluded even at laser fluence less than 0.4 mJ/cm^2, and therefore, the appearance threshold of the $MgOH^+$ production was determined to be 3.60 eV. The mechanism of the two-photon dissociation process will be discussed later.

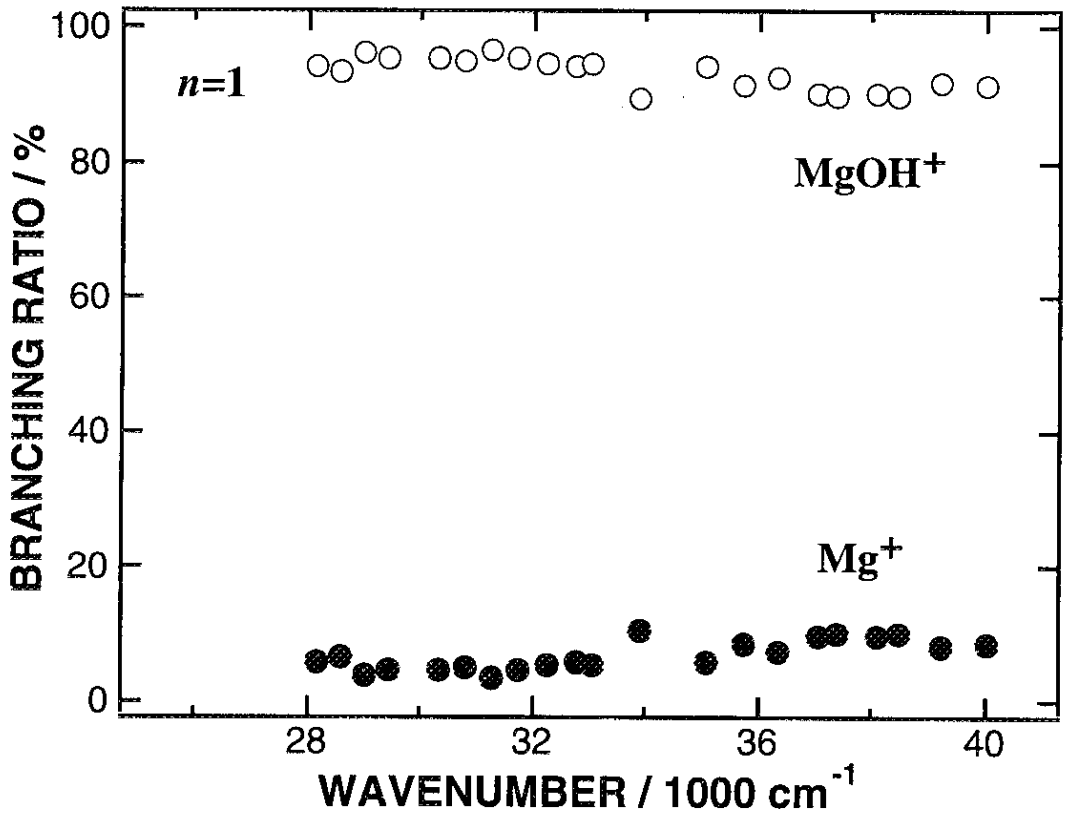

Figure IV-8. Branching ratio between the $MgOH^+$(○) and Mg^+(●) fragment ions in the photodissociation of $Mg^+(H_2O)$ plotted vs. photon energy from 28000-40000 cm^{-1}. Branching fractions of these ions are almost constant ($MgOH^+$:Mg^+ = 93:7) in the above energy region.

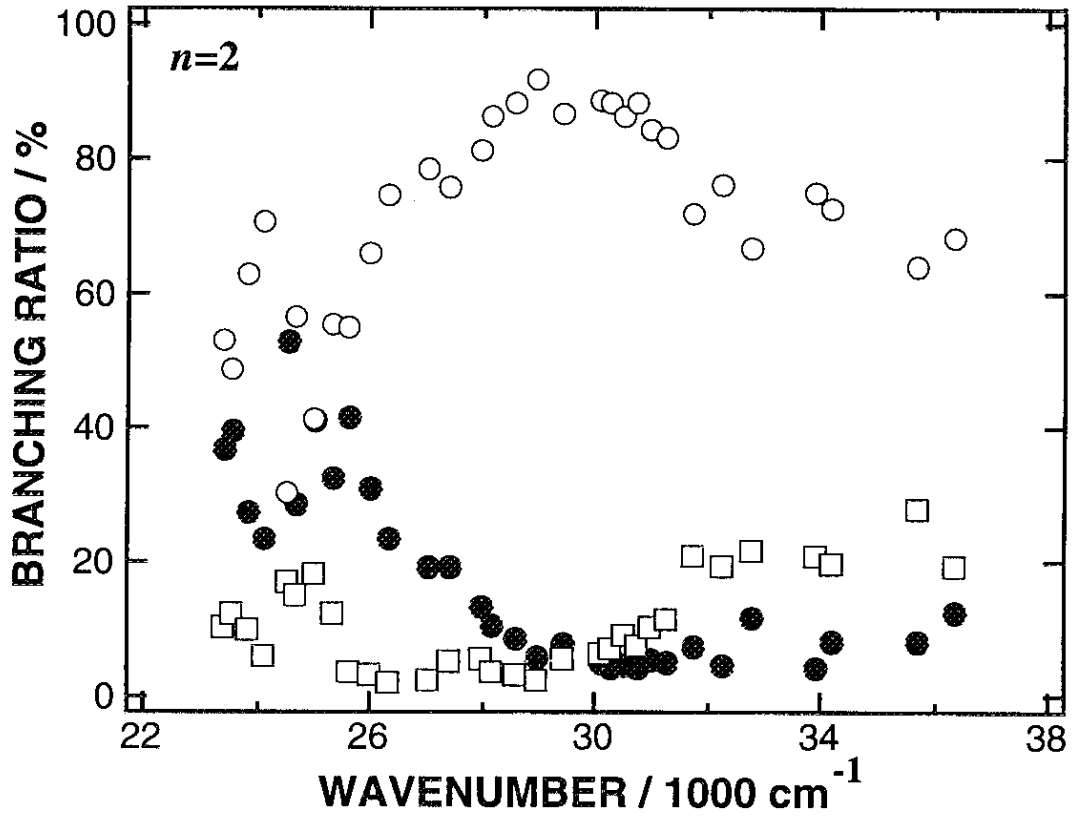

Figure IV-9. Branching ratios of $MgOH^+(H_2O)$ (○), $MgOH^+$ (□), and $[Mg^+(H_2O) + Mg^+]$ (●) produced by the photodissociation of $Mg^+(H_2O)_2$ plotted vs. photon energy from 23000 to 36500 cm^{-1}.

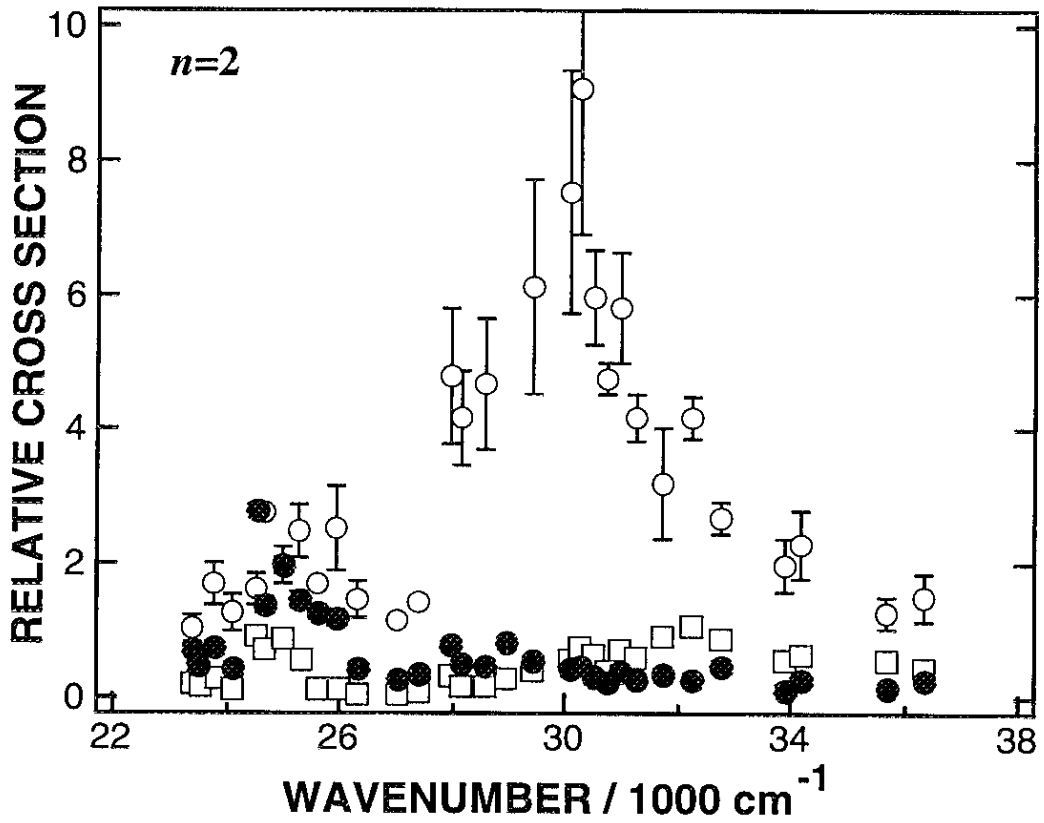

Figure IV-10. Relative cross sections of the $MgOH^+(H_2O)$(○), $MgOH^+$ (□), $Mg^+(H_2O)$ and Mg^+ (●) fragment ions in the photodissociation of $Mg^+(H_2O)_2$ plotted vs. photon energy from 23000 to 36500 cm^{-1}.

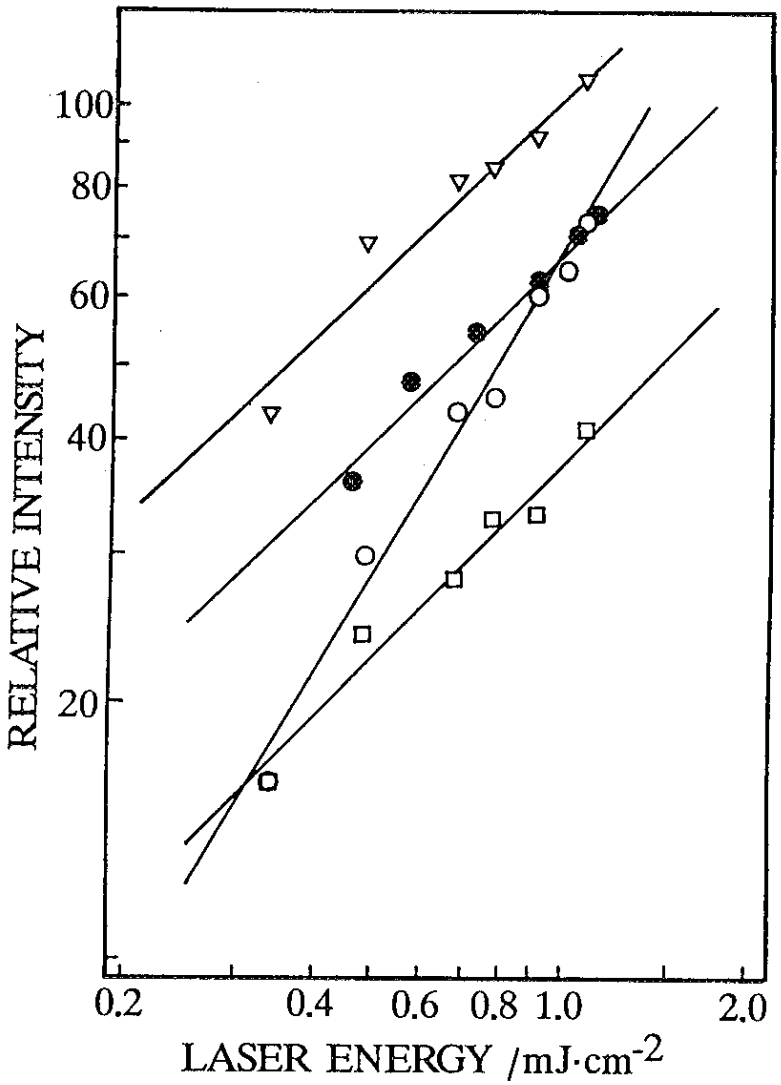

Figure IV-11. Log-log plots of the fragment ion intensities vs. the fluence of the photolysis laser in the photodissociation of $Mg^+(H_2O)_2$. The lines are the results of the least square fittings. (▽) $Mg^+(H_2O)$ at 400 nm, slope = 0.98. (○) $MgOH^+$ at 400 nm, slope = 1.74. (□) Mg^+ at 400 nm, slope = 1.05. (●) $MgOH^+$ at 320 nm, slope = 1.01.

Photodissociation for the larger clusters The branching fraction of the fragment ions dissociated from $Mg^+(H_2O)_3$ is depicted in Figure IV-12. For n=3, $Mg^+(H_2O)_{1,2}$ and $MgOH^+(H_2O)_{1,2}$ ions were detected as the major dissociation products. The total fraction of the evaporation products decreases to less than 10 % and the $MgOH^+(H_2O)$ ion becomes the dominant product with increasing photolysis energy. These dependencies of the reactive fractions on the photolysis energy are quite similar to those for n=2. In contrast, for n=4 and 5, the primary products such as $MgOH^+(H_2O)_3$ and $MgOH^+(H_2O)_4$ could not be detected. Instead, the signals of $MgOH^+(H_2O)_{n-2}$, which are produced through the intracluster reaction followed by further evaporation of a water molecule, were most intensely observed as the reaction product. Thus the H-atom loss products seem to be the short-lived reaction intermediates in the $Mg^+(H_2O)_{4,5}$ photodissociation and cannot be detected within the present experimental time domain. The branching ratios for n=4 and 5 are shown in Figures IV-13 and IV-14, respectively. Interestingly, the total fractions of intracluster reaction for these ions are almost constant in the photolysis energy range examined as in the case for n=1.

The threshold behaviors for the $MgOH^+(H_2O)$ production from $Mg^+(H_2O)_3$ in Figure IV-12 and for the $MgOH^+(H_2O)_2$ production from $Mg^+(H_2O)_5$ in Figure IV-14, respectively are also seen as in the case for $MgOH^+$. From these threshold energies, we could determined the successive binding energies of $MgOH^+(H_2O)_{n-1}$ as 43 kcal/mol (1.9 eV) for n=2 and 35 kcal/mol (1.5 eV) for n=3, respectively, which are much larger than those for $Mg^+(H_2O)_n$. The difference between the hydration energies for $Mg^+(H_2O)_n$ and those for $MgOH^+(H_2O)_{n-1}$ may be responsible for the first intensity alternation at n=5 in the mass spectrum of nascent cluster ions shown in

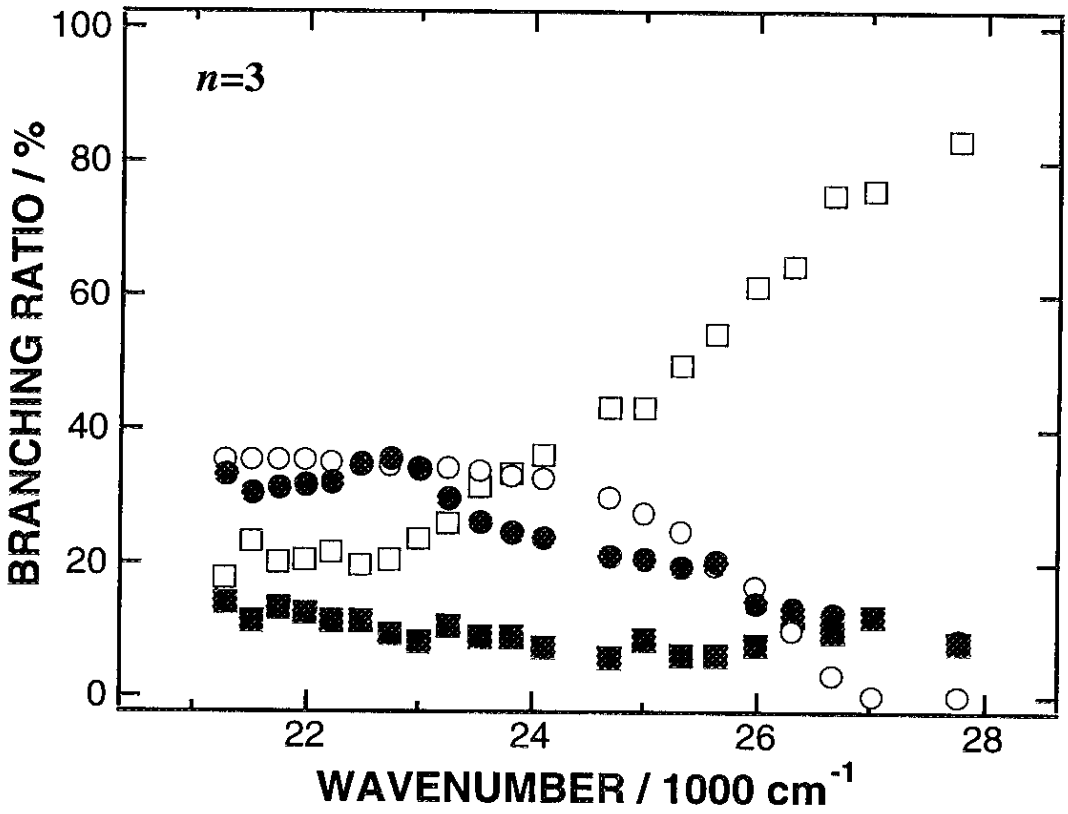

Figure IV-12. Branching ratios of $Mg^+(H_2O)$ (■), $Mg^+(H_2O)_2$ (●), $MgOH^+(H_2O)$ (□), and $MgOH^+(H_2O)_2$ (○) produced by the photodissociation of $Mg^+(H_2O)_3$ plotted vs. photon energy from 21000 to 28000 cm^{-1}.

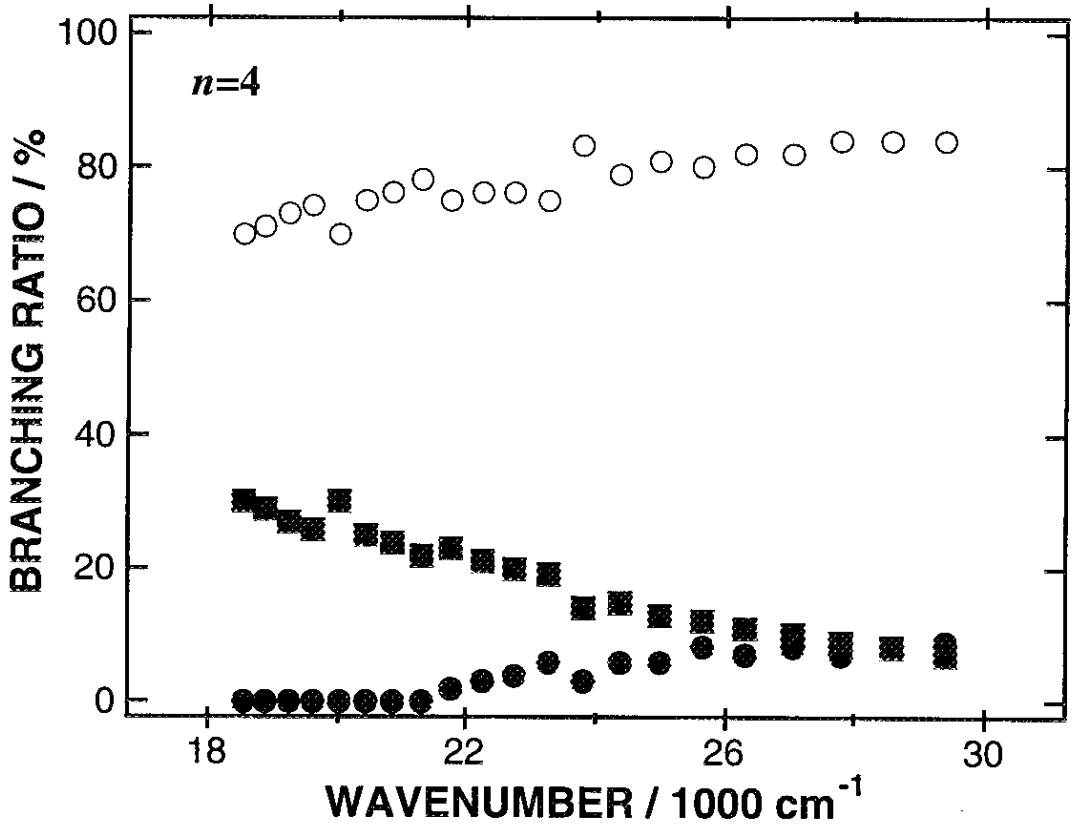

Figure IV-13. Branching ratios of $Mg^+(H_2O)$ (■), $Mg^+(H_2O)_2$ (●), and $MgOH^+(H_2O)_2$ (○) produced by the photodissociation of $Mg^+(H_2O)_4$ plotted vs. photon energy from 19000 to 30000 cm^{-1}.

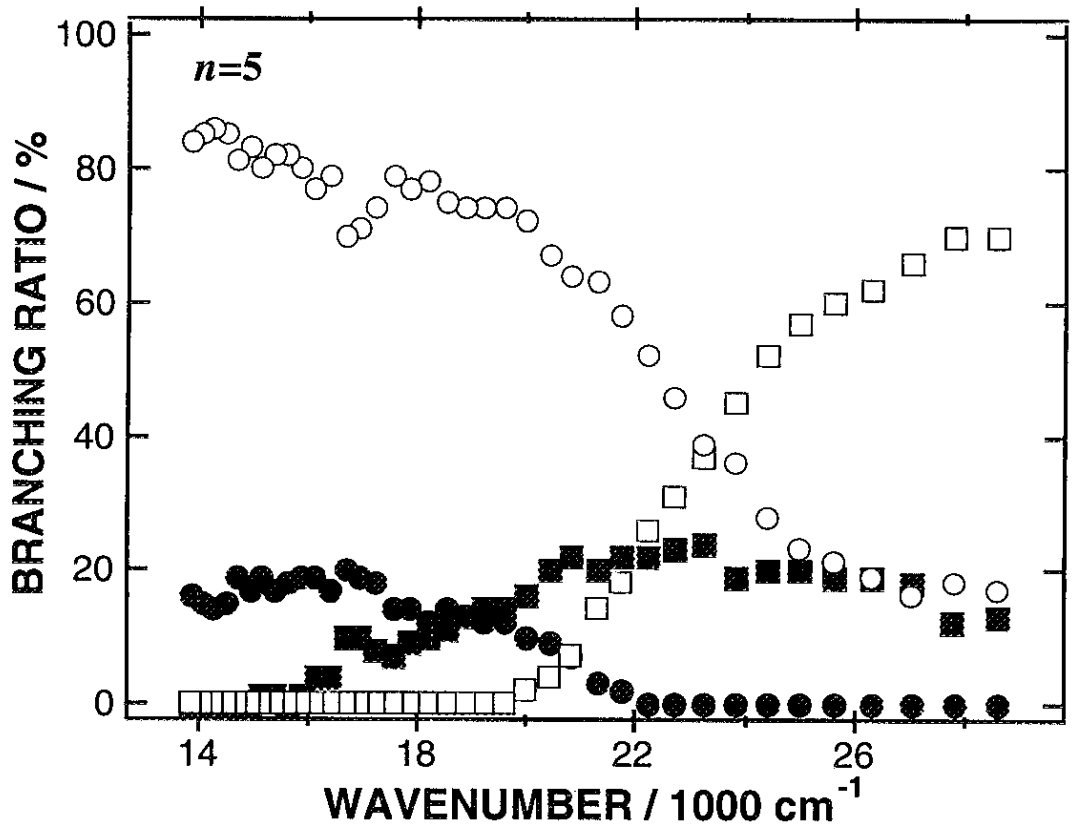

Figure IV-14. Branching ratios of $Mg^+(H_2O)_2$ (■), $Mg^+(H_2O)_3$ (●), $MgOH^+(H_2O)_2$(□), and $MgOH^+(H_2O)_3$(○), produced by the photo-dissociation of $Mg^+(H_2O)_5$ plotted vs. photon energy from 13800 to 29000 cm^{-1}.

Figures IV-3 and IV-4. Details of the anomalous mass distribution of the parent ions will be discussed in Chapter VI.

IV-3.4. Photodissociation Spectra of $Mg^+(H_2O)_n$

Figure IV-15 shows photodissociation spectra of size-selected $Mg^+(H_2O)$ (250-370 nm) and $Mg^+(H_2O)_2$ (280-470 nm). Each point in these spectra represents the total yield of fragment ions averaged over 500 laser shots, and it is also normalized to the fluence of the photolysis laser and to the fragment ion intensity produced with 308-nm photolysis. The spectra have characteristic features: For $Mg^+(H_2O)$, the spectrum consists of an intense band at 30500 cm^{-1} (3.78 eV) with a weak shoulder at 28300 cm^{-1} (3.51 eV), and another band at 38500 cm^{-1} (4.77 eV). The ratio of the integrated absorption intensities of these two bands is about 2:1. For n=2, the spectrum shifts further to the red and an intense overlapped band is observed at 30500 cm^{-1} (3.78 eV) in addition to a band appeared around 25000 cm^{-1} (3.10 eV).

Photodissociation spectra of $Mg^+(H_2O)_n$, n=1-5, are depicted in Figure IV-16. These spectra were also obtained by taking total yield of fragment ions as a function of photolysis wavelength. The intensities of the spectra are normalized at their peak positions. The dissociation spectrum for n=3 consists of two main bands and exhibits the smallest band width; the higher-energy band is observed at about 28500 cm^{-1} which is shifted by ca. 2000 cm^{-1} from that for n=2. However, the lower-energy peak does not shift appreciably with addition of the third water molecule. Small redshifts of these bands from those for n=3 were observed for n=4 and 5, and a weak shoulder appears at ca. 17000 cm^{-1} for n=5. The author could not obtain dissociation spectra for n=6 and larger cluster ions because of the low abundance of these ions in the parent-ion beam as noted in Section IV-3.1. The spectra for this entire series of clusters show significant redshift relative

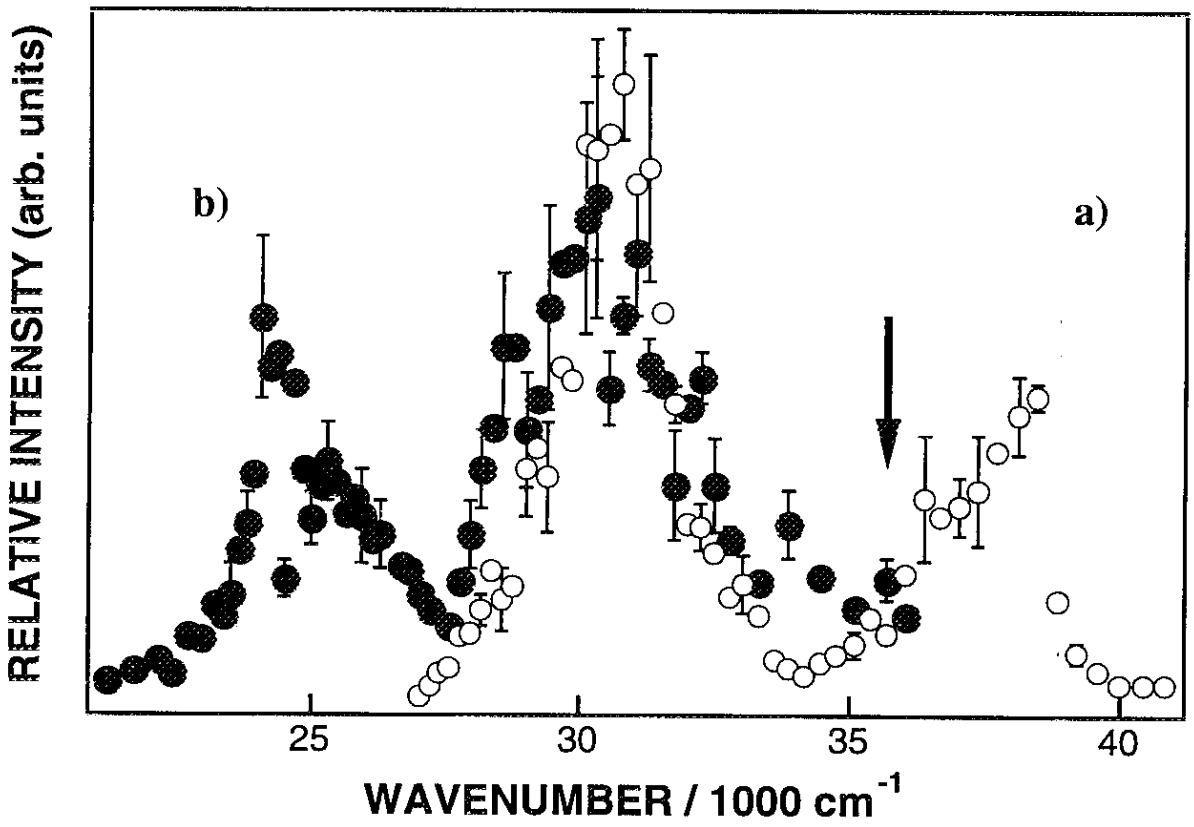

Figure IV-15. Photodissociation spectra of (a) $Mg^+(H_2O)$ and (b) $Mg^+(H_2O)_2$. The intensities of the spectra are normalized at their peak positions. The position of the Mg^+ ^2P-^2S transition is shown by an arrow.

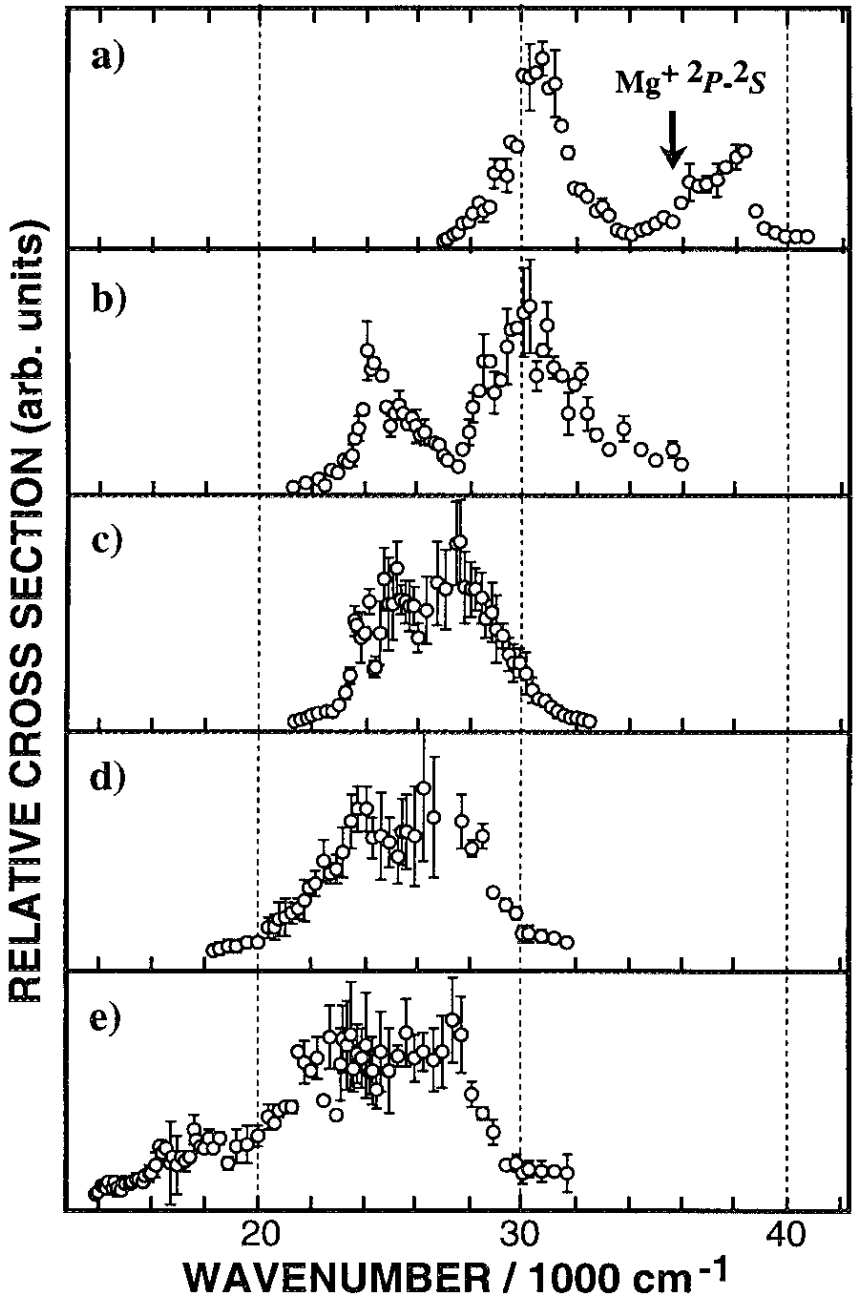

Figure IV-16. Photodissociation spectra of $Mg^+(H_2O)_n$ with n=1 (a) to 5 (e). These are obtained by taking into account the total yield of the fragment ions. The intensities of the spectra are normalized at their peak positions.

to the atomic resonance lines of Mg^+ near 35700 cm^{-1} and exhibit the stepwise shell formation around the Mg^+ ion as discussed later.

IV-3.5. Time-resolved photodissociation

In order to understand the kinetic mechanism and the dynamics of the photoinduced reaction, it is important to examine the excited-state lifetime and photodissociation time for each clusters. These data are also quite informative to understand the microscopic aspect of solvation dynamics in bulk solution. Because condensed-phase processes involve numerous many-body interactions, dynamical information is often highly collisionally averaged. The study of dynamical processes in size-selected clusters affords an opportunity to separate intrinsic dynamics from the perturbations of solvent molecules. From this point of view, recently, Farrar and his co-workers have examined the time dependence of the $Sr^+(NH_3)_2 \rightarrow Sr^+(NH_3) + NH_3$ photodissociation process [44]. They determined the dissociation time of this cluster by using a picosecond pump-probe technique combined with the reflectron mass spectrometer: The $Sr^+(NH_3)$ daughter and Sr^+ granddaughter ions were detected as a function of the delay time between the pump and probe laser pulses. Though the technique they used is the best way to examine the time dependence of the photodissociation of mass-selected cluster ions, the time constant obtained includes both the excited-state decay and the dissociation times; it is rather difficult to measure these time constants, independently.

As mentioned in the previous sections, the photoexcitation of $Mg^+(H_2O)_n$ induces both the evaporation and the intracluster reaction to produce hydrated $MgOH^+$ ions. To clarify the kinetic mechanism and dynamics of these processes, information on the excited-state decay process is indispensable as well as that for the total dissociation time. Fortunately, as

for the $Mg^+(H_2O)_n$ photodissociation, two-photon process to produce the $MgOH^+$ ion is found to occur for n=2 in the energy region below 29000 cm^{-1} (see Sections IV-3.2. to IV-3.4.). As mentioned later, the Mg^+ ^2D-^2S transition occurs at 71491 cm^{-1} [45] and thus, the excitation energy of the allowed ^2D-^2P transition is almost the same as the ^2P-^2S level spacing (35700 cm^{-1}). As in the case of the Mg^+ ion, the ^2D-^2P type transition of $Mg^+(H_2O)_2$ is expected to be strongly allowed and readily promotes the ions to higher electronically excited states located well above the reaction threshold energy. Therefore, the two-photon process is ascribed to the $MgOH^+$ production via the high-lying excited states derived from the ^2D level as a result of the absorption of one more photon by $Mg^+(H_2O)_2(^2P)$. Since the ^2D-^2P excitation and other deexcitation such as radiative transition and internal conversion are the competitive processes in the first excited state, the excited-state decay can be probed by the detection of the $MgOH^+$ ions formed through the above process.

In the present study, the lifetime of the first excited state for $Mg^+(H_2O)_2$ is measured by a pump-to-probe experiment for the $MgOH^+$ ions. Figure IV-17 shows schematically the experimental setup for the time-resolved pump-probe study. The photolysis laser is a dye laser pumped by a pulsed Nd:YAG laser with a 4 ns pulse width. The pulse width is minimized by adjusting the Q-switch timing. The laser fluence is ca. 40 mJ/cm^2. A mirror is placed from 20 to 280 cm from the chamber center line to provide the appropriate delay as well as to double pass the laser beam and improve the signal-to-noise ratio. With this experimental configuration, the fluence of the probe pulse is about 70 % of that for the pump laser. The dynamical information regarding the excited-state decay of $Mg^+(H_2O)_2$ is obtained with pump-probe delays of up to 12 ns by moving the mirror.

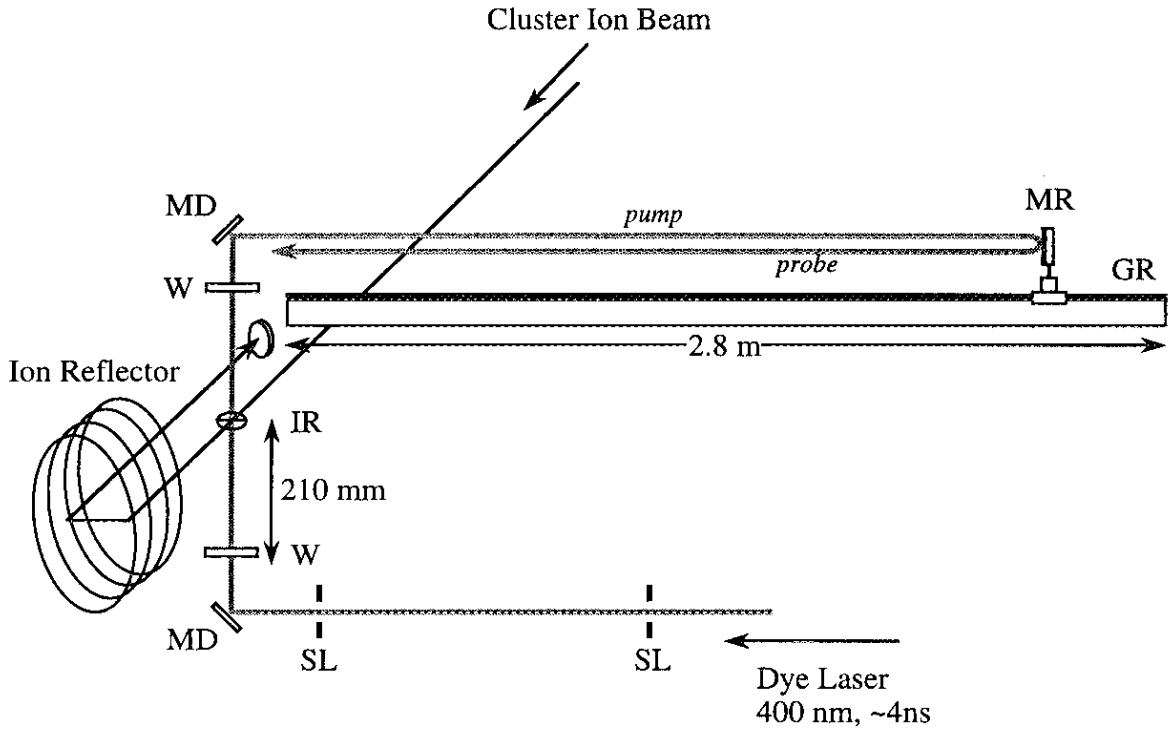

Figure IV-17. Experimental setup for the time-resolved measurement of photodissociation with using the 4-ns pulsed laser. This setup provides the pump-probe delay of 1.4-20 ns. GR: optical guide rail; MD: dielectric mirror (99.9%); SL: slit; MR: reflection mirror (Al coating, ~76%); W: chamber window (CaF_2); IR: laser beam-ion beam interaction point.

The data are acquired by recording the mass spectrum containing the fragment ions, $MgOH^+$ and $Mg^+(H_2O)$, with the digital oscilloscope and averaging 500 shots to obtain an acceptable signal-to-noise ratio. The excited-state lifetime is obtained by taking the amount of photodissociation product as a function of the pump-probe delay time. Figure IV-18 shows the results for the time-resolved photodissociation of the $Mg^+(H_2O)_2$ ions obtained at the photolysis energy close to the peak of the first absorption band (ca. 400 nm in Figure IV-15b). In order to take into account for shot-to-shot variations in the cluster source, the $MgOH^+$ signal is normalized to the sum of the $MgOH^+$ and $Mg^+(H_2O)$ signals and then subtracted the background signals due to the pump pulse; the ordinate of Figure IV-18 represents $R=R_{on}-R_{off}$, where R_{on} and R_{off} are the normalized signals with and without the pump pulse, respectively. The data are shown with a fit to an exponential decay function having a time constant of 2.6 ns. Since the temporal width of the dissociation laser is 4 ns, the result of the decay time constant may be qualitative, however, it clearly indicates the excited-state decay time is on the nanosecond time scale.

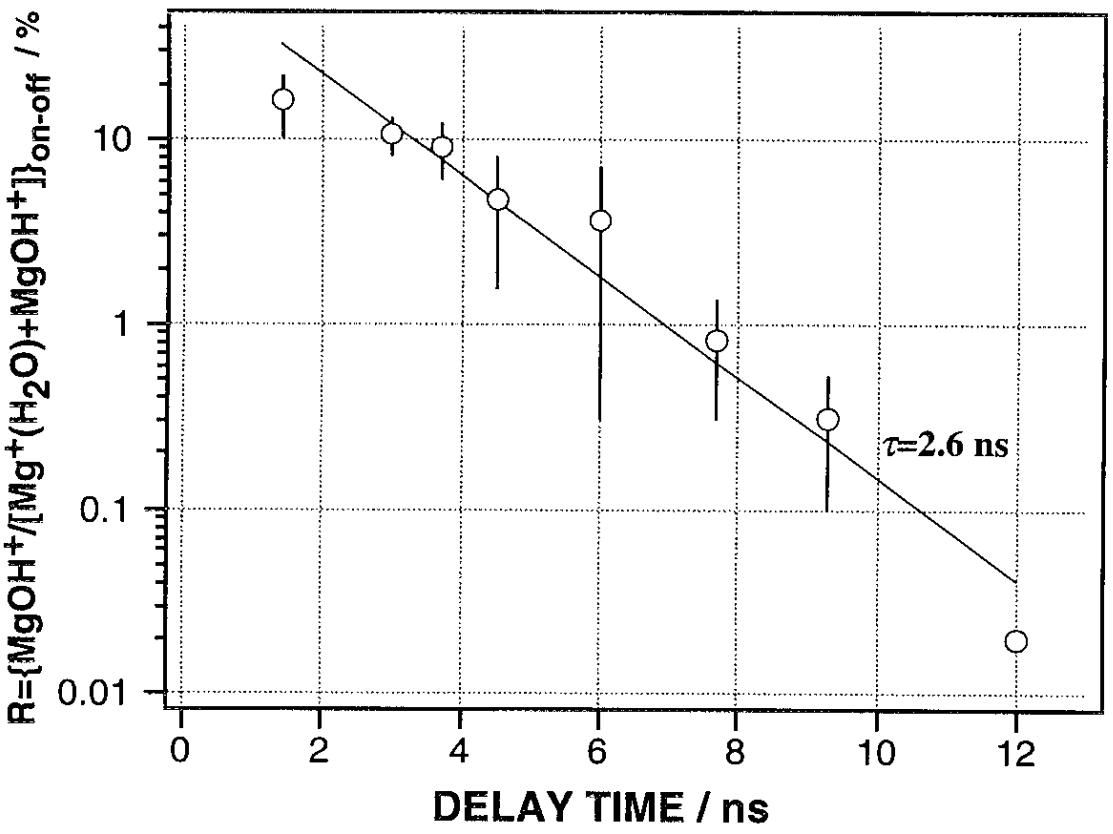

Figure IV-18. The intensity ratio, R, of $MgOH^+$ produced at 400 nm by two-photon photodissociation of $Mg^+(H_2O)_2$ as a function of pump-probe delay. The ratio is normalized to the sum of $MgOH^+$ and $Mg^+(H_2O)_2$ signals and subtracted the background signals due to the pump pulse: $R=R_{on}-R_{off}$. The dashed line is a single-exponential decay fitted with a time constant of 2.6 ns.

IV-4. Discussion

IV-4.1. Electronic structure of $Mg^+(H_2O)_n$

The bond dissociation energy of Mg^+-H_2O determined by photodissociation was reported to be 60 kcal/mol (2.6 eV) [27], which is consistent with 56 ± 5 kcal/mol estimated on the basis of the correlation of Mg^+ affinity with proton affinity [26]. The Mg^+–H_2O binding energy was also estimated to be 0-24 kcal/mol from the photodissociation of Mg^+(ROH) for a number of ligands [26]. On the other hand, the recent theoretical study has predicted the binding energy as 36 ± 5 kcal/mol (1.6(2) eV) [29], which is consistent with the present calculations (37 kcal/mol). Although the values of the binding energy reported hitherto disperse rather widely, the excitation energy examined here is higher than these values, and thus it is energetically possible to examine the excited state of the $Mg^+(H_2O)_{1,2}$ by the present photodissociation technique. As for the larger clusters, the binding energy for $Mg^+(H_2O)_{n-1}$–H_2O becomes much smaller as predicted theoretically by Bauschlicher *et al.* [29,35] and Iwata *et al.* [53]. Therefore the photodissociation spectra for the larger clusters may also correspond to their absorption spectra.

$Mg^+(H_2O)$ The photodissociation spectrum of $Mg^+(H_2O)$ exhibits a shoulder at 28300 (3.51 eV) and two distinct peaks at 30500 (3.78) and 38500 cm^{-1} (4.77 eV), as shown in Figure IV-15a. To first order, the ground state of the Mg^+ ion is a pure $^2S_{1/2}$ state, and excitation to the p orbitals results in the $^2P_{3/2}$ and $^2P_{1/2}$ excited states; these atomic transitions in Mg^+ occur at 35669 and 35761 cm^{-1} with a spin-orbit splitting of 92 cm^{-1} [45]. Interaction of the Mg^+ ion with a water molecule causes splitting of three p orbitals. If a C_{2v} symmetry is assumed for the structure of $Mg^+(H_2O)$, the ground state of the

$Mg^+(H_2O)$ ion is the totally symmetric $^2A_1$ state, arising from interaction of the 3*s* atomic orbital with the lone pair orbital on H_2O, while the excited states are the $^2A_1(z)$, $^2B_1(x)$, and $^2B_2(y)$ symmetries with the *z* axis as the molecular axis (*x* axis is assigned to the out-of-plane axis after the Mulliken symbols). The observed bands may correspond to the transitions from the ground state to these excited states. In order to interpret the observed spectrum in detail, the potential energy curves of the ground and excited states of $Mg^+(H_2O)$ were calculated by using the *ab initio* CI method. The optimized geometry of the ground state $Mg^+(H_2O)$ ($^2A_1$) is planar with C_{2v} symmetry (see Figure IV-19a) and agrees with the results predicted by Bauschlicher and Partridge (BP) [29,31]. The potential energy curves of the ground and excited electronic states as a function of $R_{Mg\text{-}O}$ are also shown in Figure IV-20. The vertical excitation energies of the lowest three excited states, $^2B_2$, $^2B_1$, and $^2A_1$, are found to be 27900 (3.46), 30000 (3.72), and 38400 cm^{-1} (4.76 eV), respectively. These results are in excellent agreement with the observed peak positions. Thus, as a result of complex formation, the lowest two transitions for n=1 are found to be redshifted with respect to the Mg^+ ^2P-^2S transition by 7400 and 5200 cm^{-1}, while the third one is blue-shifted by 2800 cm^{-1}. And also, the calculated oscillator strengths, which are predicted to be nearly the same for the three transitions, seem to be consistent with the observed intensity ratio (2:1) for the 30500- and 38500-cm^{-1} bands as shown in Figure IV-15a; the lowest two transitions overlap each other in the photodissociation spectrum. Recently, the excited electronic states and the binding energies of Mg^+-ligand clusters were also studied theoretically for several ligand molecules by BP. According to their work on $Mg^+(H_2O)$, vertical excitation energies of the lowest three transitions are 3.62 ($p\pi$, in plane), 3.87 ($p\pi$, out of plane), and <4.82 eV ($p\sigma$). These results are

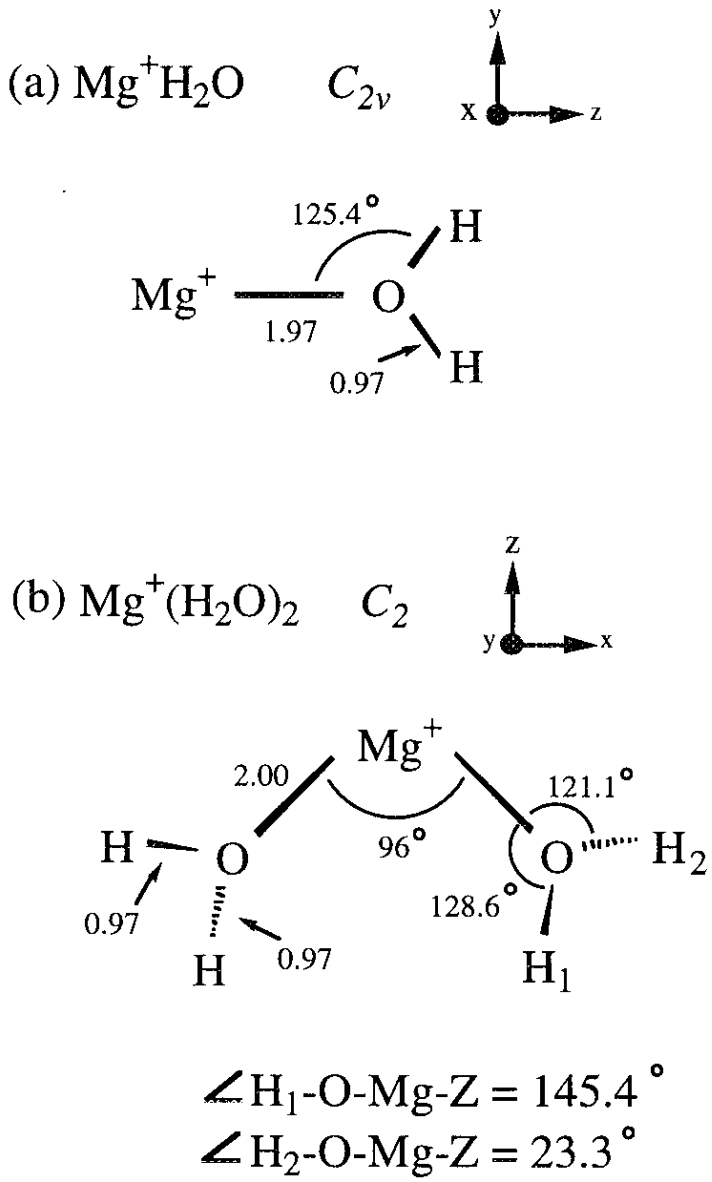

Figure IV-19. Optimal structures of (a) Mg^+H_2O and (b) $Mg^+(H_2O)_2$. Distances are shown in angstroms.

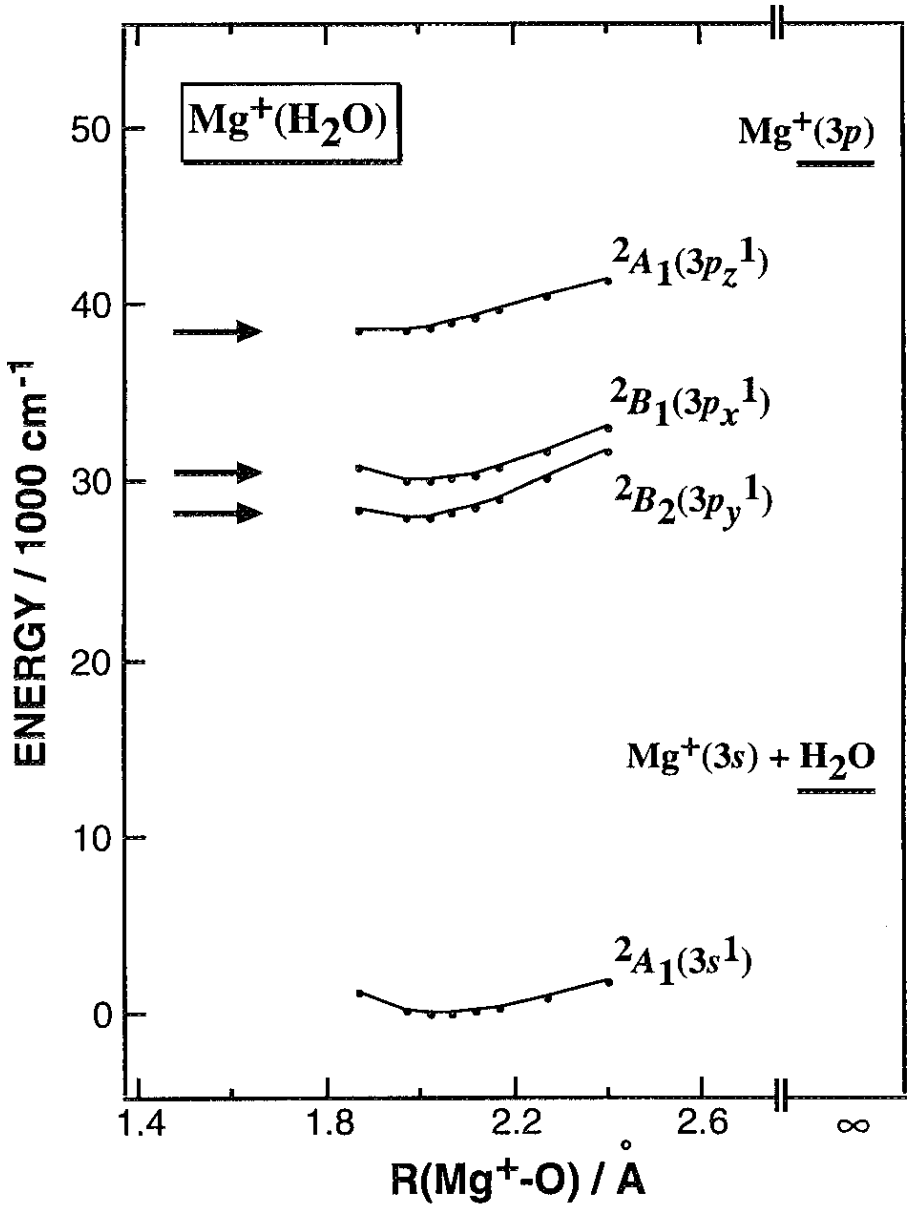

Figure IV-20. Calculated potential energy curves of the ground and the excited states for $Mg^+(H_2O)$ as a function of the Mg-O distance. Observed peak positions are shown by arrows.

consistent with both the observed and calculated values determined in the present study.

$Mg^+(H_2O)_2$ As shown in Figure IV-15b, the photodissociation spectrum of $Mg^+(H_2O)_2$ changes drastically from that of $Mg^+(H_2O)$; an absorption band peaks at 25000 cm^{-1} (3.10 eV) and a broad intense band at ~30000 cm^{-1} (3.72 eV) . In order to interpret this spectrum, we also calculated the structure and transition energies of the $Mg^+(H_2O)_2$ ion were also calculated. The optimal geometry is a bent structure (C_2 symmetry) with two waters staggered as shown in Figure IV-19b. This bent structure shows marked contrast to those of $M^+(H_2O)_2$ (M=Ca and Sr), in which O-M-O configurations are linear [35]. This difference is ascribed to the $sd\sigma$ hybridization for the latter two ions whereas *sp* hybridization for $Mg^+(H_2O)_2$ [35]. The vertical transition energies are found to be 3.14 (1^2B ($3p_y$) - ^2A), 3.73 (2^2B ($3p_x$) -1^2A) and 4.18 eV (2^2A ($3p_z$) -1^2A), whereas those reported by Bauschlicher *et al.* are 3.29, 3.89, and <4.34 eV, respectively [35]. The potential energy curves, similar to Figure IV-20, are obtained and those of the excited states are found to be all bound in the symmetric Mg-O stretching coordinate. The observed photodissociation spectrum for n=2 (Figure IV-15b) agrees well with these predictions: the band peak at 25000 cm^{-1} corresponds to the transition to the 1^2B state and the broad intense band at ca. 30000 cm^{-1} is probably due to the overlapped transitions to the higher two electronic states (2^2B and 2^2A). Relative intensities of these bands also agree with the theoretical transition probabilities (almost 1:1:1 in our calculation in order from lower energy transition and 3.44:3.36:2.01 in Ref. 35). The observed spectral shifts from n=1 to 2 seem to be consistent with the theoretically predicted structures of these complexes: one of the two $3p\pi$ orbitals, which are nearly degenerate for n=1, is raised in energy by large

amount when the second water is coordinated to form the bent structure (nearly 90° O-Mg-O angle). This trend in the spectral shift is clearly seen in Figure IV-15b, in which one of the overlapped bands for n=1 shows relatively small redshift (less than 2000 cm^{-1}), while the other two bands shift to the red as large as 7000 cm^{-1}. Therefore, we can reasonably assign the observed bands in the photodissociation spectrum to the ^2P-^2S type transitions localized on the Mg^+ ion.

Photodissociation spectra for the larger clusters The theoretical transition energies are not available for n=3 and larger cluster ions. However, based on the results for n=1 and 2, the bands observed for n=3 (Figure IV-16c) can be safely assigned to the transitions localized on Mg^+. The observation that the splitting in these transitions for n=3 is much smaller than those for n=1 and 2 may be explained as follows. Figure IV-21 shows the optimized geometries for n=2-4 calculated by the *ab initio* method [31,35]. As seen in this figure, up to three water molecules directly coordinate to the Mg^+ ion, and the $Mg^+(H_2O)_3$ ion has an equilibrium structure with C_3 symmetry in which three equivalent waters coordinate to Mg^+ with nearly 90° O-Mg-O angles. In this configuration, the $p\pi$-like 1^2B state of n=2 mentioned previously is also destabilized by metal-ligand interaction with nearly the same amount as those for 2^2B and 2^2A, leading to much closer excitation energies for three excited states. For n=4, two stable structures have been proposed [31]; one is the structure in which all four water molecules coordinate to Mg^+ from the same side, and another is that in which the fourth water coordinates to two of the three first-shell water molecules of the $Mg^+(H_2O)_3$ ion (Figure IV-21c). These are denoted as the (4+0) and the (3+1) structures, respectively. The similarity of the dissociation spectrum for n=4 (Figure IV-16d) to that for n=3 implies that the effect of the fourth water

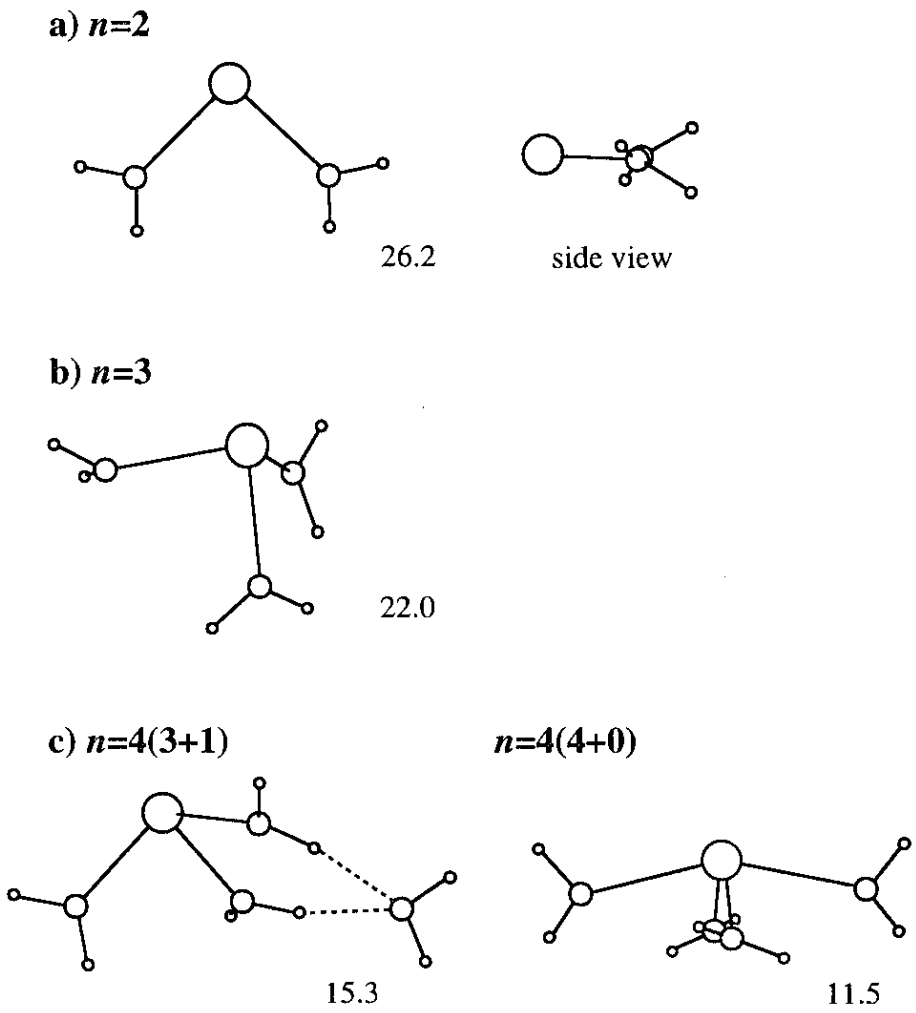

Figure IV-21. Optimal structures of $Mg^+(H_2O)_n$ (n=2-4) calculated by Bauschlicher *et al.* (see Ref. 31). The successive binding energies of these structures are given in kcal/mol. As for n=4, the (3+1) structure is more stable than the (4+0) structure.

on the electronic structure of the Mg^+ ion is quite small, which probably supports the (3+1) structure. Though the theoretical work on the equilibrium structure for n=5 is not available at present, three possible structures can be considered by analogy with the above $Mg^+(H_2O)_4$ structures: (5+0), (4+1), and (3+2) structures in line with the designation noted above. The tail extending to about 14000 cm^{-1} in the n=5 dissociation spectrum (Figure IV-16e) may indicate the existence of at least two isomers in the above three candidates.

Recently, Donnelly and Farrar have studied the photodissociation spectra of $Sr^+(NH_3)_n$, n=1-6 [43]. They found a large spectral shift with increasing cluster size; the spectrum of n=6 is redshifted in energy by about 17000 cm^{-1} with respect to the Sr^+ resonance lines at 23715 ($0_{1/2}$) and 24517 cm^{-1} ($1_{1/2}$). To interpret the size evolution of the dissociation spectra, they carried out a spectral moment analysis of the dissociation cross sections, which indicates a large increase in the electronic radial distribution in the electronic ground state with increasing cluster size. On the basis of these results, they suggested an increasing Rydberg character of cluster states that correlate with 5*s* and 5*p* atomic orbitals on Sr^+; ion-pair character in the ground and excited state wave functions of the metal increases with increasing cluster size. However, in the case of Sr^+, the ^2D level lies below ca. 10000 cm^{-1} from the ^2P level and the presence of the states derived from the former level may hamper the definite assignment of the observed spectra and a rigorous moment analysis: a strong mixing of these states as a result of complex formation may also lead to a large spectral redshift. Bauschlicher and his co-workers have calculated the ground-state geometries, binding energies, and transition energies of $Sr^+(NH_3)_n$, n=1-3 [35]. They predicted the strong mixing of the above mentioned states, which could explain the observed large spectral shifts. In contrast, the ^2D level of Mg^+ lies at 35800

cm^{-1} above the ^2P level and the mixing between these levels by the complex formation is negligibly small as predicted by theoretical calculations[35]. Though the $Mg^+(H_2O)_n$ ions also exhibit spectral redshifts as large as 17000 cm^{-1} with respect to the Mg^+ resonance line (^2P-^2S), these shifts are mostly due to the destabilization of the ground state as a result of metal-ligand repulsion.

IV-4.2. Photodissociation processes of $Mg^+(H_2O)_n$

In the photodissociation of $Mg^+(H_2O)_n$, fragment ions formed by two different processes such as the evaporation and intracluster reaction are observed in the mass spectrum as mentioned previously: $Mg^+(H_2O)_m$ and $MgOH^+(H_2O)_{m-1}$ ions are produced by the former and the latter processes, respectively. These two processes are competitive in nature, and its branching ratio depends strongly on both the photolysis wavelength and cluster size. To make the discussion clear, the two processes are separately discussed in the following paragraphs.

Evaporation mechanism As exemplified in Section IV-3.5, the deexcitation rate of these clusters is rather slow (on the order of 10^8 s^{-1} for the first excited state of n=2) and the radiative process is also expected to take part in the decay processes, especially for n=1 and 2. The reason why the dissociation time is so slow in comparison with that of a small molecule (picosecond time regime) can be ascribed to the bound nature of the excited-state clusters as predicted by the theoretical calculations (see Section IV-4.1). As a result, the dissociation dynamics is predissociative in character and the fast internal conversion from the excited states to higher vibrational levels of the electronic ground state above its dissociation limit is followed by evaporation of water molecules. For n=2 and larger clusters, one or more

water molecules evaporate by one-photon excitation. The evaporation mechanism may be similar to that for n=1 as follows,

$$Mg^+(H_2O)_n + h\nu \rightarrow [Mg^+(H_2O)_n]^* \quad \text{(IV.5)}$$

$$[Mg^+(H_2O)_n]^* \rightarrow [Mg^+(H_2O)_n]^\dagger \quad \text{(IV.6)}$$

$$[Mg^+(H_2O)_n]^\dagger \rightarrow Mg^+(H_2O)_{n-1} + H_2O \quad \text{(IV.7)}$$

$$\rightarrow Mg^+(H_2O)_{n-2} + 2H_2O, \quad \text{(IV.8)}$$

where $[Mg^+(H_2O)_n]^*$ and $[Mg^+(H_2O)_n]^\dagger$ denote the cluster ions in the initially excited state and in the higher vibrational levels of the ground electronic state (see Figure IV-22). As for the process to produce $Mg^+(H_2O)_{n-2}$, two mechanisms such as sequential and simultaneous evaporation of two H_2O molecules are possible. However, as seen in Figures IV-13 (n=4) and IV-14 (n=5), the branching ratios of $Mg^+(H_2O)_{n-2}$ increase at the same rate as the decrease of $Mg^+(H_2O)_{n-1}$ with increasing photon energy. Thus, these results strongly suggest that the sequential evaporation occurs in the higher vibrational levels of the ground electronic state.

Farrar and his co-workers have also argued about the evaporation mechanism for $Sr^+(NH_3)_n$ [43,44]. Based on the observation that the dissociation cross section for $Sr^+(ND3)$ is an order of magnitude smaller than that for $Sr^+(NH_3)$, they proposed a bond-stretch attraction model, in which an ion-pair state such as $Sr^{2+}(NH_3)^-$ is assumed to mediate the electronic to vibrational energy transfer. This model is applicable for the electronic quenching of an excited-state metal atom having a low ionization potential. Although they did not take into account the low-lying excited states derived

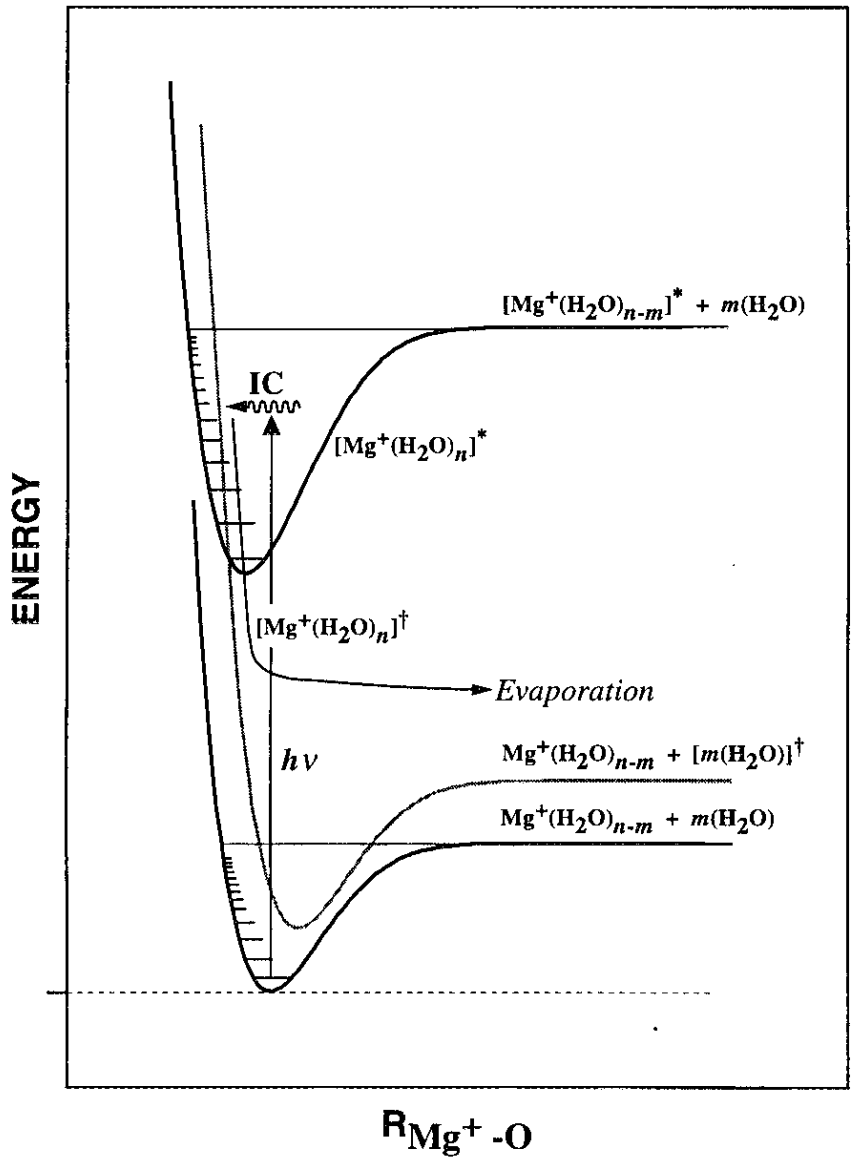

Figure IV-22. Schematic potential curves for the dissociation of $Mg^+(H_2O)_n$. The excited state has bound character. The evaporation of water molecules is predissociative in character and occures from the higher vibrational levels of the electronic ground state.

from the ^2D asymptote of Sr^+, these excited states may also be deeply involved in the dissociation of these clusters: The states correlated to ^2D may mediate the quenching process to the ground state. As for $Mg^+(H_2O)_n$, the above mechanism seems to be less important especially for n=1, because the ionization potential of $Mg^+(^2P)$ is higher than 10 eV and the electron affinities of water clusters with $n \leq 5$ are almost zero or negative [1,2]. I also examined the deuterium substitution effect on the relative dissociation cross section for $Mg^+(H_2O)_{1,2}$ and found no significant difference. Although information about the potential energy surfaces of crossing region is lacking at the moment, a direct internal conversion process yielding the higher vibrational levels of the ground electronic state seems to be responsible for the evaporation process of $Mg^+(H_2O)_n$. The slow decay rate mentioned above seems to support these considerations.

Energetics and Dynamics of Intracluster Reaction One of the interesting features of the $Mg^+(H_2O)_n$ photodissociation is the intracluster reaction to produce the hydrated $MgOH^+$ ions, which depends strongly on both the excitation wavelength and cluster size. To gain insight into this reaction mechanism, we examined the photodissociation of $Mg^+(H_2O)_n$ by carefully adjusting the voltage applied on the deceleration and reflection plates of the reflectron so as to detect the H-atom loss products as well with the same collection efficiency. The $MgOH^+(H_2O)_{n-1}$ ion is found to be formed predominantly as the primary product of this reaction for n=1 and 2 as shown in Figures IV-8 and IV-9. This is also true for larger clusters, though the branching fraction is much smaller than those for n=1 and 2 as mentioned below. The energetics and dynamics of the intracluster reaction including the primary product will be discussed in the following paragraphs.

n=1 Reaction As for $Mg^+(H_2O)$, the process to produce $MgOH^+$ ions as well as the evaporation is energetically possible with the present photolysis energy ranging from 3.35 to 5.06 eV: The ground states of Mg^+ and $MgOH^+$ lie at 1.6 and 3.5 eV, respectively, above the ground-state $Mg^+(H_2O)$ as discussed below. Two possible mechanisms may be considered for this reaction: one is the ground-state channel, in which cluster ions cross back from the initially accessed excited state to higher vibrational levels of the ground electronic state, followed by the reaction, and the other is the direct excited-state channel. Unfortunately, there is no theoretical study on the excited-state channel for this reaction. However, Stwalley and his co-workers have recently studied the photodissociation spectrum of jet-cooled MgD_2^+ by detecting the reactive fragment product, MgD^+ [46]. They observed discrete vibrational transitions with an averaged spacing of ca. 400 cm^{-1}, superimposed on a broad continuum background in the red region of the Mg^+ resonance line. In connection with this work, Bauschlicher has carried out the *ab initio* CI calculations on the optimal geometries and binding energies for the ground- and excited-state MgH_2^+ [36]. The three excited states arising by exciting 3*s*-like electron into 3*p* orbitals are found to be all bound relative to their asymptote: the $^2B_1$ (out-of plane) and $^2B_2$ (in-plane) states are more strongly bound. Interestingly, he found that the bonding in the $^2B_2$ state is very different from the others: The Mg^+ ion is found to insert into the H-H bond for this state, due to the strong interaction of in-plane $3p\pi$ orbital of Mg^+ and H_2 σ^* orbital. Based on these theoretical results, Stwalley's group assigned the discrete bands to the transition to the $^2B_1$ state and the broad underlying continuum to the $^2B_2$ state, in which a direct and rapid reaction proceeds. If the similar state-specific reaction channel is opened for $Mg^+(H_2O)$, the author can expect a strong wavelength dependence in the branching ratio for the evaporation and the reaction processes. However, the

observed branching ratio is almost constant in the wavelength region examined (see Figure IV-8). Duncan and his co-workers [38] also studied the photodissociation spectrum of jet-cooled $Mg^+(H_2O)$ and observed the well resolved rovibronic bands for both the 1^2B_2-1^2A_1 and 1^2B_1-1^2A_1 transitions. Although it is difficult to estimate the precise excited-state lifetime from the rotational bandwidth because they used a low-resolution dye laser (ca.1 cm^{-1}), these results imply that , for $Mg^+(H_2O)$, such a fast reaction as that for Mg^+D_2 does not take place in its excited states.

On the other hand, the reactivity of the $Mg^+(H_2O)$ on the ground-state surface is evident from the following considerations. As mentioned previously, the hydrated $MgOH^+$ ions are predominant products for $n \geq 5$ in the parent-ion mass spectrum (see Figure IV-3). In the cluster beam source, both $Mg^+(^2S)$ and $Mg^+(^2P)$ ions may be produced by the laser vaporization process. However, the radiative lifetime of $Mg^+(^2P)$ (reported to be 3.7 ns) [47] is too short to take part in the parent-ion production, and thus, almost all of the hydrated $MgOH^+$ ions observed in the mass spectrum are produced through collision of $Mg^+(^2S)$ with water clusters. Although there is no direct experimental evidence to rule out the excited-state channel, these arguments as well as the observed constant fraction of $MgOH^+$ production in the $Mg^+(H_2O)$ photodissociation seem to suggest the ground-state channel for the H-atom elimination reaction for n=1.

The above arguments imply that the evaporation and intracluster reaction are the competitive processes in the deexcitation of higher vibrational states on the ground-state surface. The results of the branching ratio shown in Figure IV-8 indicate no barrier in the H-atom elimination reaction: This is consistent with the theoretical threshold energy to produce $MgOH^+$ from $Mg^+(H_2O)$, as mentioned previously. Though the $MgOH^+$ production is the dominant process in the present excitation energy region, the Mg^+ ion

produced via the evaporation process is detected as much as 5-10%. This result implies that the reaction may take place with rather slow rate, partly because the reaction proceeds just above the reaction barrier as it is expected from the theoretical threshold energy. In the reaction of an excited-state metal atom with a water molecule, two possible mechanism such as an abstraction reaction to produce metal hydrate and an insertion reaction to produce metal hydroxide can be considered: In a full-collision reaction studies, the long-lived insertive intermediate is known to be involved [48]. The fact that we could not detect MgH^+, in addition to the rather slow reaction rate mentioned above, suggests an insertion-type mechanism for the $MgOH^+$ production [49].

n=2 Reaction As for n=2, the photoinduced reaction also produces both the $MgOH^+$ and $MgOH^+(H_2O)$ ions. The laser-fluence dependence predicts the two-photon process for the $MgOH^+$ production in the energy region below the threshold (29000 cm^{-1}), though the ions are predominantly produced by a one-photon process at the energies above this threshold as shown in Figure IV-11. The author should note that the Mg^+ ^2D-^2S transition occurs at 71491 cm^{-1} [45], and thus, the excitation energy of the allowed ^2D-^2P transition is almost the same as the ^2P-^2S level spacing. As in the case of the Mg^+ ion, the ^2D-^2P type transition of $Mg^+(H_2O)_2$ is expected to be strongly allowed and readily promotes the ions to higher electronically excited states located well above the reaction threshold energy. The two-photon behavior below the threshold can be reasonably understood by this mechanism (see Figure IV-23). Thus, $[Mg^+(H_2O)_2]^*$ produced by process (IV.5) is subsequently excited as follows,

$$[Mg^+(H_2O)_2]^* + h\nu \rightarrow [Mg^+(H_2O)_2]^{**}. \qquad \text{(IV.9)}$$

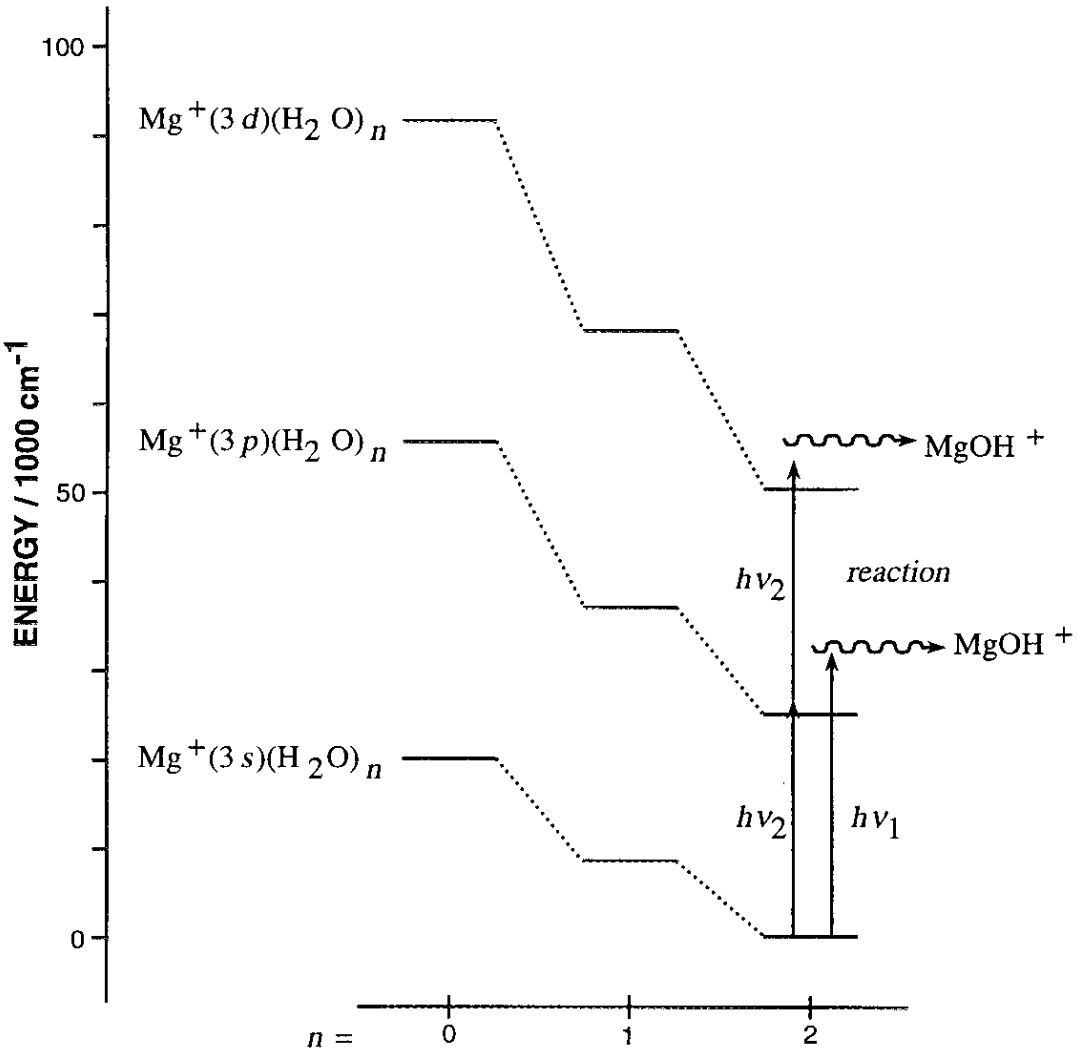

Figure IV-23. Schematic energy diagram of the photoexcitation processes of $Mg^+(H_2O)_2$.

Because the two-photon energy is at least 3 eV larger than the formation threshold of $MgOH^+$, most of the ions excited by two-photon absorption is considered to be dissociated to the stable $MgOH^+$ ion, i.e.,

$$[Mg^+(H_2O)_2]^{**} \rightarrow MgOH^+ + H + H_2O. \qquad \text{(IV.10)}$$

A rough estimate of the upper limit of the rate for the internal conversion process (IV.6) can be obtained on the basis of the above arguments. In the energy region below the reaction threshold, process (IV.6) competes with the depopulation by the subsequent excitation through the ^2D-^2P type transition as shown by process (IV.9), in which the $MgOH^+$ ions are produced presumably as the sole product by the following process (IV.10). Then, the fraction, R=[$MgOH^+$]/([Mg^+]+[$Mg^+(H_2O)$]), is given by the relationship $R=\sigma_{D\text{-}P}\Phi/k$, where Φ is the laser photon flux in unit of photons $cm^{-2}s^{-1}$, k is the rate of process (IV.6) in s^{-1}, and $\sigma_{D\text{-}P}$ is the absorption cross section of the ^2D-^2P transition, typically, on the order of 10^{-16} cm^2 [42,47]. A typical R~30 % fraction (as shown in Figure IV-6) with laser flux of 10^{24} photons $cm^{-2}s^{-1}$ (0.5 mJ/cm^{-2} per 10-ns pulse) near 400 nm yields k on the order of 10^8 s^{-1}. The estimated value agrees qualitatively with the lifetime of the first excited state determined by the time-resolved photodissociation experiment. Since the radiative rate for the ^2P-^2S type transition of $Mg^+(H_2O)_2$ should be comparable to that for the free ion, 2.7×10^8 s^{-1}, the initially excited cluster ions may depopulate through both the radiative process and the process (IV.6). These results seem to be consistent with the rather small photodissociation cross sections mentioned previously. The value may imply that the internal conversion process (IV.6) is the rate-determining step in the photodissociation of $Mg^+(H_2O)_2$ below the threshold.

In the present study, we found that the branching fraction of the H-atom loss process to produce $MgOH^+(H_2O)$ increases with increasing the photolysis energy up to 29500 cm^{-1} as shown in Figures IV-9 and IV-10. Notably, this process is found to occur almost exclusively at the energy close to the peak of the overlapped band, indicating the occurrence of rapid reaction. Since the lower-energy transition of the overlapped band at ca. 30000 cm^{-1} is assigned to the excitation of 3*s* electron into the out-of-plane $3p\pi$ orbital, the features in the $Mg^+(H_2O)_2$ photodissociation are quite similar to those for MgD_2^+ discussed in the previous section. As mentioned above, the $MgOH^+$ ions are produced by two-photon process via the processes (IV.9) and (IV.10) in the energy region below 29000 cm^{-1}, though at higher energy only one photon is needed. The former process was ascribed to the $MgOH^+$ production via the high-lying excited states derived from the ^2D level as a result of the absorption of one more photon by $Mg^+(H_2O)_2(^2P)$. Interestingly, switching from two-photon to one-photon process occurs abruptly when the photolysis energy exceeds above this energy as shown in Figure IV-24, indicating a significant shortening of the lifetime of the latter state. Although there are two possible candidates such as the ground- and excited-state channels as in the case of n=1, the above results seem to suggest the excited-state channel for the reaction of n=2 at least in the energy region above 29000 cm^{-1}. Since MgH^+ and/or $MgH^+(H_2O)$ could not be detected , the reaction mechanism may be insertive as is discussed for n=1.

In the case of the insertion reaction, the degree of overlap between the Mg^+ $3p\pi$ orbital and the σ^* orbital of a ligand is critical in the barrierless reaction. As for $Mg^+(H_2O)_2$, it seems to be difficult to expect a large overlap between the Mg^+ $3p\pi$ orbital and the σ^* orbital of a ligated water, if the excited-state geometry is similar to the bent structure predicted theoretically for the ground state. However, as noted in the experimental section, clusters

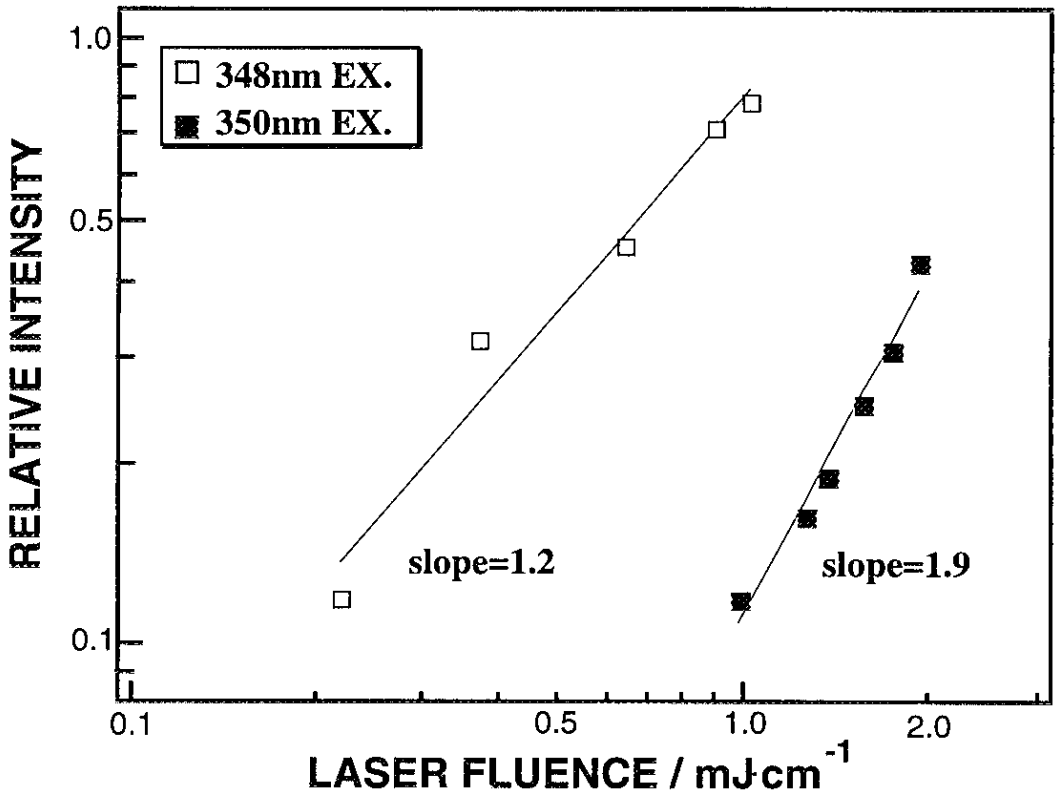

Figure IV-24. Photolysis-laser-fluence dependencies of the $MgOH^+$ fragment ion signals in the dissociation of $Mg^+(H_2O)_2$ at (a) 348 (□) and (b) 350 nm (■). The results of the least-square fittings are shown by the straight lines. From these results, abrupt switching from the two-photon (b) to one-photon (a) processes was observed around these wavelengths.

presently produced are rather hot and it may sample a wide range of geometries in the initially accessed excited state including those favored for the insertion reaction. On the other hand, the ground-state channel as discussed for n=1 may be responsible for the $MgOH^+(H_2O)$ production in the energy region below 27000 cm^{-1}, where the 1^2B (in-plane) state is located and the orbital alignment is quite unfavorable for the insertion reaction. The large fraction of the evaporation products as seen in Figure IV-9 in addition to much slow decay rate estimated for this state (on the order of 10^8 s^{-1}) seems to support the above expectation. At this moment, there is no clear answer why the excited-state channel is opened for n=2 and not for n=1.

The energetics of the processes is next considered as follows,

$$[Mg^+(H_2O)_2]^\dagger \rightarrow MgOH^+(H_2O) + H \qquad \text{(IV.11)}$$

$$\rightarrow MgOH^+ + H + H_2O \qquad \text{(IV.12)}$$

The heat of formation of the $MgOH^+$ ion from $Mg^+(H_2O)_2$ can be deduced from the thermochemical data and partly from the results of the theoretical calculations. As shown in Figure IV-25, this energy, ΔE, is given by

$$\Delta E = D(Mg^+H_2O\text{-}H_2O) + D(Mg^+\text{-}H_2O) + D(H\text{-}OH) - D(Mg^+\text{-}OH), \qquad \text{(IV.13)}$$

where D(A-B) denotes the dissociation energy of the bond between A and B. The dissociation energy of water, D(H-OH), is 5.16 eV [50]. $D(Mg^+\text{-}OH)$ was reported to be 3.3(3) eV by Knudsen cell mass spectroscopy [51], which is in good agreement with the recent photodissociation results, 3.25 (17) eV

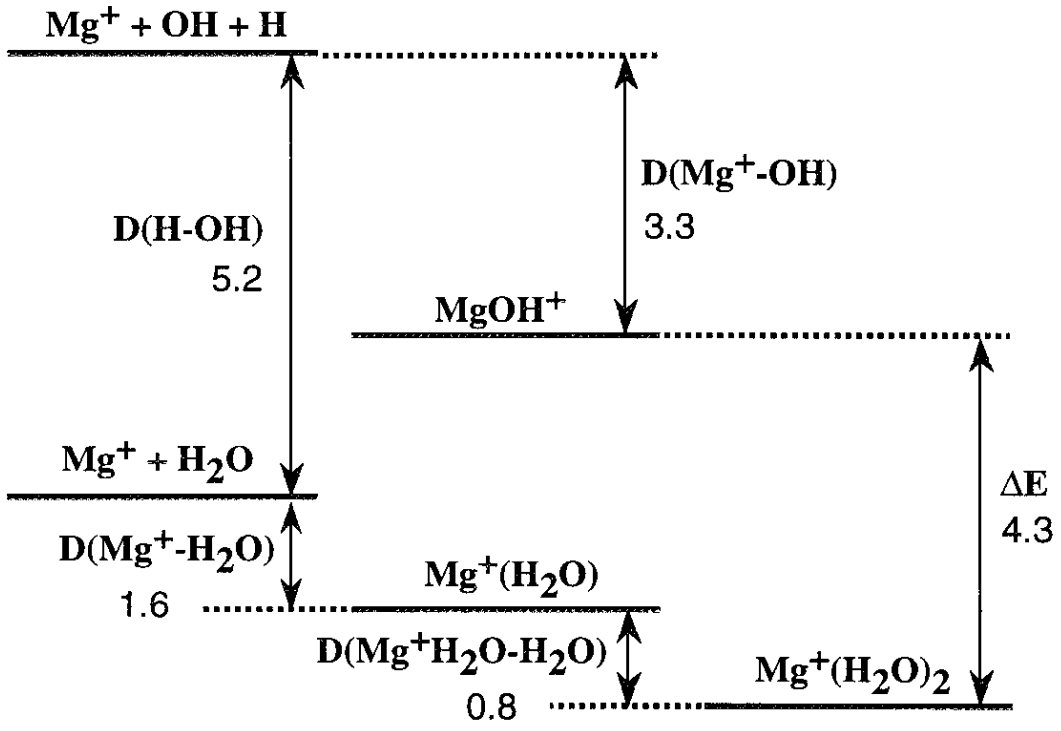

Figure IV-25. Schematic energy diagram of $Mg^+(H_2O)_2$, $Mg^+(H_2O)$, and $MgOH^+$. All values are in units of eV.

[27]. Reliable values for the dissociation energies of $Mg^+(H_2O)$ and $Mg^+(H_2O)_2$ have not been obtained experimentally so far; the value determined by photodissociation is inconsistent with that obtained by displacement reaction as noted in Section IV-4.1. Therefore, the author adopted the calculated binding energies, 1.6(2) eV for $D(Mg^+\text{-}H_2O)$ and 0.8(2) eV for $D(Mg^+H_2O\text{-}H_2O)$, obtained in the present study. Consequently, eq. (IV.13) gives the heat of formation of $MgOH^+$ as 4.3 eV. This value is about 0.7 eV higher than the appearance energy of $MgOH^+$ (3.6 eV) determined in the present measurement. One possible explanation for this discrepancy is the internal excitation of parent ions. The hot Mg^+ ions incipiently produced by laser vaporization may be cooled insufficiently by subsequent collision during the formation of hydrated ions. Therefore the parent $Mg^+(H_2O)_2$ ion may have rather high internal energy with an upper limit corresponding to the dissociation energy, $D(Mg^+H_2O\text{-}H_2O) = 0.8$ eV. If this energy is consumed for the dissociation, the total appearance energy, which is equal to 4.4 eV, shows a good agreement with the estimation. As pointed out by Shen and Farrar [42] and by Liu and Lisy [52], internal excitation in the clusters produced by pick up source is estimated to be about 15-20 kcal/mol (0.65-0.87 eV). The present cluster source of laser vaporization may be under the similar condition because a condensation channel was not used in the present experiment.

As shown in Figure IV-12, the photodissociation of $Mg^+(H_2O)_3$ yields $Mg^+(H_2O)_{1,2}$ and $MgOH^+(H_2O)$ as the major fragment ions. Figure IV-12 shows the branching ratios of these fragment ions including the primary reaction product, $MgOH^+(H_2O)_2$. The onset of rise in $MgOH^+(H_2O)$ fraction at 22600 cm^{-1} (2.80 eV, 64.6 kcal/mol) corresponds to the threshold energy of evaporation from the primary reaction product,

$$MgOH^+(H_2O)_2 \rightarrow MgOH^+(H_2O) + H_2O \qquad (IV.14)$$

as noted in Section IV-3.2. Since the three excited states for n=3 are almost overlapped, it is rather difficult to see the excited-state dependence of branching fraction for the reaction. However, as seen in Figure IV-12, $Mg^+(H_2O)_{1,2}$ and $MgOH^+(H_2O)_{1,2}$ are the major fragment ions in the energy region below 24000 cm^{-1}, while $MgOH^+(H_2O)$ is the predominant product in the energy region above 26000 cm^{-1}, where the second and third excited states are located. These features are quite similar to those for the $Mg^+(H_2O)_2$ photodissociation. Therefore, the mechanism of intracluster reaction for n=3 is considered to be similar to that for n=2.

The author also performed the similar photodissociation experiments for the $Mg^+(H_2O)_4$ and $Mg^+(H_2O)_5$ ions and the results of branching ratio are shown in Figures IV-13 and IV-14, respectively. The photodissociation of $Mg^+(H_2O)_4$ yields only three fragment ions such as $Mg^+(H_2O)_{1,2}$ and $MgOH^+(H_2O)_2$, while $Mg^+(H_2O)_5$ yields $MgOH^+(H_2O)_{2,3}$ and $Mg^+(H_2O)_{2,3}$. As seen in Figure IV-14, the fraction of $MgOH^+(H_2O)_2$ increases rapidly in the energy region above 20600 cm^{-1}, indicating the occurrence of the following evaporation process as

$$MgOH^+(H_2O)_3 \rightarrow MgOH^+(H_2O)_2 + H_2O \qquad (IV.15)$$

In both cases, the primary products such as $MgOH^+(H_2O)_3$ and $MgOH^+(H_2O)_4$ could not be detected, because the threshold energies of the evaporation of a water molecule from these ions are much lower than the present photolysis energy range [53]. In contrast to the cases for n=2 and 3, the fractions of intracluster reaction for n=4 and 5 show no characteristic dependence on the photolysis wavelength as in the case for n=1; the fraction

of reaction for n=5 is the sum of the $MgOH^+(H_2O)_2$ and $MgOH^+(H_2O)_3$ fragments. A statistical RRKM calculation predicts a slow increase in the rate of evaporation from n=2 to 4 [54]. Thus the rather large fraction of evaporation seen in Figures IV-13 and VI-14 (about twice larger than that for n=1) may imply that the rates of intracluster reaction for n=4 and 5 do not change appreciably from that in the first excited state for n=3. The fact that the fractions of the reaction products are independent of the photolysis-energy might suggest the absence of the excited-state reaction channel. One of the possible reasons for the suppression of the excited-state reaction channel may be the enhancement of internal conversion by the presence of second shell water molecules. However, it may be premature to discuss further the mechanism of the reaction for n=4 and 5 with the branching-ratio data alone. In order to get further insight into the dynamics of intracluster reaction, it seems to be necessary to carry out a real-time measurement of the excited-state decay rate as well as the theoretical calculations of the reactive potential surfaces.

IV-5. Conclusion

I have investigated the photodissociation spectra and photodissociation dynamics of $Mg^+(H_2O)_n$ (n=1-5) using a reflectron-type TOF mass spectroscopy coupled with laser spectroscopy. The photodissociation spectra are found to exhibit large redshifts with increasing cluster size and show the clear evolution of solvation shell closing at n=3. The spectra for n=1 and 2 were well reproduced by the *ab initio* CI calculations. The observed absorption bands were assigned to the ^2P-^2S type transitions mainly localized on Mg^+. Although the spectra undergo a large redshift as large as 17000 cm^{-1} with respect to the Mg^+ resonance line, these spectral changes are mostly due to an electrostatic interaction instead of a charge-transfer type interaction.

Both the sequential evaporation of water molecules and the intracluster reaction yielding H-atom loss products are found to be involved in the photodissociation of $Mg^+(H_2O)_n$. The fact that the low-lying excited states of these clusters are all bound in nature along the Mg-O stretching coordinate suggests that the former process proceeds via higher vibrational levels, lying above the dissociation barrier in the ground state and being redistributed through a fast internal conversion process.

The intracluster reaction, yielding $MgOH^+(H_2O)_{n-1}$ as the primary products, is found to occur efficiently for $n \leq 3$. The reaction mechanism is considered to be an insertive one, and it seems to depend strongly on the number of ligated waters and the photolysis energy. As for $Mg^+(H_2O)$, the branching fraction of this reaction is independent of the photolysis energy and the reaction seems to take place on the ground-state surface. In contrast, the reaction cross section for $Mg^+(H_2O)_2$ depends on the photolysis energy and shows a strong enhancement at the energy above 28600 cm^{-1}, which corresponds to the onset energy of the transition to the out-of-plane 2^2B state.

And also the results of the laser-fluence-dependence experiment indicate the opening of new excited-state decay channel above this energy. These results as well as the results for MgD_2^+ reported recently by Stwalley's group suggest that the reaction proceeds directly through the 2^2B state (and probably 2^2A too). In contrast, the low-lying 1^2B state seems to be nonreactive and the reaction is considered to take place on the ground-state surface after crossing back from the initially excited state through a fast internal conversion process as in the case for n=1. This conclusion is consistent with the much slower decay rate of this state (on the order of 10^8 s^{-1}). The $Mg^+(H_2O)_3$ ion exhibits the similar tendency for the fractions of the reaction products and its reaction mechanism is discussed in line with those for n=2.

For larger clusters, the fractions of reaction products are independent of the photolysis energy. One of the possible reasons may be that the rapid increase of internal conversion rate enhanced by the second shell water molecule suppresses the excited-state channel.

References for Chapter IV

[1] J. V. Coe, G. H. Lee, J. G. Eaton, H. W. Sarkas, K. H. Bowen, C. Ludewigt, H. Haberland and D. R. Worsnop, *J. Chem. Phys.* **92**, 3980 (1990).

[2] G. H. Lee, S. T. Arnold, J. G. Eaton, H. W. Sarkas, K. H. Bowen, C. Ludewigt and H. Haberland, *Z. Phys.* D **20**, 9 (1991).

[3] R. N. Barnett, U. Landman, C. L. Cleaveland, and J. Jortner, *Phys. Rev. Lett.* **59**, 811 (1987).

[4] R. N. Barnett, U. Landman, C. L. Cleaveland, and J. Jortner, *J. Chem. Phys.* **88**, 4421, 4429 (1987).

[5] U. Landman, R. N. Barnett, C. L. Cleaveland, D. Scharf, and J. Jortner, *J. Phys. Chem.* **91**, 4890, (1987).

[6] R. N. Barnett, U. Landman, C. L. Cleaveland, N. R. Kestner and J. Jortner, *J. Chem. Phys.* **88**, 6670 (1988).

[7] R. N. Barnett, U. Landman, C. L. Cleaveland, N. R. Kestner and J. Jortner, *Chem. Phys. Lett.* **148**, 249 (1988).

[8] H. Haberland, H. -G. Schindler and D. R. Worksnop, *Ber. Bunsenges. Phys. Chem.* **88**, 270 (1984).

[9] H. Haberland, C. Ludewigt, H. -G. Schindler and D. R. Worksnop, *Surf. Sci.* **156**, 157 (1985).

[10] M. Knapp, O. Echt, D. Kreisle, and and E. Recknagel, *J. Chem. Phys.* **85**, 636 (1986).

[11] M. Knapp, O. Echt, D. Kreisle, and and E. Recknagel, *J. Phys. Chem.* **91**, 2601 (1987).

[12] L. A. Posey and M. A. Johnson, *J. Chem. Phys.* **89**, 4807 (1988).

[13] L. A. Posey , M. J. DeLuca, P. J. Campagnola, and M. A. Johnson, *J. Phys. Chem.* **93**, 1178 (1989).

[14] T. Kondow, *J. Phys. Chem.* **91**, 1307 (1987).

[15] F. Misaizu, T. Kondow, and K. Kuchitu, *Chem. Phys. Lett.* **178**, 369 (1991).

[16] I. Dzidic, P. Kebarle, *J. Phys. Chem.* **74**, 1466 (1970).

[17] I. N. Tang, A. W. Castleman, Jr., *J. Chem. Phys.* **57**, 3638 (1972).

[18] I. N. Tang, M. S. Lian, and A. W. Castleman, Jr., *J. Chem. Phys.* **65**, 4022 (1976).

[19] P. M. Holland and A. W. Castleman, Jr., *J. Am. Chem. Soc.* **102**, 6174 (1980).

[20] K. I. Peterson, P. M. Holland, R. G. Keesee, N. Lee, T. D. Märk, and A. W. Castleman, Jr., *Surf. Sci.* **106**, 136 (1981).

[21] P. M. Holland and A. W. Castleman, Jr., *J. Chem. Phys.* **76**, 4195 (1982).

[22] E. Kochanski and E. Constantin, *J. Chem. Phys.* **87**, 1661 (1987).

[23] T. F. Magnera, D. E. David, and J. Michl, *J. Am. Chem. Soc.* **111**, 4100 (1989).

[24] T. F. Magnera, D. E. David, D. Stulik, R. G. Orth, H. T. Jonkman, and J. Michl, *J. Am. Chem. Soc.* **111**, 5036 (1989).

[25] P. J. Marinelli, R. R. Squires, *J. Am. Chem. Soc.* **111**, 4101 (1989).

[26] L. Operti, E. C. Tews, and B. S. Freiser, *J. Am. Chem. Soc.* **110**, 3847 (1988).

[27] L. Operti, E. C. Tews, T. J. MacMahon, and B. S. Freiser, *J. Am. Chem. Soc.* **110**, 9125 (1989).

[28] C. W. Bauschlicher, Jr., S. R. Langhoff, and H. Partridge, *J. Chem. Phys.* **94**, 2068 (1991).

[29] C. W. Bauschlicher, Jr. and H. Partridge, *J. Phys. Chem.* **95**, 3946 (1991).

[30] C. W. Bauschlicher, Jr., S. R. Langhoff, and H. Partridge, J. E. Rice, and A. Komornicki, *J. Chem. Phys.* **95**, 5142 (1991).

[31] C. W. Bauschlicher, Jr. and H. Partridge, *J. Phys. Chem.* **95**, 9694 (1991).

[32] M. Sodupe, C. W. Bauschlicher, Jr. and H. Partridge, *Chem. Phys. Lett.* **195**, 494 (1992).

[33] C. W. Bauschlicher, Jr. and H. Partridge, *Chem. Phys. Lett.* **181**, 129 (1991).

[34] M. Sodupe, C. W. Bauschlicher, Jr. and H. Partridge, *Chem. Phys. Lett.* **192**, 185 (1992).

[35] C. W. Bauschlicher, M. Sodupe, Jr. and H. Partridge, *J. Chem. Phys.* **96**, 4453 (1992).

[36] C. W. Bauschlicher, *Chem. Phys. Lett.* **201**, 11 (1993).

[37] C. S. Yeh, K. F. Willey, D. L. Robbins, J. P. Pilgrim and M. A. Duncan, *Chem. Phys. Lett.* **196**, 233 (1992).

[38] K. F. Willey, C. S. Yeh, D. L. Robbins, J. P. Pilgrim and M. A. Duncan, *J. Chem. Phys.* **97**, 8886 (1992).

[39] N. E. Levinger, D. Ray, K. K. Murray, A. S. Mullin, C. P. Schulz, and W. C. Lineberger, *J. Chem. Phys.* **89**, 71 (1988).

[40] M. H. Shen, J. W. Winniczek, and J. M. Farrar, *J. Phys. Chem.* **91**, 6447 (1987).

[41] M. H. Shen and J. M. Farrar, *J. Phys. Chem.* **93**, 4386 (1989).

[42] M. H. Shen and J. M. Farrar, *J. Chem. Phys.* **94**, 3322 (1991).

[43] S. G. Donnelly and J. M. Farrar, *J. Chem. Phys.* **98**, 5450 (1993).

[44] C. A. Schumuttenmaer, J. Quan, S. G. Donnelly, M. J. DeLuca, D. F. Varley, L. A. DeLouise, R. J. D. Miller, and J. M. Farrar, *J. Phys. Chem.* **98**, 3077 (1993).

[45] *Atomic Energy Levels*; edited by C. E. Moore, Natl. Stand. Ref. Data Ser., NBS 35, Vol. **1** (National Bureau of Standards, Washington DC,1971).

[46] L. N. Ding, M. A. Young, P. D. Kleiber, W. C. Stwalley, and A. M. Lyyra, *J. Phys. Chem.* **97**, 2181 (1993).

[47] A. A. Radzig and B. M. Smirnov, *Reference Data on Atoms, Molecules, and Ions*, Springer Series in Chemical Physics **31** (Springer, Berlin, 1985).

[48] K. Kuwahara, H. Ikeda, H. Umemoto, T. Sato, K. Takano, S. Tsunashima, F. Misaizu, and K. Fuke, *J. Chem. Phys.* **99**, 2751 (1993).

[49] Both the $MgOH^+$ and MgH^+ ions are expected to be produced by the insertion-type reaction. However, the former one may be produced preferentially because of its much higher binding energy; D_O of $MgOH^+$ and MgH^+ were reported to be 74±4 and ~46 kcal/mol in Refs. 26 and 27.

[50] S. G. Lias, J. E. Bartmess, J. F. Liebman, J. L. Holmes, R. D. Levin, and W. G. Mallard, *J. Phys. Chem. Ref. Data Suppl.* **17** (1988).

[51] C. J. Cassady and B. S. Freiser, *J. Am. Chem. Soc.* **106**, 6176 (1984).

[52] W. L. Liu and J. M. Lisy, *J. Chem. Phys.* **89**, 605 (1988).

[53] H. Watanabe, S. Iwata, H. Nakamura, K. Hashimoto, F. Misaizu, and K. Fuke, submitted in *J. Am. Chem. Soc.*

[54] The calculated evaporation rates of $Mg^+(H_2O)_n$ show increasing tendency with the increase of n because of its rather large successive hydration energy.

Chapter V

Photodissociation of $Ca^+(H_2O)_n$ cluster ions

V-1. Introduction

In the past decade, the field of cluster ions has been extended by applying novel experimental measurements [1-4]. Within the broad topics of cluster structure and dynamics, the solvation in fundamental phenomenon is of central importance. The clusters containing metal ions, M^+S_n, play important roles for the reaction both in the gas-phase and in solution. Numerous studies have been devoted to determining the successive hydration energies by high-pressure mass spectrometry and collision induced dissociation experiment [5-12]. Recently, mass-selected photodissociation spectroscopy has been used to study the electronic spectrum of solvated metal ions containing polar solvents, e.g., water and ammonia molecules. The high-resolution photodissociation spectra of the (1:1) complexes, V^+H_2O [13], Co^+CO_2 [14], Mg^+H_2O [15,16], Mg^+CO_2 [17], and Mg^+D_2 [18] have been reported by several groups. On the other hand, in order to bridge the gaps between isolated metal ions and solvated metal ions in bulk solution, the photodissociation spectra for large clusters ($n \geq 2$) have been examined for several systems, $Sr^+(NH_3)_n$ [19-21], $Sr^+(H_2O)_n$ [20,22], and $Mg^+(H_2O)_n$ [23-26] as described in Chapter IV.

In the alkaline-earth metal-polar solvent systems, the central issues are the electronic structures and the formation of the solvent shell, and the intracluster reaction. The large redshifts as large as ~2 eV were observed in the photodissociation spectra of $Sr^+(NH_3)_n$, n=1-6 [21], and $Mg^+(H_2O)_n$, n=1-5 [25]. For the former system, the observed shifts were explained by

increasing character of a Rydberg-like ion-pair state, $M^{2+}S_n^-$, however, they were attributed to the destabilization of orbitals involved in the ^2P-^2S transition for the latter system. In this chapter, the electronic structure and the reactivity of size-selected $Ca^+(H_2O)_n$ ions are examined by the photodissociation technique. In the Mg^+ system, the ^2D state lies far above the ^2P state, while the ^2D state for Ca^+ lies between the electronic ground ^2S and the ^2P states. The excited ^2P states of $Ca^+(H_2O)_n$ is expected to be perturbed by ligand field-induced *d-p* orbital mixing. The photodissociation spectra of $Ca^+(H_2O)_n$ for n=1-6 and the branching ratios of photofragments are examined in this study. On the basis of these results, the electronic structure and the reaction mechanism of $Ca^+(H_2O)_n$ are discussed in conjunction with the *d-p* orbital mixing.

V-2. Experimental

The experimental apparatus and the photodissociation technique for size-selected cluster ions employed in the present study are almost the same as those described in Sections II-2 and IV-2, respectively. The apparatus consists of a laser vaporization cluster-ion source and a reflectron type time-of-flight (TOF) mass spectrometer. The Ca^+ ions were generated by laser irradiation of a rotating Ca rod; the second harmonic of a Nd:YAG laser (Quanta-Ray, GCR-12) was used as the vaporization light source. In the cluster source, the $Ca^+(H_2O)_n$ ions were formed via multiple collisions between the Ca^+ ions and water clusters. The latter clusters were generated by the expansion of water vapor (20 Torr) seeded in 3 atm He from a pulsed valve (General valve, Series 9): The valve was placed 10 mm upstream from the metal rod. The cluster ions were skimmed by a skimmer with 2.5-mm

diameter and introduced into the Wiley-McLaren-type TOF mass spectrometer. After extracting and accelerating by pulsed electric fields (Velonex, 350J/V1735), the ions were focused and deflected into the reflectron TOF mass spectrometer. The cluster ions mass-separated in the first field free region were irradiated with a photolysis laser at right angles to the beam just prior to enter the reflector of the reflectron. The product ions were reaccelerated back into the second field free region and detected by dual microchannel plates (MCP; Hamamatsu, F1552-23S). The signal from the MCP was processed by a digital storage oscilloscope (LeCroy 9450) after being amplified by a preamplifier (NF Electric Instruments, BX-11).

A XeCl excimer pumped dye laser (Lambda Physik, LPX205i/FL2002) and a pulsed Nd:YAG pumped dye laser (Quanta-Ray, GCR-3/PDL-3) were used for photolysis with wavelengths of 330-740 and 835-970 nm, and of 740-835 nm, respectively. As for the wavelength range of 970-1440 nm, the Raman-shifted output of the Nd:YAG pumped dye laser was used: The dye laser output was focused into a high pressure cell (Continuum, RS2) filled with 30 atm H_2.

The photodissociation technique for size-selected ions was described in Sections IV-2.1 and IV-2.2. The photofragment ion signals were obtained by subtracting the background signals due to metastable ions from the total ion signals. The photodissociation spectra were obtained by plotting the total fragment ion signals normalized by the photolysis laser fluence and the parent ion intensity as a function of the photolysis wavelength.

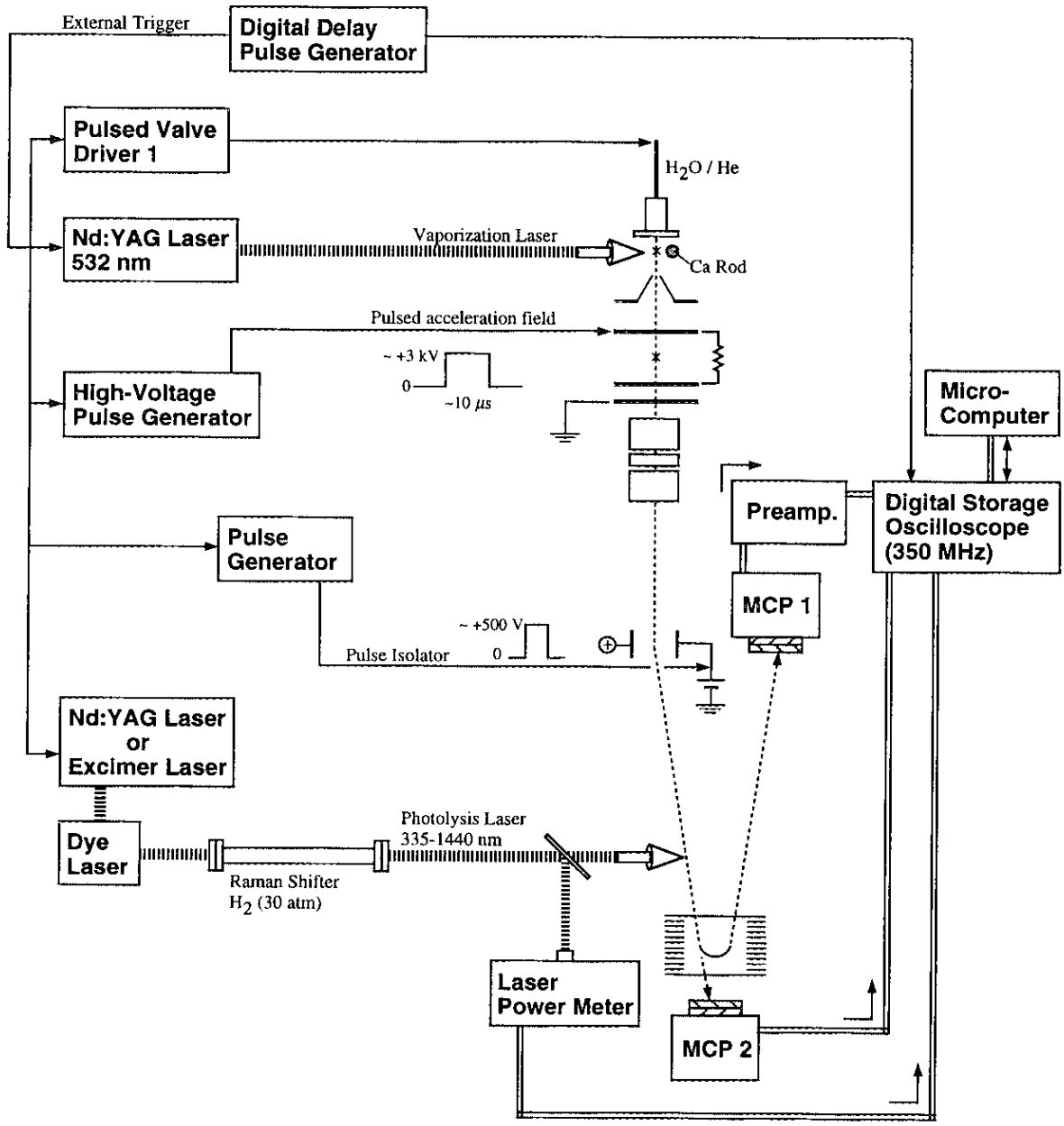

Figure V-1. Block diagram of the laser system and the measurement devices for the study of photodissociation of size-selected $Ca^+(H_2O)_n$, n=1-6.

V-3. Results

V-3.1. Size distribution of parent ions

In the cluster source, both $Ca^+(H_2O)_n$ and $CaOH^+(H_2O)_{n-1}$ ions are formed with characteristic size distributions. In the TOF mass spectrum of the product ions (Figure V-2), the $Ca^+(H_2O)_n$ ions are dominantly observed for $1 \leq n \leq 4$ and $n \geq 13$, while the $CaOH^+(H_2O)_{n-1}$ ions are exclusively observed for $5 \leq n \leq 14$. Though the Ca atom has six isotopes, the abundances of isotopes other than ^{40}Ca are negligibly small, therefore, Ca^+ refers to the most abundant $^{40}Ca^+$ in the following discussion. The similar product distribution is also observed for Ca^+-D_2O and Mg^+-H_2O system. Details on the features of these mass spectra and the mechanism of the product switching are discussed in Chapter VI.

V-3.2. Photodissociation spectra

Figure V-3 shows the photodissociation spectra of size-selected $Ca^+(H_2O)_n$ for n=1-6 in the wavelength range from 330 to 1440 nm. These spectra were obtained by taking the total yield of fragment ions as a function of the photolysis energy. The spectrum for the $Ca^+(H_2O)$ ion consists of two intense bands at 22400 cm^{-1} (2.78 eV) and 28000 cm^{-1} (3.47 eV): the integrated intensity ratio of these bands is about 2:1. The photodissociation spectrum of $Ca^+(H_2O)_2$ shows an intense band at 20000 cm^{-1} (2.48 eV) and a weaker broad band at about 24700 cm^{-1} (3.06 eV). In the case of n=3, an intense overlapped band with a large band width was observed at ca. 17000 cm^{-1} (2.11 eV). The spectra for larger clusters also consist of the single intense band at 12500 cm^{-1} (1.55 eV) for n=4, 9200 cm^{-1} (1.14 eV) for n=5, and 8700 cm^{-1} (1.08 eV) for n=6, respectively. The spectra for this entire series of clusters show significant redshifting relative to the atomic resonance

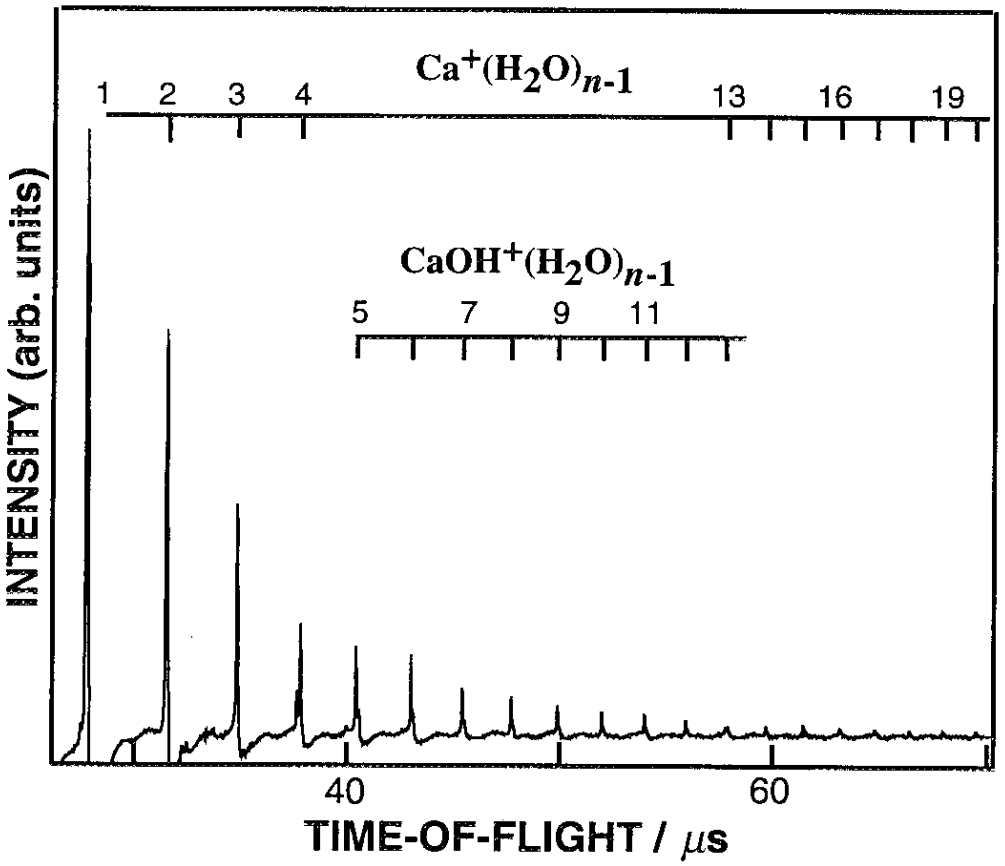

Figure V-2. Typical time-of-flight (TOF) mass spectrum of the nascent cluster ions produced by laser vaporization. The $Ca^+(H_2O)_n$ ions are dominant for $n \leq 4$ and $n \geq 13$, while the $CaOH^+(H_2O)_{n-1}$ is observed exclusively for $5 \leq n \leq 14$.

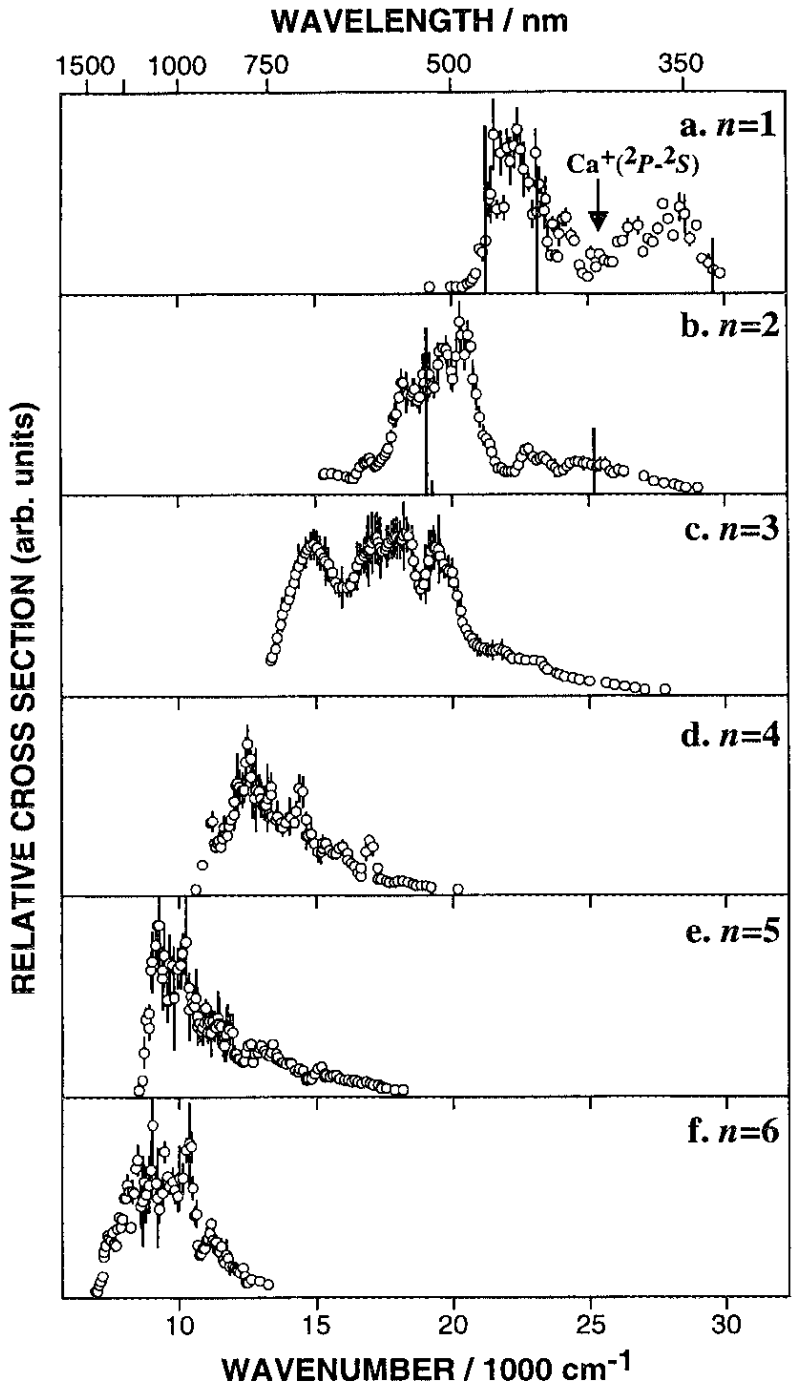

Figure V-3. Photodissociation spectra of $Ca^+(H_2O)_n$ with n=1(a) to 6 (f). These spectra are obtained from the total yield of the fragment ions as a function of photon energy. The dissociation cross sections are normalized at their peaks. An arrow in the figure shows the $Ca^+(^2P\text{-}^2S)$ resonance line. Sticks in the figure represent the theoretical excitation energies and relative transition intensities determined by Bauschlicher and his co-workers.

line (25303 cm^{-1}) as large as 18000 cm^{-1}. And also, the spectral width becomes much sharper with increasing cluster size.

V-3.3. Branching ratios of the photofragment ions

As in the case of $Mg^+(H_2O)_n$, both the evaporation of water molecules and the photoinduced intracluster reaction to produce the hydrated $CaOH^+$ ions, $CaOH^+(H_2O)_m$, were observed as the photodissociation channels for the Ca^+-H_2O system. The branching ratio of each process provides us information on the energetics, mechanisms, and dynamics of the photodissociation processes.

n=1 Photodissociation Figure V-4 shows the branching ratio for the photodissociation of $Ca^+(H_2O)$. As for n=1, the Ca^+ ion is produced dominantly through the evaporation of an H_2O molecule, while the $CaOH^+$ ion formed by the dehydrogenation reaction is a minor product ion. The results for the branching ratio of $CaOH^+$ exhibit the threshold behavior at about 24500 cm^{-1} (3.04 eV). This threshold coincides with the onset of the second absorption band. In Figure V-5, the results on the laser fluence dependence of the $CaOH^+$ ion yield are shown. In the production of $CaOH^+$, two photons are needed in the energy lower than the threshold. The author should note that the Ca^+ ^2D-^2S transition occurs at 56712 cm^{-1} [27], and the excitation energy of the allowed ^2D-^2P transition is almost the same as the ^2P-^2S level spacing. Therefore, the two-photon behavior can be ascribed to the sequential excitation of $Ca^+(H_2O)$ to the higher excited states derived from the ^2D level.

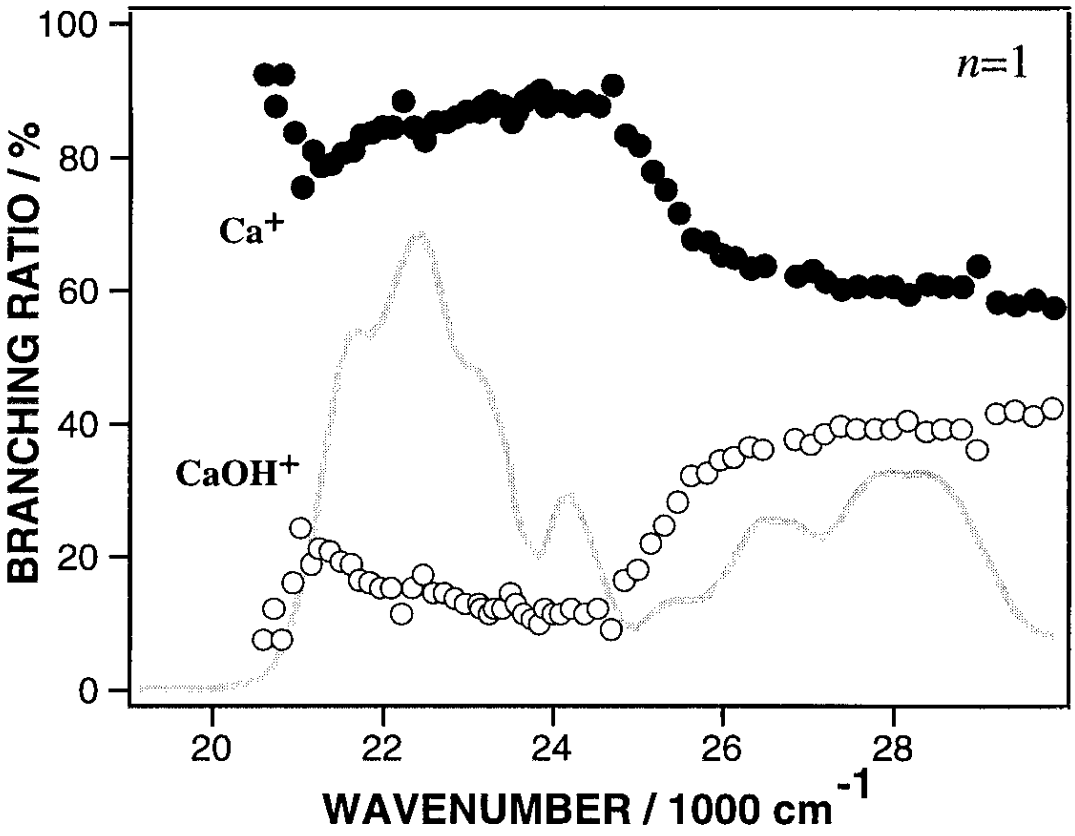

Figure V-4. Branching ratios of Ca^+ (●) and $CaOH^+$ (○) produced by the photodissociation of $Ca^+(H_2O)_2$ plotted as a function of photon energy. The blurred curve in the figure represents the photodissociation spectrum of $Ca^+(H_2O)$.

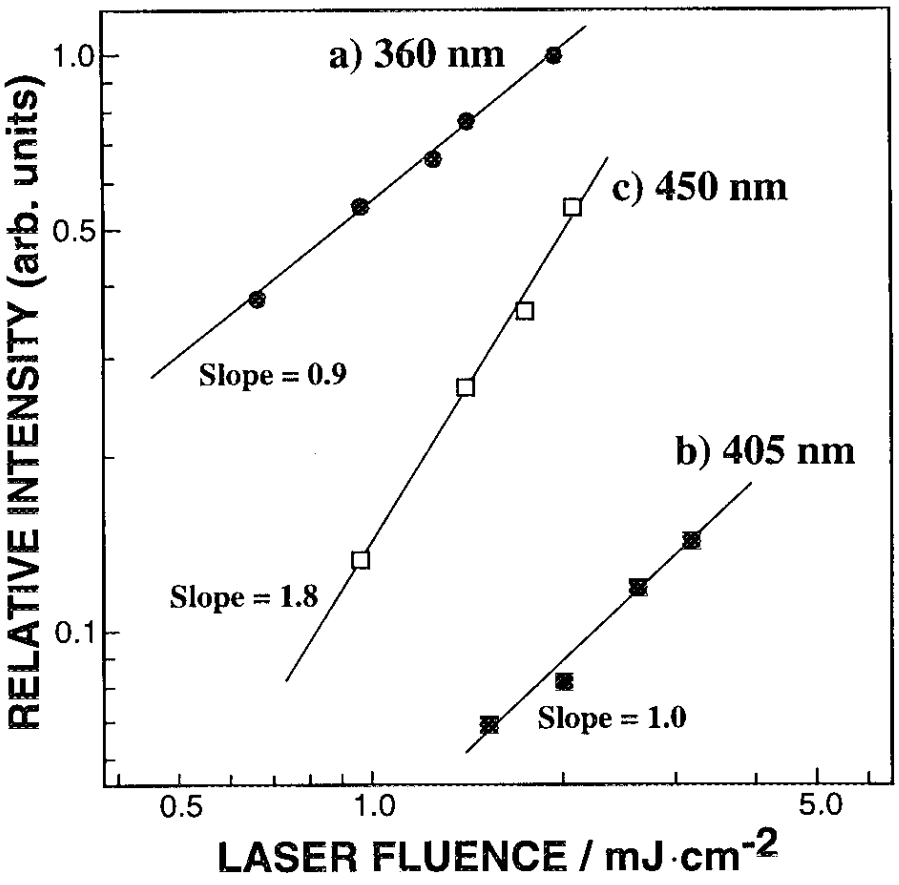

Figure V-5. Photolysis-laser-fluence dependencies of $CaOH^+$ fragment ion yields for the photodissociation of $Ca^+(H_2O)_n$. The data obtained at various wavelengths are shown by (●) at 360 nm (a), (■) at 405 nm (b), and (□) at 450 nm (c). The straight lines are the results of the least-squares fittings in the log-log plots. The slopes are 0.9 for (a), 1.0 for (b), and 1.8 for (c), respectively.

n=2 Photodissociation In the photodissociation of $Ca^+(H_2O)_2$, two evaporation fragments, $Ca^+(H_2O)$ and Ca^+, and two reaction products, $CaOH^+(H_2O)$ and $CaOH^+$, were detected as shown in Figure V-6. Although the $CaOH^+(H_2O)$ formed with an H-atom loss process is the dominant product ion in the lower energy region, its branching ratio decreases with increasing photon energy. On the other hand, the branching ratio of $CaOH^+$ increases with increasing photon energy, and it becomes close to 100 % in the higher energy region. These results clearly indicate that the $CaOH^+(H_2O)$ is the precursor of the $CaOH^+$ ion. The results on the laser fluence dependence of the $CaOH^+$ formation show that this ion is produced by one photon process in the energy region of 16000-28000 cm^{-1}. Figure V-7 shows the total fractions of the reaction and evaporation processes, respectively. In contrast to the case of $Ca^+(H_2O)$, the reaction process is the major dissociation channel and its fraction exceeds more than 80 % in the whole energy regions examined. These results are similar to those for the $Mg^+(H_2O)_2$ photodissociation (see Sections IV-3 and IV-4).

Photodissociation for the larger clusters In the photodissociation for n=3 and 4, two kinds of ions having the mass separation of ca. 18 were detected as the fragment ions. With the present photodissociation method, it is difficult to assign firmly the masses of these ions without an internal reference signal. However, the results on the $Ca^+(H_2O)_n$ photodissociation for n=1 and 2 in addition to those for $Mg^+(H_2O)_n$ show that the reactive fraction increases with increasing cluster size, especially for $n \geq 3$. Thus I believe that the fragments observed are not the evaporation products, $Ca^+(H_2O)_m$, but the reaction products such as $CaOH^+(H_2O)_{m-1}$. As for n=3, the branching ratio is almost independent of the photolysis energy and the ratio is 9:1 [$CaOH^+(H_2O)$: $CaOH^+$] (see Figure V-8). The results for n=4 are

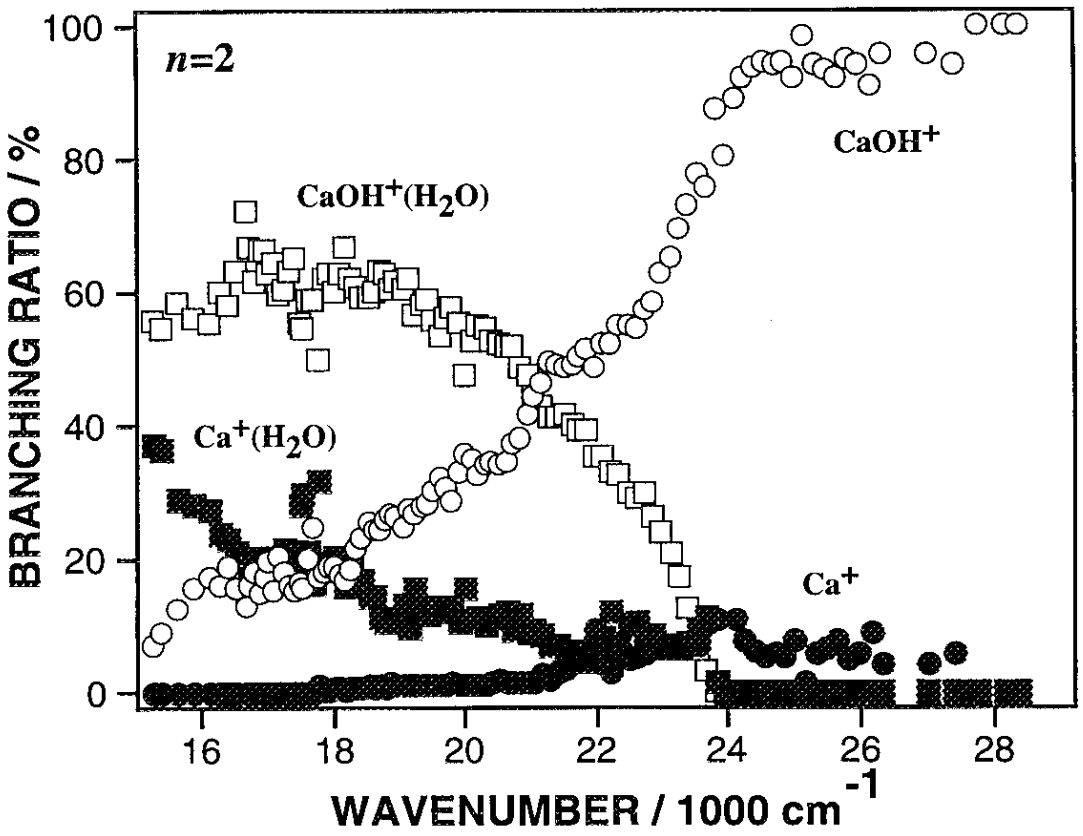

Figure V-6. Branching ratios of $Ca^+(H_2O)$ (■), Ca^+ (●), $CaOH^+(H_2O)$ (□), and $CaOH^+$ (○) produced by the photodissociation of $Ca^+(H_2O)_2$ plotted as a function of photon energy.

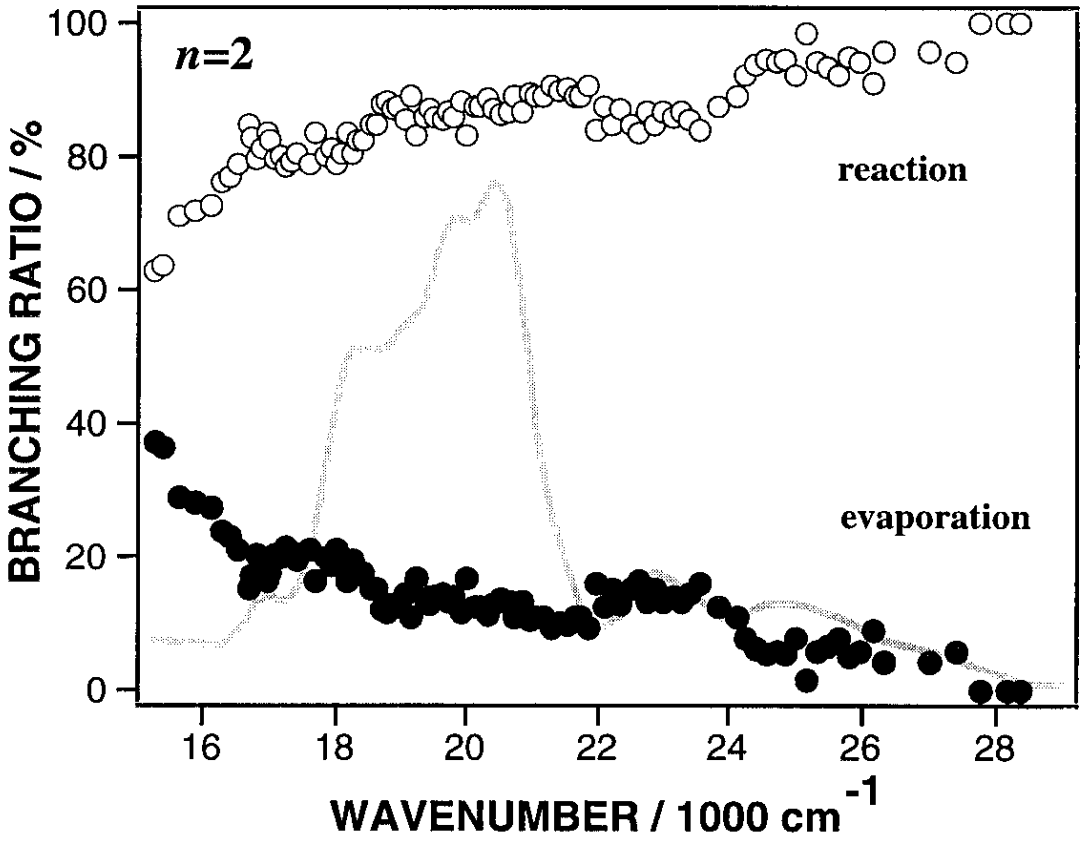

Figure V-7. The total branching ratios of the evaporation products, [$Ca^+(H_2O)$ and Ca^+], (●) and the reaction products, [$CaOH^+(H_2O)$ and $CaOH^+$], (○). The blurred curve in this figure represents the photodissociation spectrum of $Ca^+(H_2O)_2$.

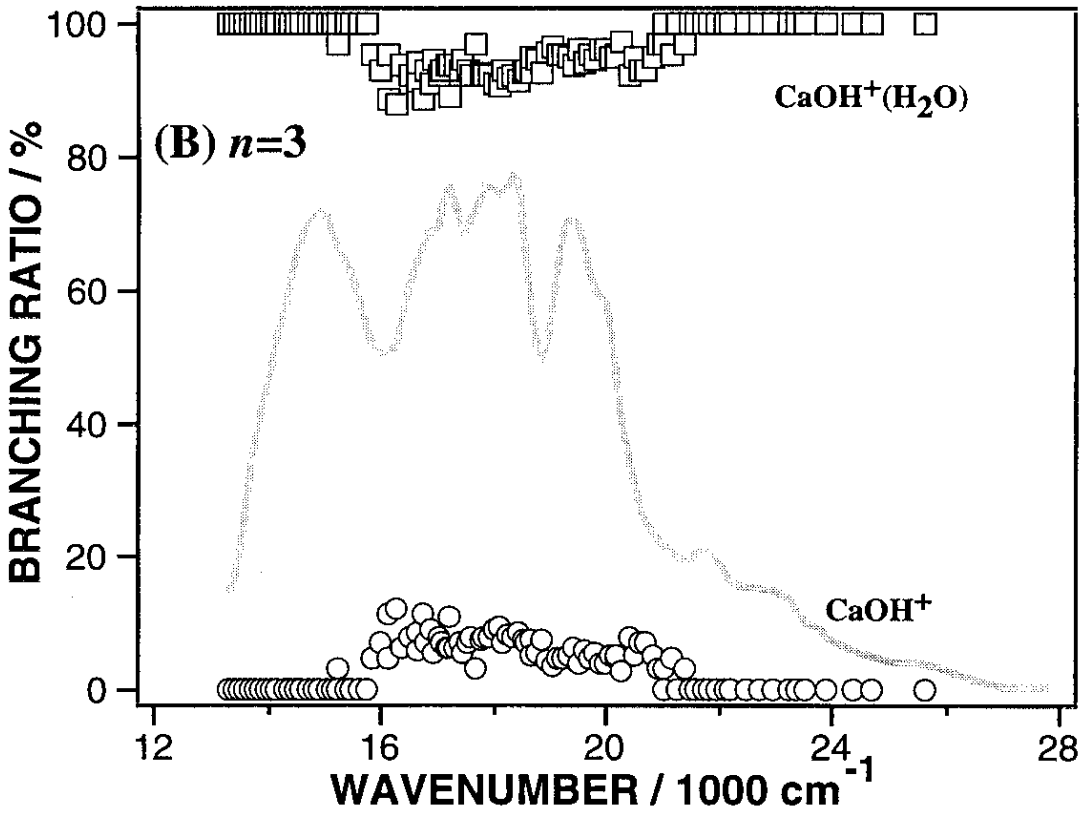

Figure V-8. Branching ratios of $CaOH^+(H_2O)$ (□) and $CaOH^+$ (○) produced by the photodissociation of $Ca^+(H_2O)_3$ plotted as a function of photon energy. Branching fractions of these ions are almost constant (9:1) in the avobe energy region. The blurred curve in this figure represents the photodissociation spectrum of $Ca^+(H_2O)_3$.

similar to those for n=3. For n=5 and 6, only one fragment ion such as $CaOH^+(H_2O)_{n-2}$ was detected: Since the excitation energy for these ions is substantially low, no further evaporation may occur.

V-4. Discussion

V-4.1. Electronic structure of $Ca^+(H_2O)_n$

Electronic structure of $Ca^+(H_2O)$ As shown in Figure V-3a, the photodissociation spectrum of $Ca^+(H_2O)$ consists of two distinct bands: a more intense band at 22400 cm^{-1} and a weaker band at 28000 cm^{-1}. Each bands are shifted with respect to the ^2P-^2S transition of Ca^+ (25303 cm^{-1}) by 2900 cm^{-1} to the red and by 2700 cm^{-1} to the blue, respectively, upon the complex formation. In analogy with the $Mg^+(H_2O)$, these absorption bands may be ascribed to the transitions from the ground state to the excited states derived from the ^2P level of Ca^+. The approximate intensity ratio of 2:1 observed for these bands supports the above assignments: the approach of $Ca^+(^2P)$ to H_2O generates the triple states corresponding to three different orientations of the singly occupied p-orbitals with respect to H_2O.

Bauschlicher and Partridge (BP) performed *ab initio* calculations of the $Ca^+(H_2O)_n$ ions for n=1 and 2 [28]. They predicted the binding energies and geometries for the ground-state ions, and the spectroscopic data including vertical excitation energies, transition intensities, and the characters of the low-lying electronic states. According to the BP's results, the optimized geometry of the ground-state $Ca^+(H_2O)$ is planar with C_{2v} symmetry as shown in Figure V-9a. The computed vertical transition energies are 21300 (2^2B_2, in-plane $p\pi$), 23100 (2^2B_1, out-of plane $p\pi$), and <29600 cm^{-1} (4^2A_1, $p\sigma$). The transition energies and relative intensities are plotted in Figure. V-

a) n=1, C_{2v}

b) n=2, D_{2h}

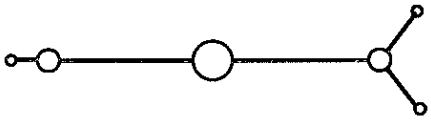

c) n=3, D_3

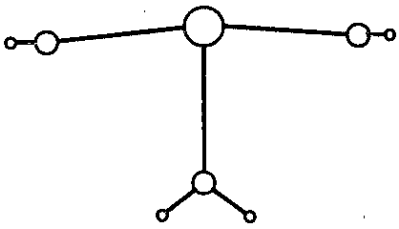

Figure V-9. Optimal structures for $Ca^{+}(H_2O)_n$, n=1 (a); n=2 (b); n=3 (c).These results were taken from Ref. 28.

3a. The calculated energies for three transitions are in good agreement with the observed peak positions. In the case of Mg^+, the ^2D level lies above ca. 35800 cm^{-1} from the ^2P level and the mixing of these two levels is negligible. However, the ^2D level of Ca^+ atomic ion lies below 11600 cm^{-1} from the ^2P level, and the electronic structure of the excited states is expected to be altered significantly by the ^2P-^2D mixing. In order to characterize the nature of these excited states, BP made a population analysis and predicted the 4*s*, 4*p*, and 4*d* populations in the excited states for the $Ca^+(H_2O)$ ion. According to their results, main characters of these transitions are the ^2P-^2S excitation localized on Ca^+, however, the excited states related to these transitions have a significant amount of the 3*d* character as well due to the ligand-field-induced *d*-*p* mixing. The ratio of the absorption intensities for the three transitions is calculated to be 4.63($^2B_2$):3.47($^2B_1$):1.47($^2A_1$). However, the predicted ratio is far from the observed ratio, 2($^2B_2$ and $^2B_1$):1($^2A_1$). They also predicted three ^2D-^2S type transitions having a substantially large transition moment just below the above transitions; 3^2A_1-1^2A_1(17000 cm^{-1}), 1^2B_2-$^2A_1$ (15500 cm^{-1}), and 1^2B_1-$^2A_1$(16800 cm^{-1}), respectively. In contradiction to these expectations, no absorption was observed in the lower energy region as shown in Figure V-3a. These results seem to imply that their calculations overestimated the *p*-*d* mixing. Therefore, the observed bands can be ascribed to the transitions to the ^2P-type excited states having much smaller 4*d* population than the theoretical predictions. The fact, that the absorption spectrum of $Ca^+(H_2O)$ is almost the same as that for $Mg^+(H_2O)$ except for the excitation energy, seems to support these arguments.

Electronic structure of $Ca^+(H_2O)_2$ Figure V-3b shows the photodissociation spectrum of $Ca^+(H_2O)_2$. The spectrum consists of an intense band (20000 cm^{-1}) and a week broad band (24700 cm^{-1}). BP also

calculated the geometry, the vertical excitation energies, and the transition intensities for $Ca^+(H_2O)_2$ [28]. The optimal structure has D_{2h} symmetry; that is, the waters are eclipsed as shown in Figure V-9b. The computed transition energies are in good agreement with the experiment results as shown in Figure V-3b: The calculated results are 19100 cm^{-1}[$1^2E(4p\pi^1)$ and $2^2E(4d\pi^1)$] and <25200 cm^{-1}[$2^2B_2(4p\sigma^1)$]. Therefore, the observed bands can be assigned to the ^2P-^2S type transitions localized on the Ca^+ ion, and are red-shifted with respect to the Ca^+ atomic ion transition by 5300, and 600 cm^{-1}, respectively. The redshifts for $Ca^+(H_2O)_2$ are larger than those for $Ca^+(H_2O)$. The shift with the second water is probably due to a shift up in energy of the ground state due to a destabilization of the 4*s* orbital when ligands are on both sides of the Ca^+ ion. The intensity ratio for the 20000-cm^{-1} and 24700-cm^{-1} bands is found to be smaller than the calculated result: the observed ratio is ca. 4:1, while the calculated ratio of the 1^2E-1^2A_1 and 2^2B_2-1^2A_1 transitions is 9.08:3.52. The spectrum of $Sr^+(NH_3)_2$ reported by Shen and Farrar also shows the similar feature to that for $Ca^+(H_2O)_2$: an intensity reduction was observed for the transition to the higher excited state derived from the $^2P(4p\sigma^1)$ state of Sr^+ [21]. They proposed a possible reason for this reduction in intensity as follows: The ground state retains *s*-orbital character, and to the extent that the cluster transitions can be considered as metal-centered transitions, the increasing admixture of *d* character in the excited state makes the transition increasingly forbidden. Although this effect is expected to be small, the intensity reduction observed in the spectrum is consistent with this orbital mixing interpretation.

Electronic structures for larger clusters The photodissociation spectra for $n \geq 3$ are shown in Figures V-3c - V-3f. Though the theoretical data are not available for the $Ca^+(H_2O)_n$ ($n \geq 3$), the observed bands may also be

assigned to the ^2P-^2S transitions localized mainly on the Ca^+ ion. The absorption spectra for this entire series of clusters show significant redshifting as large as 18000 cm^{-1} relative to the atomic lines of Ca^+ and a very clear evolution from the visible to the near IR. Although the photodissociation spectra of $Mg^+(H_2O)_n$ are also found to exhibit large redshifts and show clear evolution of the solvation shell closing at n=3, these spectral changes are mostly due to metal-ligand repulsion rising the ground-state energy. In contrast to $Mg^+(H_2O)_n$, the absorption bands for $Ca^+(H_2O)_n$ redshift monotonically with increasing cluster size for n up to 6. According to the theoretical calculations by BP [28], the Ca^+ ion undergoes $sd\sigma$ hybridization compared with the sp hybridization for Mg^+. If this is the case, the first shell surrounding the Ca^+ ion is expected to be filled with 6 water molecules. Recently, Kochanski and Constantin calculated the structures of $Ca^+(H_2O)_n$ for n up to 10 using a Monte Carlo method and found that the most stable structures have five or six water molecules in the first shell [7]. These theoretical predictions seems to be consistent with the observed spectra. As discussed in Chapter IV, the interaction of the Mg^+ ion with the second-shell water molecule is much weaker than that for the first solvent shell. Thus the monotonous redshifts observed for $Ca^+(H_2O)_n$ may indicate that the first solvent shell surrounding Ca^+ is not yet filled for n=3-5: The tendency in the spectral shifts seem to exhibit the shell closing with six water molecules. It should be note that the spectral shapes for these clusters become much sharper with increasing the number of water molecules. This may be due to the increase in a symmetry of the ligand field as it is seen for $Mg^+(H_2O)_3$; Oh for n=6.

As mentioned in Chapter IV, Donnelly and Farrar proposed another possibility to interpret the redshifts for $Sr^+(NH_3)_n$ [21]. They carried out a spectral moment analysis of the cross sections and found a large increase in

the electronic radial distribution in the ground state with increasing cluster size. On the basis of these results, they suggested an increasing Rydberg character of cluster states that correlate with 5*s* and 5*p* atomic orbitals on Sr^+; ion-pair character in the ground and excited state wave functions of the metal increases with increasing cluster size. As in the case of Sr^+, the ionization potential of $Ca^+(^2P)$ is rather low (11.87 eV) [27] and a Rydberg-type ion-pair state, $Ca^{2+}(H_2O)_n^-$, may mix into the wave functions for the 5*s*- and 5*p*-based valence states. Therefore, both the destabilization of the ground state due to metal-ligand interaction and the mixing of the Rydberg-type ion-pair state are considered to be the plausible mechanism for the origin of the observed large redshifting.

V-4.2. Photodissociation processes of $Ca^+(H_2O)_n$

As in the case of $Mg^+(H_2O)_n$, both the evaporation of water molecules and the photoinduced intracluster reaction with an H-atom elimination were observed in the photodissociation of $Ca^+(H_2O)_n$. However, the size dependence of the reaction for $Ca^+(H_2O)_n$ was found to be different from that for $Mg^+(H_2O)_n$. In the following paragraphs, the two processes are separately discussed to make the discussion clear.

Evaporation processes The photoexcitation of $Ca^+(H_2O)_n$ induces the evaporation of water molecules as well as the intracluster reaction as seen in Figure V-4. The former process is found to be the efficient deexcitation process especially for the small clusters. In order to understand the mechanism of the evaporation process, information on the excited-state potential surfaces is indispensable. However, at present, no experimental and theoretical data are available for the excited-state surfaces of these clusters. And also, the observed absorption spectra for these clusters have low

resolution due to insufficient cooling of the parent ions, and as a result, they provide us no detail information on the excited state surface. However, recently, Kochanski and Constantin have reported the experimental and theoretical studies on the structures and the successive binding energies for $Ca^+(H_2O)_n$ [7]. They determined the successive hydration energies for n up to 5 using a high pressure mass spectrometry. According to their results, the binding energy for Ca^+-H_2O is 28 kcal/mole (1.21 eV). This number is a little bit higher than that calculated by Bauschlicher, *et al.* using an *ab initio* method (26.6 kcal/mol) [28]. Using the experimental binding energy for the ground-state $Ca^+(H_2O)$, the author obtained the dissociation limit of the excited state, $Ca^+(^2P)(H_2O) \rightarrow Ca^+(^2P) + H_2O$, as ca. 35000 cm^{-1} (4.34 eV), where as the ^2P-^2S level spacing is 25200 cm^{-1} (3.13 eV). This result as well as the absorption spectrum for n=1 clearly shows that the three excited states (2^2B_2, 2^2B_1, and 4^2A_1) derived from the ^2P state of Ca^+ are all bound along the Ca^+-H_2O stretching coordinate. Therefore, as in the case of $Mg^+(H_2O)$, the dissociation dynamics is predissociative in character.

As seen in Figure V-4, the evaporation process to produce Ca^+ is predominant at least in the first and second excited states (2^2B_2 and 2^2B_1, respectively) for the $Ca^+(H_2O)$ ion. These results are in marked contrast to those for $Mg^+(H_2O)$; as seen in Figure IV-8, the evaporation process for the latter ion is the minor process (less than 10 %) and its branching ratio is almost constant for the photolysis energy. The reason why these two ions exhibit the different evaporation behaviors may be ascribed to the difference in the excited-states electronic structures for these ions. As mentioned previously, the ^2D state of Ca^+ lies below the ^2P state, while that for Mg^+ lies far above the ^2P state. As a result, the excited states of $Ca^+(H_2O)$ derived from Ca^+ ^2D may deeply involve in the evaporation process for this ion. According to the theoretical calculations by Bauschlicher and his co-workers

[28], the $1^2B_2(^2D, d\pi)$ and $1^2B_1(^2D, d\pi')$ states lie only ca. 4000 cm^{-1} and ca. 7000 cm^{-1}, respectively, below the states derived from the ^2P state. Since these excited states have the same symmetries as those for the ^2D-type excited states, the couplings between these states are electronically allowed. Moreover, the energy separations between these states are small, and as a result, a part of the potential wells of these states may overlap each other. These situations may cause a strong coupling between these states and the internal conversion to the ^2D-type states is expected to be strongly enhanced. The direct internal conversion to the ground state as in the case of $Mg^+(H_2O)$ may also play some roles, however, the deexcitation process via the ^2D-type state may be the predominant channel for the evaporation of water molecules. As for n=2 and larger clusters, the branching ratios for the evaporation processes become much smaller than that for n=1 as seen in Figure V-7. The mechanism of this process is expected to be the same.

It is worth to note that the branching ratio curve of the Ca^+ ion shows a threshold behavior having the onset energy of 2.2 eV (18000 cm^{-1}) as shown in Figure V-6. This threshold energy corresponds to the lowest energy to produce Ca^+ from $Ca^+(H_2O)_2$. The result also indicates that a sequential evaporation occurs for larger clusters.

Intracluster reaction for $Ca^+(H_2O)_n$ The photoinduced dehydrogenation to produce $CaOH^+(H_2O)_{n-1}$ was found to occur efficiently in the $Ca^+(H_2O)_n$ photodissociation as in the case of $Mg^+(H_2O)_n$. These reactions depend strongly on the excitation energy and cluster size. However, the feature of the reaction for the Ca^+-H_2O system is quite different from that for Mg^+. In this section, the energetics and mechanisms of the intracluster reactions for these clusters are discussed on the basis of the results for the branching ratios.

It is informative to consider first the energetics of the Ca^+-H_2O system. The experimental hydration energies (ΔE) of $Ca^+(H_2O)_n$ were reported to be $\Delta E_{1,0}$=28 and $\Delta E_{2,1}$=24 kcal/mol [7]. These numbers are in good agreement with the computed binding energies ($\Delta E_{1,0}$=26.6 and $\Delta E_{2,1}$=22.6 kcal/mol) [28]. On the basis of these results, we can draw the level structure for the energies of Ca^+-H_2O system as shown in Figure V-10. The energy needed for the H-atom elimination from $Ca^+(H_2O)$ is obtained to be ca. 40 kcal/mol (14400 cm^{-1}), while the threshold energy for the formation of $CaOH^+$ from n=2 is estimated to be 66 kcal/mol from this energy diagram.

As seen in Figure V-4, the branching ratio of the $CaOH^+$ production for the $Ca^+(H_2O)$ photodissociation exhibits the threshold behavior with the onset energy of ca. 23000 cm^{-1} (66 kcal/mol): The ion signals observed in the energy below this threshold are formed by the two-photon process, in which $CaOH^+$ is produced through the higher ^2D-type excited states populated by sequential two-photon absorption as mentioned previously. These results for n=1 are in marked contrast to those for $Mg^+(H_2O)$; as for the latter ion, the reaction is the predominant process and depends not on the photolysis energy. Since the onset energy is much larger than the reaction endothermicity for the $CaOH^+$ production from $Ca^+(H_2O)$ (14000 cm^{-1} in Figure V-10), the observed threshold behavior cannot be ascribed to the energy limit of the $CaOH^+$ production. The other origin may be the opening of a new reaction channel in the energy above 23000 cm^{-1}. As for this origin, the author can also consider a possible contribution of the low-lying ^2D-type excited states. These states are predicted to lie 4000-7000 cm^{-1} below the lowest excited state (2^2B_2) derived from the ^2P state of Ca^+ [28], and play an important role in the enhancement of the evaporation process as mentioned previously. However, it is difficult to consider the preferential interaction of these states to cause the threshold behavior of reaction in the relevant energy region. Besides these

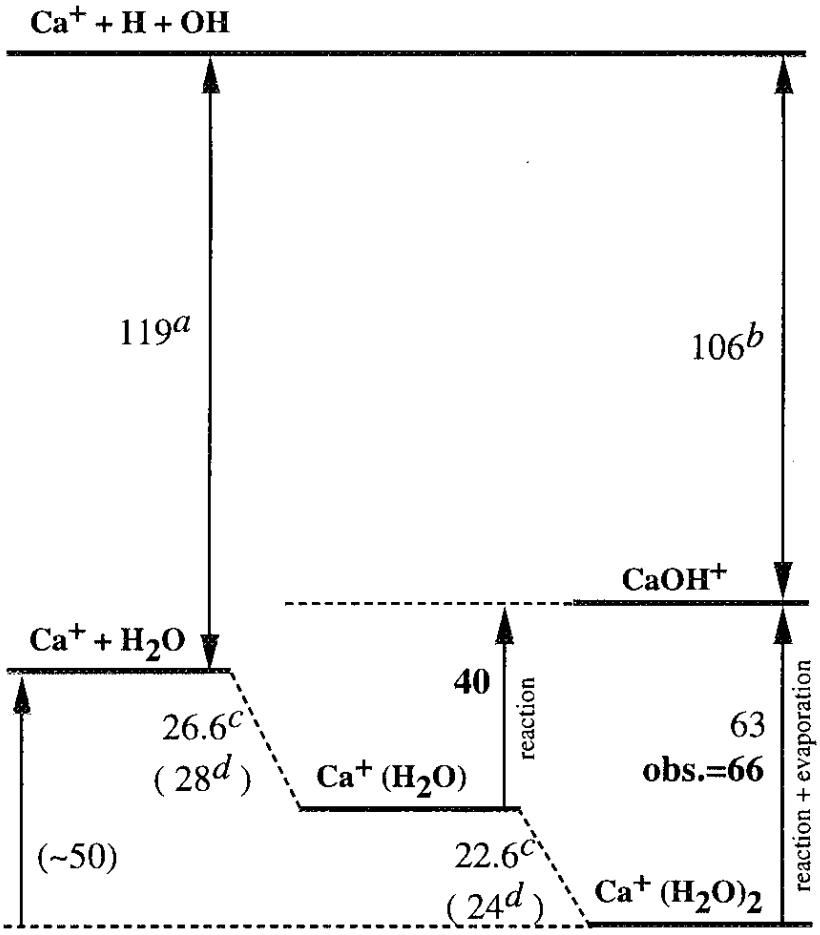

Figure V-10. Relative energies for the $Ca^+(H_2O)_{1,2}$ system. These energies in the diagram are given in kcal/mol. [a]Ref. 29, [b]Ref. 8, [c]Ref. 28, and [d]Ref. 7 are cited for determine the binding energies.

origins, I have to take into account the excited-state reaction. Relating to this issue, the state-specific reaction was found for $Mg^+(H_2O)_2$ as mentioned in Chapter IV. More recently, Duncan and his co-workers also found the excited-state reaction channel for the photodissociation of Mg^+-CO_2 complex [17]: They found the direct reaction channel to produce the MgO^+ ions from the 2^2S state. As for $Ca^+(H_2O)$, the onset of the absorption band assigned to the $2^2A_1(p\sigma)$-1^2A_1 transition agrees with the threshold of the reactive fraction within an experimental error as it is seen in Figure V-4. This fact may strongly support that an excited-state reaction channel to produce $CaOH^+$ opens in the energy region above 23000 cm^{-1}.

In the case of $Ca^+(H_2O)$, the reaction is energetically possible from three excited states, $p\pi(^2B_2$ and $^2B_1)$ and $p\sigma(^2A_1)$ as seen in Figure V-11, thus the selectivity for reaction of the $p\sigma$ state may arise from the different alignment of the excited p orbital. The lowest unoccupied molecular orbital of H_2O is the $4a1^*$, which is strongly antibonding. Population in $4a1^*$ orbital causes the binding of H_2O to be weaker. It seems possible that the metal insertion reaction, $Ca^+(H_2O) \rightarrow$ H-Ca^+-OH, could be promoted by donation of electron density into this orbital, which would result in a complex with Ca^{2+}-H_2O^- bonding character. In the excited $^2A_1$ $(p\sigma)$ state, which undergoes the metal oxidation reaction, the p orbital and its corresponding electron density are inserted into close special proximity with the H_2O orbitals. The symmetry of approach alone indicates that there would be good overlap between the $p\sigma$ and the $4a1^*$ orbitals. On the other hand, the $^2B_2($ and $^2B_1$ states does not react, have the $p\pi$ orbitals on Ca^+ lined up perpendicularly to the lobes of the antibonding H_2O orbital with incorrect symmetry. In relation to this issue, Duncan and his co-workers argued about the possible mechanism including a charge transfer from CO_2 to Mg^+. As in the case of Mg^+-CO_2, the similar charge transfer mechanism may play some roles in the reaction of $Ca^+(H_2O)$.

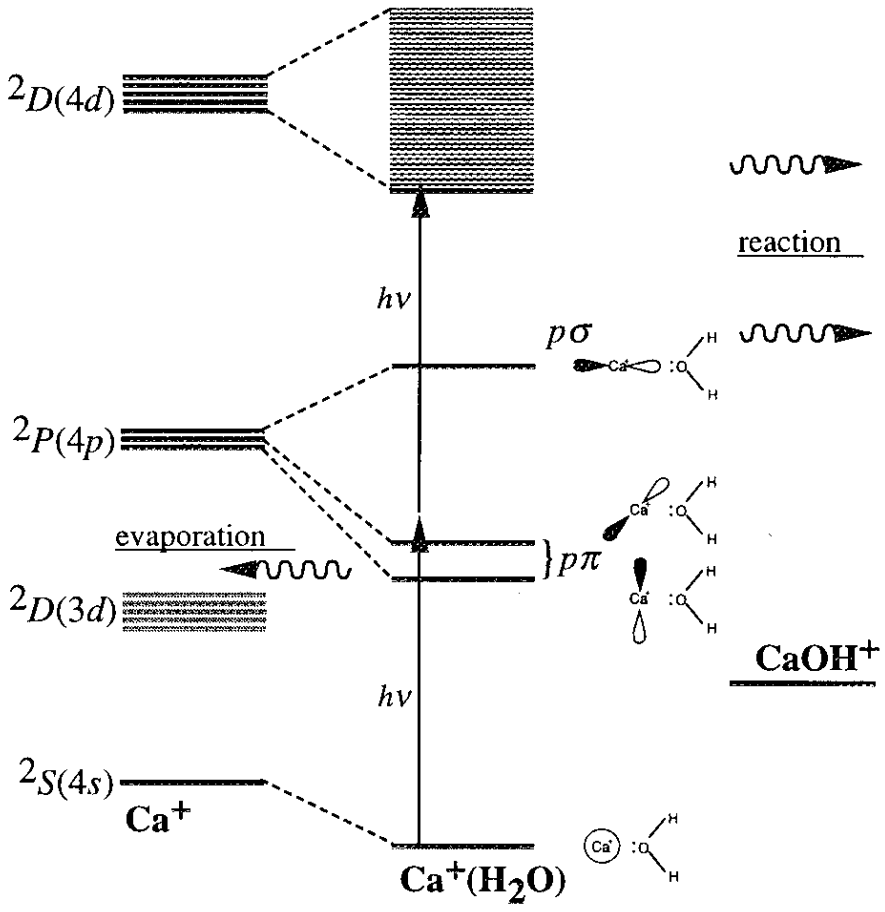

Figure V-11. Schematic energy level diagram of $Ca^+(H_2O)$.

In the $Ca^+(H_2O)_2$ photodissociation, four kinds of fragment ions such as Ca^+ and $Ca^+(H_2O)$, and $CaOH^+(H_2O)$ and $CaOH^+$ are formed. Interestingly, the reaction to produce the latter ions is the predominant process in the whole energy region examined as shown in Figure V-6 and V-7. This trend is much evident in the n=3 photodissociation, where no evaporation product was detected as shown in Figure V-8. Since the rate of evaporation for these clusters, which may be induced by the internal conversion through mixing with the low-lying ^2D-type states as discussed previously, is expected to be similar to that for n=1, the above results may indicate that the reaction process is enhanced dramatically with increasing the number of water molecules and it surmounts the evaporation process. These drastical changes in reactivity for larger clusters remind us of the possible contribution of the electron donation mechanism involving the mixing of the $Ca^{2+}(H_2O)^-$ character. However, it may be premature to further discuss the mechanism of reaction for n=2 and larger clusters. In order to clarify the dynamics of intracluster reaction, it seems to be necessary to carry out a real-time measurement of the excited-state decay rate as well as the theoretical calculations of the reactive potential surfaces.

V-5. Conclusion

An extensive spectroscopic study of the calcium-water system has been presented in this chapter. The photodissociation spectra of $Ca^+(H_2O)_n$, n=1-6, have been measured in the wavelength region from 335 to 1440 nm. The absorption spectra for this entire series of cluster exhibit large redshifts as large as ~18000 cm^{-1} with respect to the ^2P-^2S resonance line of the free Ca^+ ion and are explained by the shift of this transition as a result of hydration. In contrast to $Mg^+(H_2O)_n$, the absorption bands redshift monotonically with increasing cluster size for n up to 6. This discrepancy is attributed to the difference in the number of solvent molecules filling the first solvation shell, because of the $sd\sigma$ hybridization for the latter ion: The first shell of $Ca^+(H_2O)_n$ may be filled at n~6. As in the Mg^+-H_2O system, the dehydrogenation reactions to produce the hydrated $CaOH^+$ ions are also observed for the Ca^+-H_2O system. However, the size-dependence and state selectivity of the reaction for $Ca^+(H_2O)_n$ are found to be different from those for $Mg^+(H_2O)_n$. These discrepancies are ascribed to the difference in the electronic and geometric structures of these clusters: In the case of Ca^+, the ^2D state lies between the electronic ground ^2S state and the ^2P states.

References for Chapter V

[1] P. Kebarle, *Ann. Rev. Phys. Chem.* **28**, 445 (1977).

[2] T. D. Mark and A. W. Castleman, Jr., *Adv. Rev. Mol. Phys.* **20**, 65 (1986).

[3] P. B. Armentrout, *Ann. Rev. Phys. Chem.* **41**, 313 (1990).

[4] E. J. Bieske and J. P. Maier, *Chem. Rev.* **93**, 2603 (1993).

[5] I. Dzidic, P. J. Kebarle, *J. Phys. Chem.* **74**, 1466 (1970).

[6] R. G. Keesee and A. W. Castleman, Jr., *J. Phys. Chem. Ref. Data.* **15**, 1011 (1986).

[7] E. Kochanski and E. Constantin, *J. Chem. Phys.* **87**, 1661 (1987).

[8] T. F. Magnera, D. E. David, and J. Michl, *J. Am. Chem. Soc.* **111**, 4100 (1989).

[9] T. F. Magnera, D. E. David, D. Stulik, R. G. Orth, H. T. Jonkman, and J. Michl, *J. Am. Chem. Soc.* **111**, 5036 (1989).

[10] P. J. Marinelli, R. R. Squires, *J. Am. Chem. Soc.* **111**, 4101 (1989).

[11] L. Operti, E. C. Tews, and B. S. Freiser, *J. Am. Chem. Soc.* **110**, 3847 (1988).

[12] L. Operti, E. C. Tews, T. J. MacMahon, and B. S. Freiser, *J. Am. Chem. Soc.* **110**, 9125 (1989).

[13] D. E. Lessen, R. L. Asher, and P. J. Brucat, *J. Chem. Phys.* **93**, 6102 (1990).

[14] D. E. Lessen, R. L. Asher, and P. J. Brucat, *J. Chem. Phys.* **95**, 1414 (1991).

[15] C. S. Yeh, K. F. Willey, D. L. Robbins, J. P. Pilgrim and M. A. Duncan, *Chem. Phys. Lett.* **196**, 233 (1992).

[16] K. F. Willey, C. S. Yeh, D. L. Robbins, J. P. Pilgrim and M. A. Duncan, *J. Chem. Phys.* **97**, 8886 (1992).

[17] C. S. Yeh, K. F. Willey, D. L. Robbins, and M. A. Duncan, *J. Phys. Chem.* **96**, 7833 (1992).

[18] L. N. Ding, M. A. Young, P. D. Kleiber, W. C. Stwalley, and A. M. Lyyra, *J. Phys. Chem.* **97**, 2181 (1993).

[19] M. H. Shen and J. M. Farrar, *J. Phys. Chem.* **93**, 4386 (1989).

[20] M. H. Shen and J. M. Farrar, *J. Chem. Phys.* **94**, 3322 (1991).

[21] S. G. Donnelly and J. M. Farrar, *J. Chem. Phys.* **98**, 5450 (1993).

[22] M. H. Shen, J. W. Winniczek, and J. M. Farrar, *J. Phys. Chem.* **91**, 6447 (1987).

[23] F. Misaizu, M. Sanekata, K. Tsukamoto, K. Fuke, and S. Iwata, *J. Phys. Chem.* **96**, 8259 (1992).

[24] K. Fuke, F. Misaizu, M. Sanekata, K. Tsukamoto, and S. Iwata, *Z. Phys.* D**26**, S180 (1993).

[25] F. Misaizu, M. Sanekata, K. Fuke, and S. Iwata, *J. Chem. Phys.* **100**, 1161 (1994).

[26] M. Sanekata, F. Misaizu, and K. Fuke, *J. Am. Chem. Soc.*, in press.

[27] *Atomic Energy levels*; edited by C. E. Moore, Natl. Stand. Ref. Data Ser., NBS 35, Vol. **1** (National Bureau of Standards, Washington, DC, 1971).

[28] C. W. Bauschlicher, Jr., M. Sodupe, and H. Partridge, *J. Chem. Phys.* **96**, 4453 (1992).

[29] S. G. Lias, J. E. Bartmess, J. F. Liebman, J. L. Holmes, R. D. Levin, and W. G. Mallard, *J. Phys. Chem. Ref. Data Suppl.* **17** (1988).

Chapter VI

Reaction of singly charged metal ions with water clusters

VI-1. Introduction

The clusters containing metal ions have been studied extensively for more than twenty years in order to bridge the gap between the gas phase and condensed phase. These studies are mostly concerned with the determination of the successive solvation energies by high pressure mass spectrometry [1,2] and collision induced dissociation experiments [3]. On the other hand, the spectroscopic studies on the clusters composed of metal atom or its ion solvated with polar molecules have been developed rapidly in recent years. Hertel's and the author and his group have examined the photoionization process of the solvent clusters containing neutral alkali atoms such as Na [4] and Cs [5]. Both groups have found that the ionization potential (IP) of the clusters with water molecules saturates for $n \geq 4$ and its limiting values ($n \rightarrow \infty$) coincide with the estimated IP of an excess electron solvated in bulk water. Landman and his co-workers have examined the IPs for $Na(H_2O)_n$ theoretically to understand these anomalous observations and ascribed these behaviors to an evolution of a Rydberg-like ion-pair state with increasing cluster size [6]. Hashimoto *et al.* have also calculated the same system using the *ab initio* method and proposed an alternate mechanism for the IP saturation [7]. As for the clusters containing metal ions, Farrar's and the author have studied the photodissociation spectra of size-selected clusters, $Sr^+(NH_3)_n$ [8] and $Mg^+(H_2O)_n$ [9], in which the metal ions have an isoelectronic structure with alkali metal atoms. The spectra of the $Sr^+(NH_3)_n$ ions exhibit monotonous redshifts with respect to the Sr^+ resonance lines

spanning from the visible to near IR with increasing cluster size [8c], while the latter ions show relatively small redshifts exhibiting the clear evolution of the solvation shells [9c]. The redshifts for the former ions were ascribed to the same mechanism as those for the alkali metal-water systems. However, the theoretical study predicted a different mechanism such as a destabilization of the electronic ground state due to metal-ligand interactions [10b].

The energy dissipation and reactivity of these cluster ions are also important to get an insight into the dynamics of microscopic solvation. I found that the photoexcitation of $M^+(H_2O)_n$ (M=Mg and Ca) induces an H-atom elimination reaction with producing $MOH^+(H_2O)_m$; this process corresponds to an intracluster redox reaction [9c]. Farrar and his co-workers have examined the energy dissipation and evaporation processes of $Sr^+(NH_3)_n$ using a picosecond pump-probe photodissociation technique [11]. The other interesting aspect of the metal ion-solvent cluster (S_n) systems is a collision induced reaction, $M^+ + S_n$. The study on the cluster reaction includes an experimental difficulty in specifying the size of the neutral solvent clusters, however, the results for the photodissociation experiments mentioned above may provide us some guidelines to understand these complex reactions; the $M^+(H_2O)_n$ photodissociation corresponds to a half collision process of the $M^+ + (H_2O)_n$ reactions. Despite of the experimental limitation, the study on these reactions is still quite informative to get an insight not only into the dynamics of metal-ion solvation, but also into the chemistry in the upper atmosphere [12] in which the similar reaction processes including the singly charged alkaline-earth metal ions have found to be involved.

In the earlier stage of these studies, the author found an anomalous product distributions for the $Mg^+ + (H_2O)_n$ reactions occurred in a pickup-type cluster source. Both the $Mg^+(H_2O)_n$ and $MgOH^+(H_2O)_{n-1}$ ions are produced with characteristic size distribution; for Mg^+, the former ions are

dominant for $n \leq 5$ and $n \geq 15$, while the latter ions are produced exclusively for $6 \leq n \leq 14$. In order to understand these features for the product distributions, the photodissociation spectra and dissociation processes of $Mg^+(H_2O)_n$ n=1-5 were examined in Chapter IV [9]. In this chapter, the author studies the reactions of the Ca^+ ions with water clusters in the pickup cluster source as well as those for Mg^+, and a deuterium substitution effect on these reactions. The product distributions of the Mg^+ reaction with water molecules are also examined as a function of the initial kinetic energy (KE) of metal ions using a simple crossed beam source. Moreover, the author reexamine the photodissociation processes of mass selected $Mg^+(H_2O)_n$ ions, especially focus on the photoinduced reaction. On the basis of the results on the intracluster reactions, the reaction mechanism and the origins of the product switching for the metal ion-water cluster reactions will be fully discussed in this chapter.

VI-2. Experimental

The apparatus used is described in Chapter II. Therefore, only a brief description of the features relevant to the this study is given here. The apparatus consists of a cluster source and a reflectron time-of-flight (TOF) mass spectrometer. The cluster ions containing alkaline-earth metal ions (Mg^+ and Ca^+) are formed by a pickup type cluster source; metal ions are produced by laser irradiation of a rotating metal rod (ø5 mm) which is placed about 10 mm downstream from a pulsed valve (General valve, series 9). Second harmonic of a Nd:YAG laser (Spectra Physics, GCR-12S) is used as the vaporization laser. The ions are picked up by water clusters formed by expansion of water vapor seeded in He gas from the valve. Typical pressures

of H_2O vapor and He are 20 Torr (vapor pressure at room temperature) and 4 atm, respectively. Resultant cluster ions are collimated with a 2.5 mm-diameter skimmer and then accelerated colinearly with the incident cluster ion beam by pulsed electric fields in the acceleration grids of the Wiley-McLaren type TOF mass spectrometer. Accelerated ions are reflected by double-stage electric fields at the end of the flight tube after flying 1.4 m in the field free region. Reflected ions are detected by dual multichannel plates. Ion signals are stored in a digital storage oscilloscope (LeCroy 9450).

Besides the cluster source noted above, a simple cross beam assembly is also adopted to investigate the effect of the kinetic energy (KE) on the product distributions for the metal ion-water cluster reaction. In this experiment, the metal ion source is placed at 200 mm from the water cluster beam. The metal ions produced by the laser vaporization are guided by ion optics and are perpendicularly injected into the water cluster beam at 15 mm downstream from a pulse nozzle. The initial KE distribution of the metal ions is measured by a channeltron placed at 270 mm downstream from the ion source (see Figure VI-1). Figure VI-2 shows the KE distribution of the Mg^+ ion obtained at the laser fluence of about 20 mJ/pulse. The KE of ions is determined from time duration between the irradiation of the vaporization laser and the ion detection. The center of mass KE is scanned by varying the triggering the time of the vaporization laser with a fixed timings of the pulsed nozzle opening and the pulsed extraction fields. In this scheme, the energy resolution is limited by the distance between the pulsed extraction plates (20 mm), and is estimated to be ±5 eV. The mass spectrum of the product ions are measured by using the same apparatus as mentioned above.

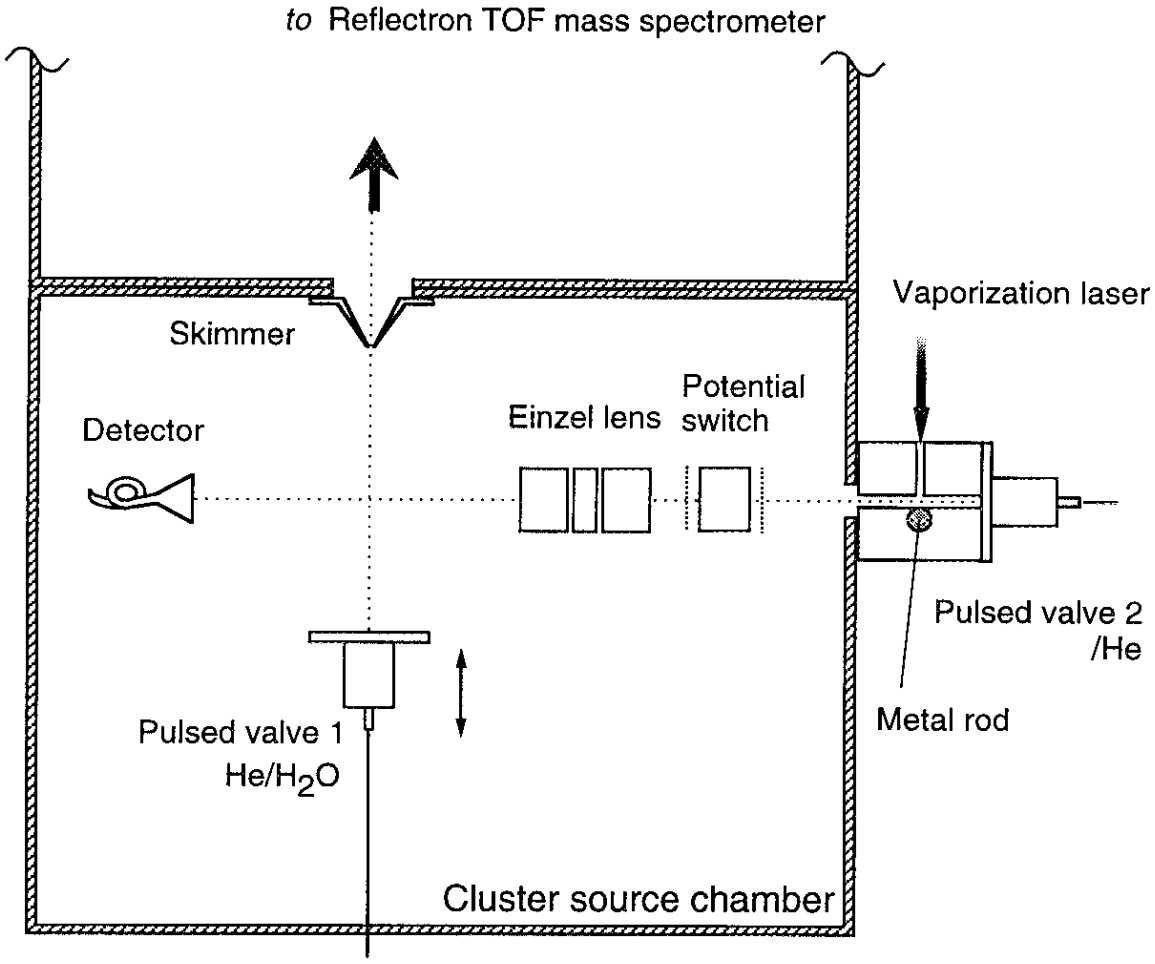

Figure VI-1. The schematic drawing of the cluster ion source for the simple cross beam assembly. The metal ions produced by the laser vaporization and guided by ion optics are perpendicularly injected into the water cluster beam, which is produced by supersonic expansion from the pulsed valve 1.

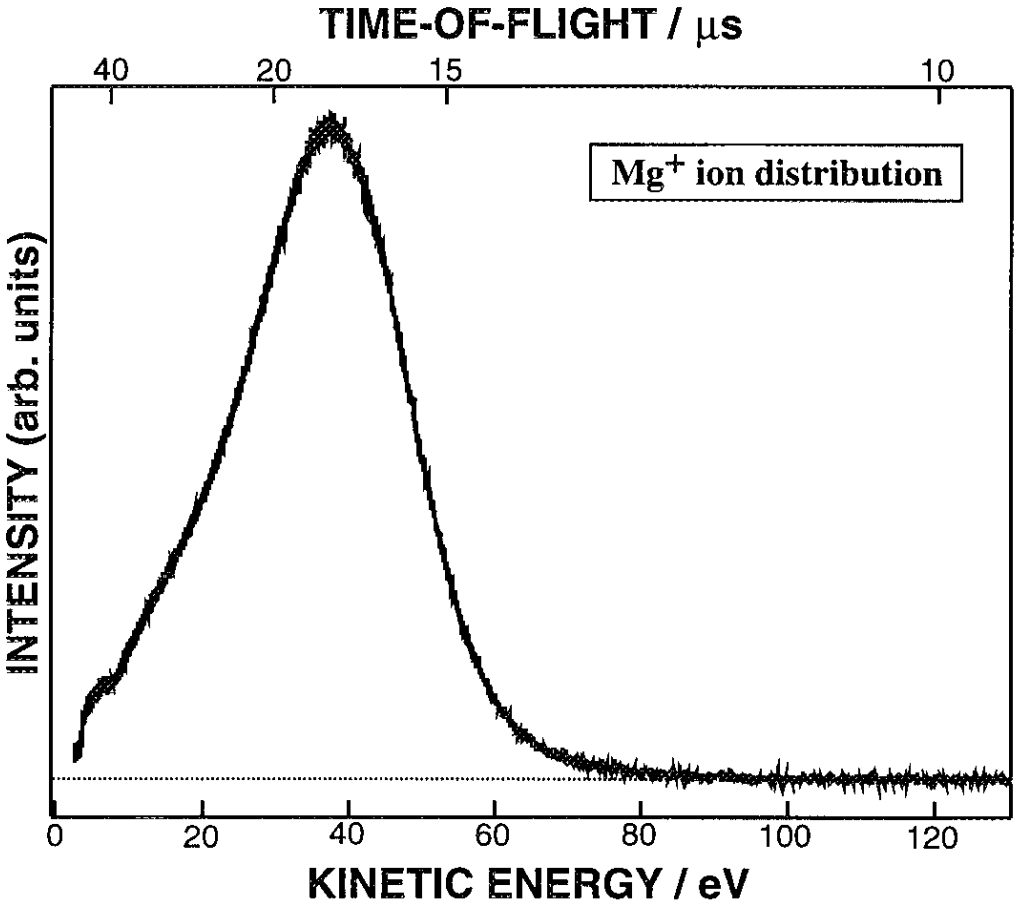

Figure VI-2. Kinetic energy (KE) distribution of the Mg^+ ions produced by the second harmonic of a Nd:YAG laser. The KE is estimated from time duration between the irradiation of the vaporization laser and the ion detection.

VI-3. Results

Figure VI-3a shows a typical TOF mass spectrum of the nascent cluster ions produced by the collision of the Mg^+ ions with water clusters in the source. Both $Mg^+(H_2O)_n$ and $MgOH^+(H_2O)_{n-1}$ ions are found to be produced by the reactions as follows,

$$Mg^+ + (H_2O)_n \rightarrow Mg^+(H_2O)_m + (n\text{-}m)H_2O \qquad \text{(VI.1)}$$

$$\rightarrow MgOH^+(H_2O)_m + H + (n\text{-}m\text{-}1)H_2O \qquad \text{(VI.2)}$$

Though the Mg atoms have isotopes, the abundances of the above two series of cluster ions, which appear with intervals of unit mass in the mass spectrum, are estimated from the known isotopic abundances (hereafter, Mg^+ refers to the most abundant $^{24}Mg^+$ ion). Figure VI-4a shows the relative abundances of $Mg^+(H_2O)_n$ and $MgOH^+(H_2O)_{n-1}$ determined from the mass spectrum. These cluster ions are produced with characteristic size distribution: For $1 \leq n \leq 5$ and $n \geq 15$, the $Mg^+(H_2O)_n$ ions are dominantly produced. In contrast, $MgOH^+(H_2O)_{n-1}$ are exclusively observed for $6 \leq n \leq 14$. The results indicate that the product ions switch rapidly at two critical cluster sizes such as n=5 and 15. These features are not affected by the stagnation pressure of expansion and the fluence of the vaporization laser. The author also examine the reaction by placing the metal rod at the exit of the pulsed nozzle and the product ions are found to exhibit the same mass distribution. For the Mg^+-D_2O system, the similar product switchings except for the shifts of critical sizes are found; the $Mg^+(D_2O)_n$ ions are dominant for $1 \leq n \leq 6$ and $n \geq 14$, while $MgOD^+(D_2O)_{n-1}$ are exclusively observed for $7 \leq n \leq 14$ as shown in Figure VI-4b.

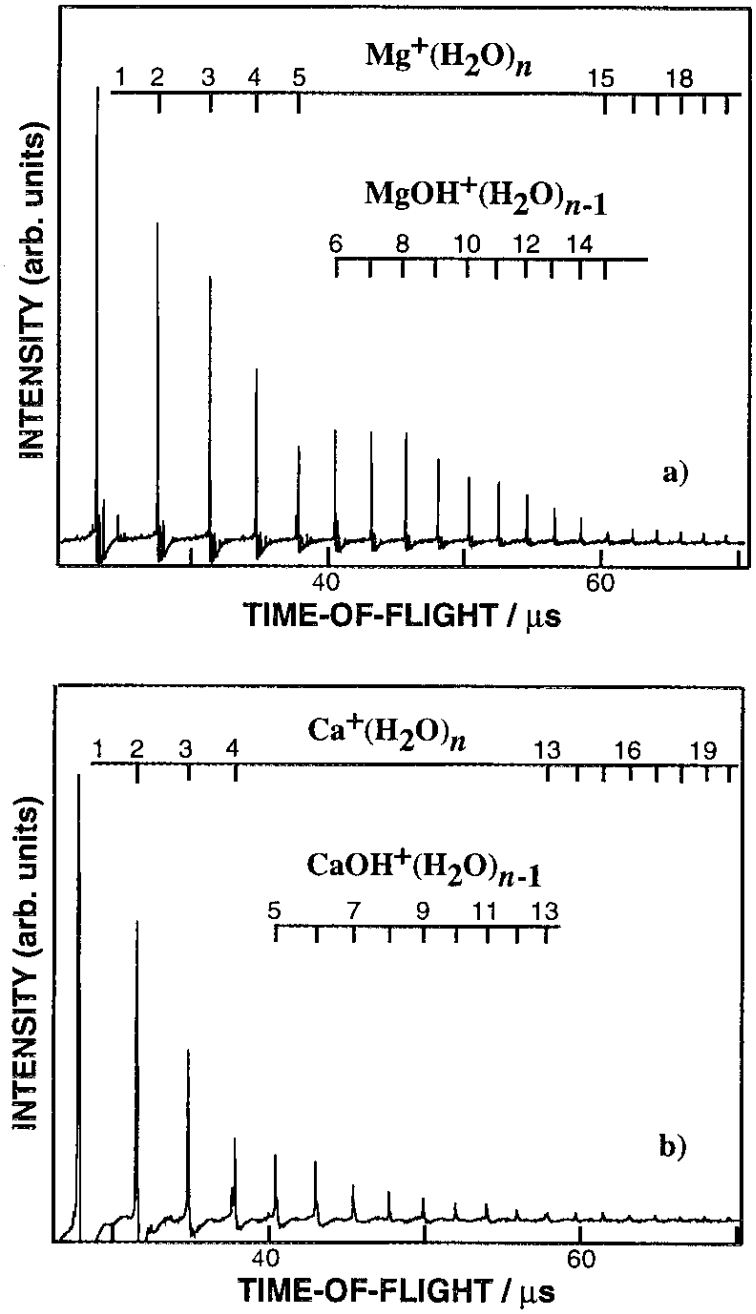

Figure VI-3. TOF mass spectra of the product ions for the reaction of the singly charged metal ions (M^+) with water clusters in the pickup cluster source; (a) for Mg^+ and (b) for Ca^+, respectively.

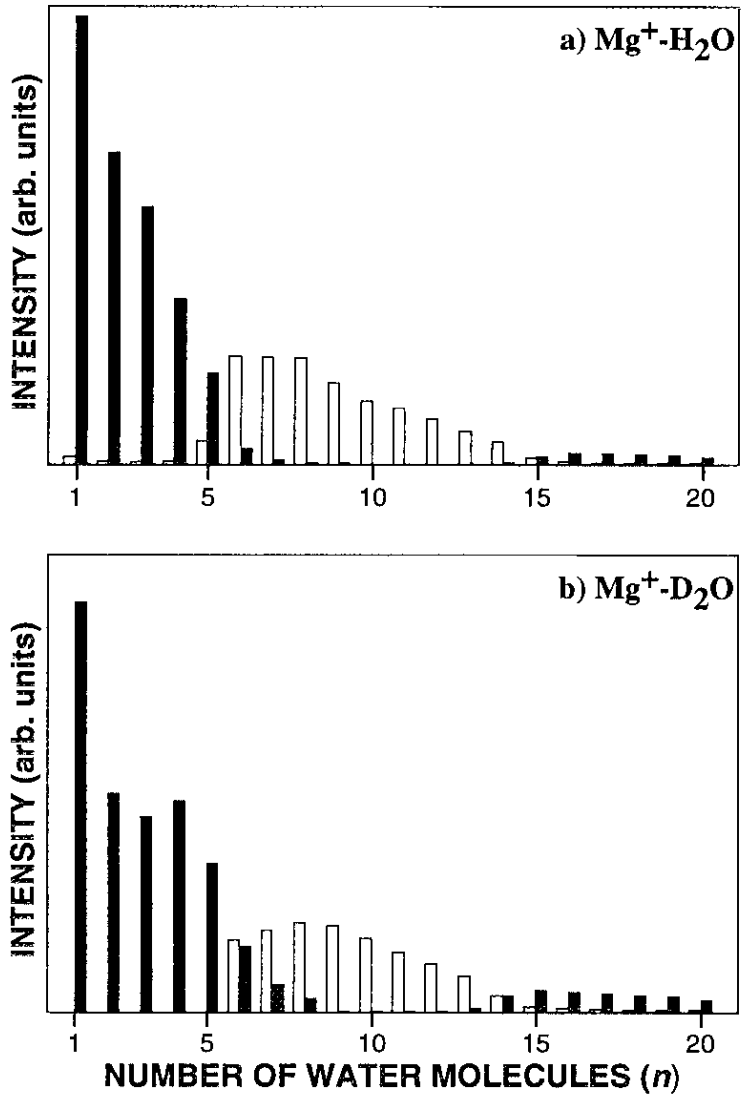

Figure VI-4. Relative abundances for Mg^+-H_2O(a) and Mg^+-D_2O(b) systems. The bars in the figures correspond to the hydrated Mg^+ (filled) and hydrated $MgOH^+$ (opened) , respectively.

Figures VI-3b and VI-5c show a typical TOF mass spectrum and the relative abundances of the nascent cluster ions determined from the mass spectrum for the reaction of the Ca^+ ions with water clusters (Ca^+ refers to the most abundant $^{40}Ca^+$ ion). As in the case of the Mg^+ ions, both the $Ca^+(H_2O)_n$ and $CaOH^+(H_2O)_{n-1}$ ions are produced with the similar product switchings; the critical sizes are n=4 and 13. In contrast to the case of Mg^+, the product distribution is extensively affected by the deuterium substitution as shown in Figure VI-5d: Although the hydrated $CaOD^+$ ions are formed for $5 \leq n \leq 12$, the $Ca^+(D_2O)_n$ ions persist in this size range.

In order to clarify the origin of the product distributions, I also examined the photodissociation processes of $Mg^+(H_2O)_n$ (n=1-5), which may correspond to the half collision process of the above reactions. These clusters have found to exhibit the strong absorption bands at the visible and near UV regions, which are ascribed to the ^2P-^2S transition of the free Mg^+ ion, shifted as a result of hydration. The photoexcitation of these clusters induces an H-atom elimination reaction to produce $MgOH^+(H_2O)_n$ in addition to the simple evaporation of water molecules; the reaction depends strongly both on the photoexcitation energy and the cluster size. The results of these photodissociation processes are described in Chapter IV. In this work, the branching ratios of the photoinduced reaction for these clusters were reexamined, because it provides us a clue to understand the origins of the anomalous distributions of the nascent cluster ions. Figure VI-6 shows a typical result on the reactive fractions for $Mg^+(H_2O)_2$ as a function of the photolysis energy. For comparison, the photodissociation spectrum is also presented: the band at 25000 cm^{-1} corresponds to the transition to the 1^2B state and the broad intense band at ca. 30000 cm^{-1} is the overlapped transitions to the higher two electronic states (2^2B and 2^2A). As discussed in Chapter IV, the reaction proceeds directly through the 2^2B state (and

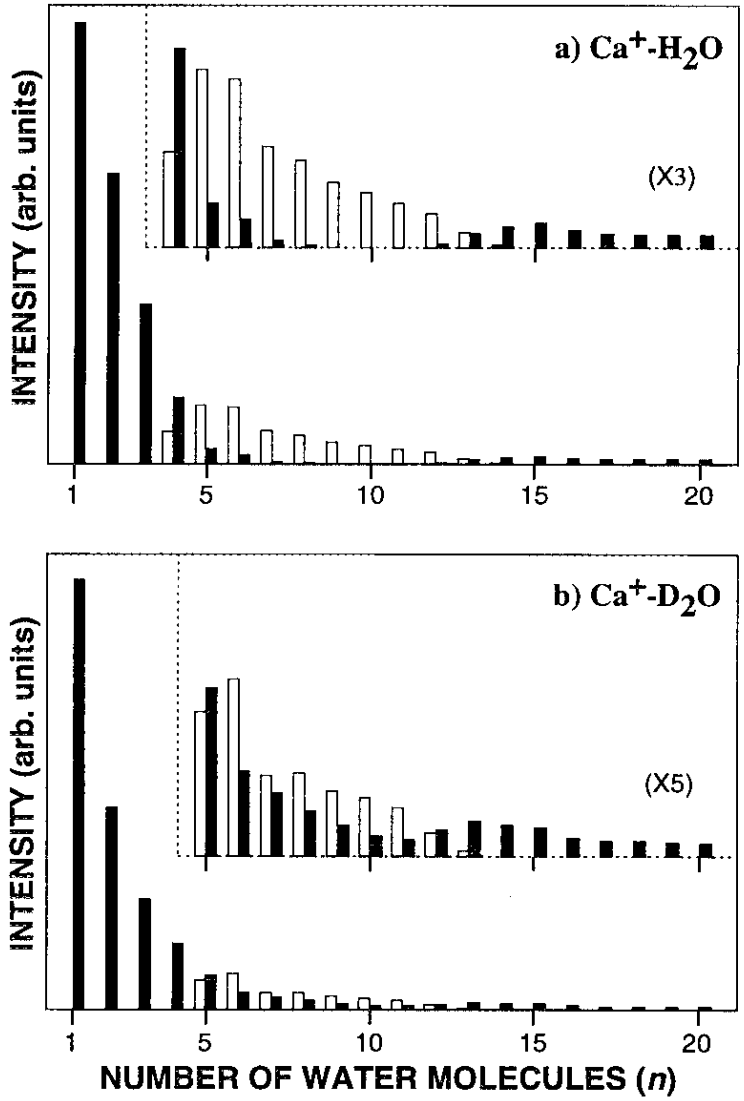

Figure VI-5. Relative abundances for Ca^+-H_2O(a) and Ca^+-D_2O(b) systems. The bars in the figures correspond to the hydrated Ca^+ (filled) and hydrated $CaOH^+$ (opened) , respectively.

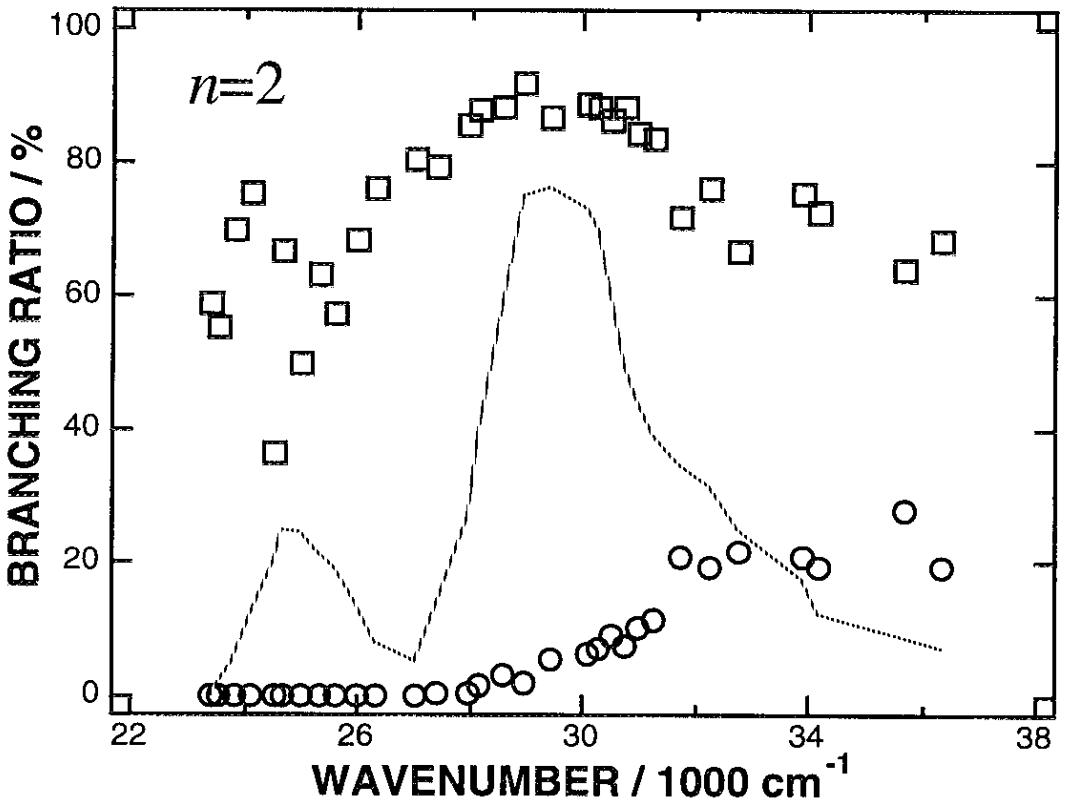

Figure VI-6. Branching fractions of the photoinduced reaction products for $Mg^+(H_2O)_2$ plotted vs. photon energy from 22000 - 38000 cm^{-1}; (□) for $MgOH^+(H_2O)$ and (○) for $MgOH^+$, respectively. The dashed curve corresponds to the photodissociation spectrum of $Mg^+(H_2O)_2$ described in Chapter IV.

probably also 2^2A), while the low-lying 1^2B state seems to be nonreactive and the reaction is considered to take place on the ground-state surface after crossing back from the initially excited state through a fast internal conversion process. As seen in Figure VI-6, the H-atom loss to produce $MgOH^+(H_2O)$ is the dominant process for the $Mg^+(H_2O)_2$ photodissociation. The evaporation of a water molecule from the primary product ions to produce $MgOH^+$ also occurs in the higher energy region. The mechanism of these processes is shown schematically in Figure VI-7. The onset of the $MgOH^+$ ion production gives the threshold energy of the process,

$$[Mg^+(H_2O)_2] \rightarrow MgOH^+(H_2O) \rightarrow MgOH^+ + H_2O \qquad \text{(VI.3)}$$

as 29000 cm^{-1} (83 kcal/mol) with respect to the ground-state $Mg^+(H_2O)_2$. Figures VI-8 and VI-9 show the reactive fractions for the $Mg^+(H_2O)_3$ and $Mg^+(H_2O)_5$ ions indicating the similar evaporation threshold behaviors. These results give the threshold energies for the processes,

$$[Mg^+(H_2O)_3] \rightarrow MgOH^+(H_2O)_2 \rightarrow MgOH^+(H_2O) + H_2O, \qquad \text{(VI.4)}$$

and

$$[Mg^+(H_2O)_5] \rightarrow MgOH^+(H_2O)_3 \rightarrow MgOH^+(H_2O)_2 + H_2O \qquad \text{(VI.5)}$$

as 21600 cm^{-1} (65 kcal/mol) and 19700 cm^{-1} (56 kcal/mol), respectively. Thus if the successive binding energies between the Mg^+ with water molecules are available, the binding energy of the $MgOH^+$ ion is estimated by using the Born cycle as shown in Figure VI-10. Unfortunately, the binding energies for $Mg^+(H_2O)_n$ have not yet been determined experimentally except

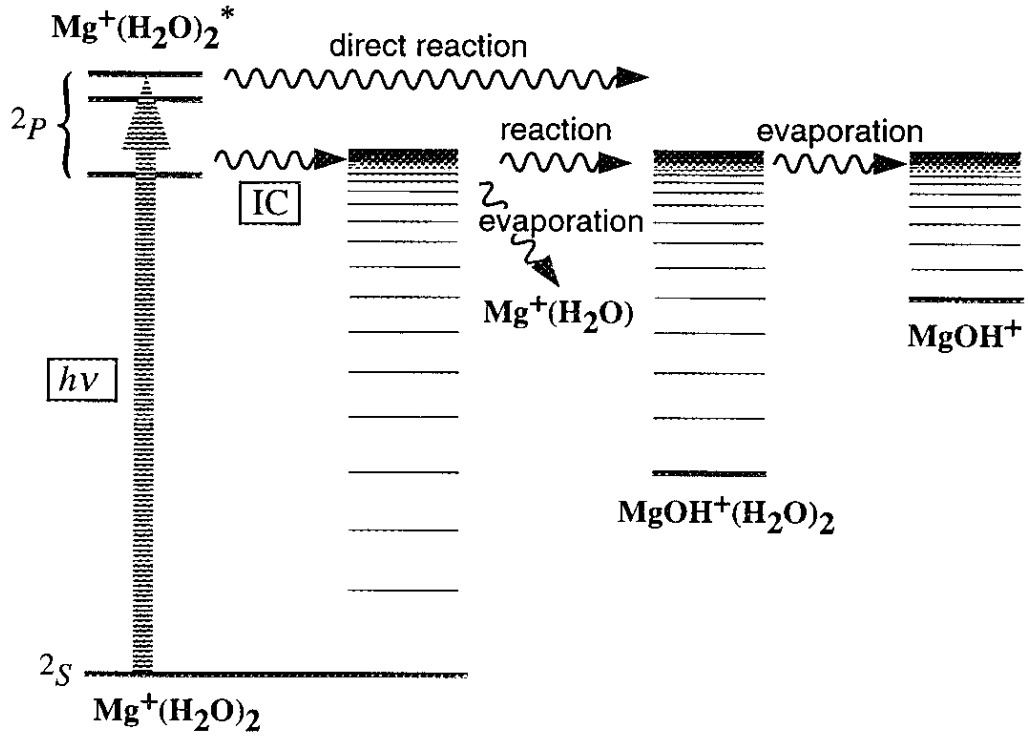

Figure VI-7. Schematic drawing for the photodissociation process of $Mg^+(H_2O)_2$.

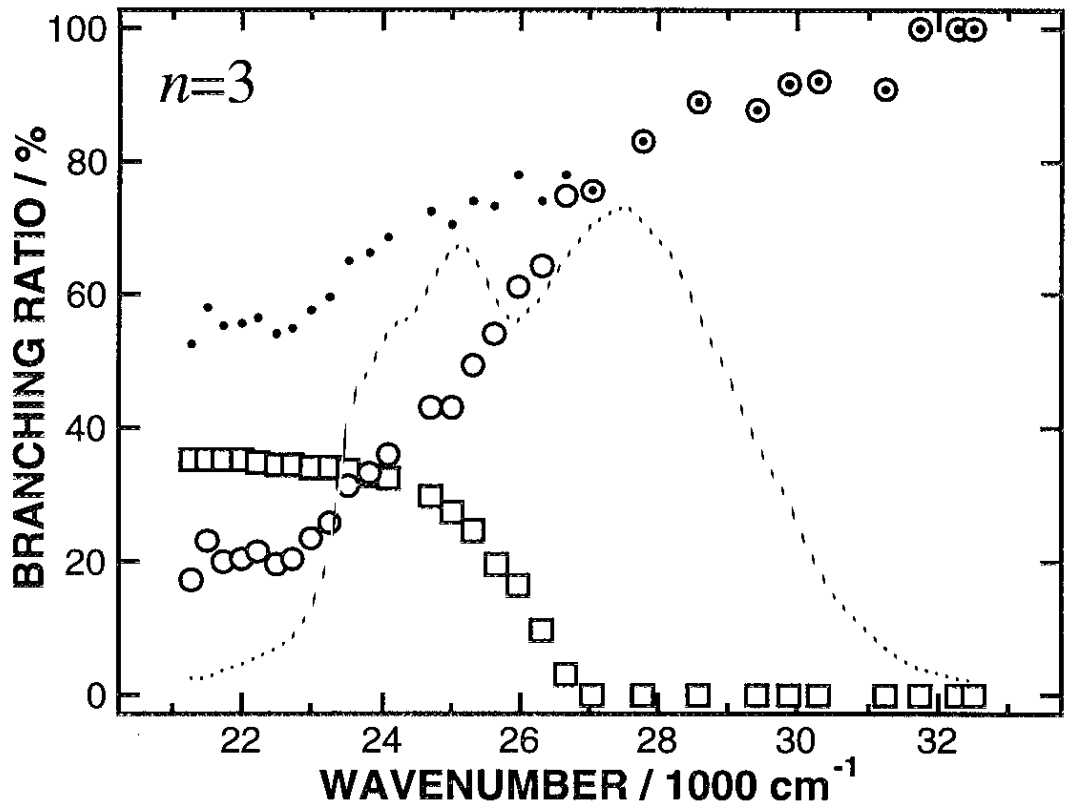

Figure VI-8. Branching fractions of the photoinduced reaction products for $Mg^+(H_2O)_3$ plotted vs. photon energy from 21000-29000 cm^{-1}; (□) for $MgOH^+(H_2O)_2$ and (○) for $MgOH^+(H_2O)$, respectively. The dots represent the total fraction of the reaction products. The dashed curve corresponds to the photodissociation spectrum of $Mg^+(H_2O)_3$ described in Chapter IV.

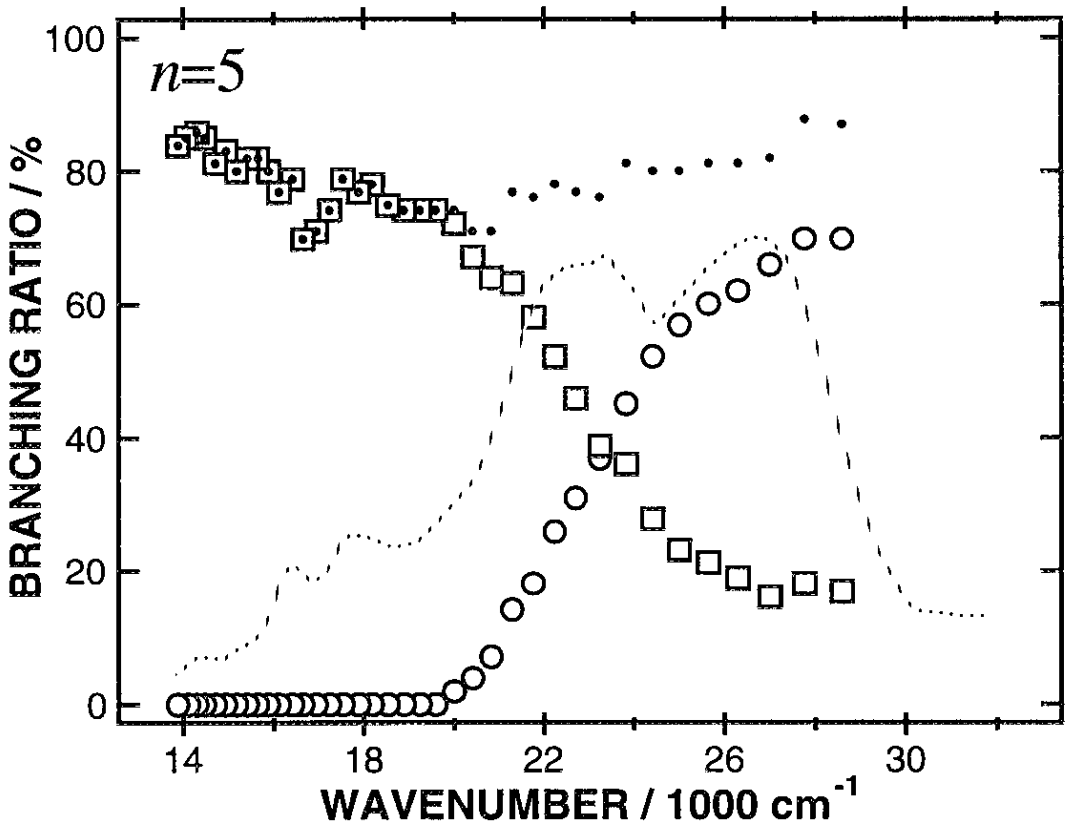

Figure VI-9. Branching fractions of the photoinduced reaction products for $Mg^+(H_2O)_5$ plotted vs. photon energy from 13800-29000 cm^{-1}; (□) for $MgOH^+(H_2O)_3$ and (○) for $MgOH^+(H_2O)_2$, respectively. The dots represent the total fraction of the reaction products. The dashed curve corresponds to the photodissociation spectrum of $Mg^+(H_2O)_5$ described in Chapter IV.

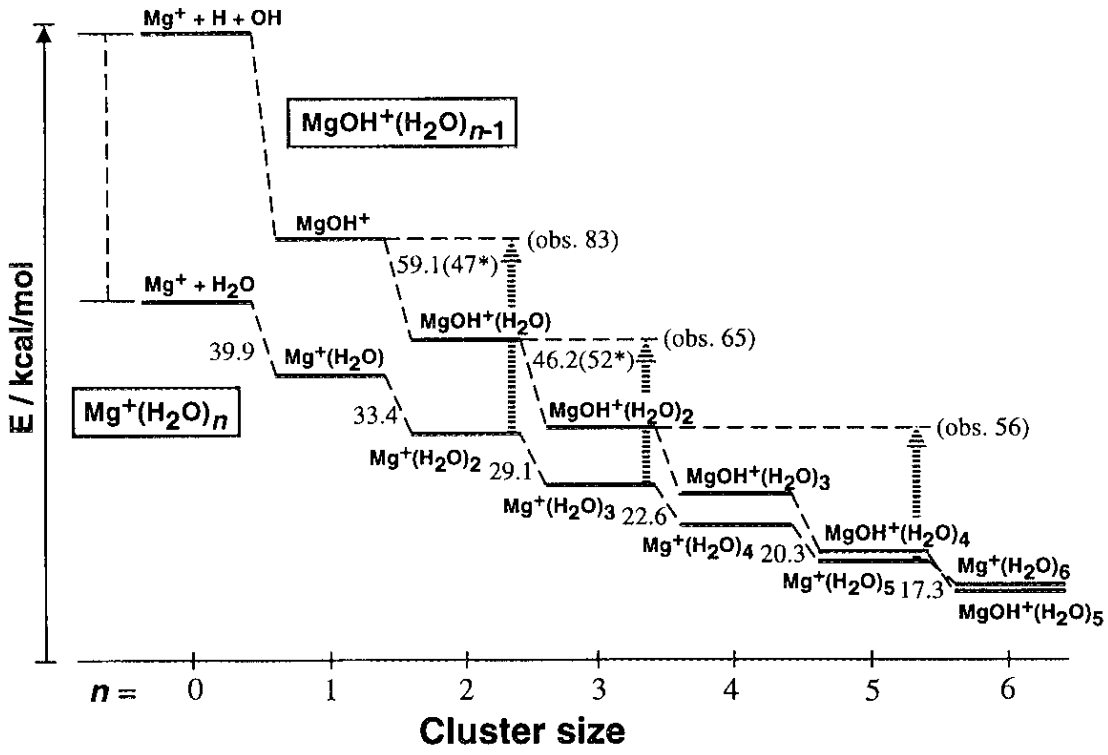

Figure VI-10. A schematic energy diagram for $Mg^+(H_2O)_n$ and $MgOH^+(H_2O)_{n-1}$ and the thermochemical Born-Haber cycle for the product ions formed in the intracluster reaction of $Mg^+(H_2O)_n$. The numbers labelled (*) are determined from the evaporation threshold energies.

for n=1. Duncan and his co-workers have estimated the binding energy for the ground-state Mg^+-H_2O ion as 24.3 kcal/mol from the excited-state dissociation energy determined by a Birge-Sponer (BS) plot of the vibronic bands for the $^2B_2$-$^2A_1$ transition [13]. However, as they pointed out, both the dissociation and binding energies may include large errors, because they estimated the dissociation energy by the BS extrapolation with the limited number of vibrational levels and also the Morse function assumed in the BS plot is not well characterized for metal ion-ligand interaction. In fact, their number is significantly smaller than the theoretical results such as 32 and 39.9 kcal/mol [10,14]. Therefore, the author adopt the calculated successive binding energies, 33.4, 29.1, 22.6, and 20.3 kcal/mol for n=2-5, respectively, obtained by the present authors [14]. Consequently, the Born cycles give the binding energies, $\Delta H_{1,0}$ for $MgOH^+$-H_2O and $\Delta H_{2,1}$ for $MgOH^+(H_2O)$-H_2O, as 47 and 52 kcal/mol, respectively. They are in reasonably good agreement with the theoretical predictions of 59.1 and 46.2 kcal/mol, respectively, though the ordering is wrong; this reversed trend may be due to a slight overestimation of the $Mg^+(H_2O)_{n-1}$-H_2O binding energies in the present calculations.

As mentioned previously, the reaction between alkaline-earth metal ions and water clusters yields the characteristic product distributions exhibiting the product switchings at two critical sizes. In order to understand this "anomalous" product distributions, the author examine the reaction for the Mg^+-H_2O system with different collision energy using the simple cross beam assembly. The Mg^+ ions produced by the laser vaporization method have a wide kinetic energy (KE) distribution as shown in Figure VI-2. Since the reaction examined here takes place under multiple collision condition, it is intrinsically difficult to specify the collision energy for the reaction; before the reactive collision takes place, the initial KE of metal ions may decrease to

various extent by collisions with He atoms. By varying the extraction field, the KE effect on the reaction products is obtained, though it is qualitative. Figure VI-11 shows the mass spectra for the product ions at three KEs. At a relatively low KE (ca. 20 eV), the product distribution is much the same as that recorded with the pickup source (see Figure VI-3a), except for the rather weak signals for n=1-4. The decrease in the signal intensities for these ions may be partly due to the fact that these ions are formed by a collision of Mg^+ with rather small water clusters, and as a result, the product ions are deflected from the water cluster beam by an initial momentum of Mg^+. At higher KE, the signals for the larger product ions decrease significantly as seen in Figures VI-11b and VI-11c, because a large deposited energy may enhance the evaporation of water molecules from the product ions. These results indicate that the critical sizes of the product switchings unchanged within the present KE range. This observation implies an important clue to understand the product switching as discussed later.

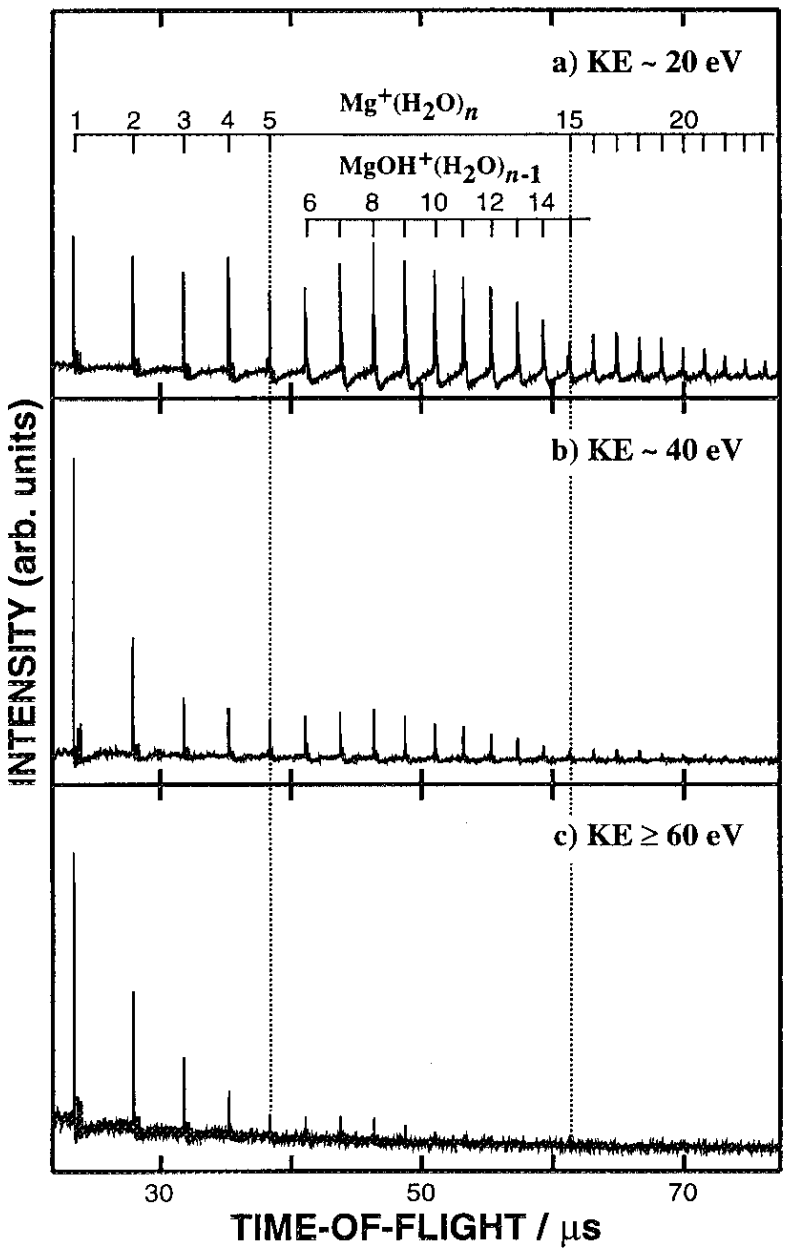

Figure VI-11. KE dependence on the product ion distribution for the reaction between Mg^+ and water clusters obtained by using the crossed beam assembly. KEs of the Mg^+ ion are determined from time duration between the irradiation of the vaporization laser and the ion detection. The energy resolution is estimated to be ±5 eV.

VI-4. Discussion

VI-4.1. Features of Reaction

In this study, the clusters are formed by the collision of metal ions generated by the laser vaporization with water clusters. Especially, in the case of the pickup source, the metal rod was placed closely to the water cluster beam. As a result, the metal ions with various states are possible to contribute to the final product distributions observed in the mass spectrum. Both singly and doubly charged ions are generated by the laser vaporization. The fraction of the latter ion is found to depend strongly on the laser fluence and is less than 0.1 under the present experimental condition. Thus the contribution of the doubly charged ions in the product distribution is negligible. The author must also consider the possible existence of the excited-state ions such as $M^+(^2P)$ in the ejected singly charged ions. However, these ions may not contribute to the final product distribution, because its radiative lifetime is too short to take part in the reaction; the lifetime of $Mg^+(^2P)$ is 3.7×10^{-9} s [15]. The fact that the mass spectrum obtained by the crossed beam assembly exhibits the same features for the product switching as those observed for the pickup source supports this conclusion. Therefore, the product distributions examined here are mostly due to the reaction of $Mg^+(^2S)$ with water clusters. The same arguments are also valid for the reaction of Ca^+.

As mentioned previously, the metal containing clusters are produced by injecting Mg^+ into the water cluster beam and the reaction proceeds with multiple collision condition. And also the Mg^+ ions have a large kinetic energy distribution as shown in Figure VI-2. Therefore it is difficult to examine the mechanism of the reaction quantitatively. But, fortunately, the photodissociation process of $Mg^+(H_2O)_n$ involves the same H-atom

elimination reaction in the collision reaction as well as the evaporation of water molecules. As discussed in Chapter VI, the reaction depends strongly on the number of ligated waters and the photolysis energy. For n=1, the reaction takes place on the ground-state surface after crossing back from the initially excited state through a fast internal conversion process. In contrast, the excited-state reaction channel seems to be opened for n=2 and 3, especially in the higher excited states of these clusters. For larger clusters, the ground-state channel seems to be dominant because of the rapid increase of internal conversion rate due to the second shell water molecules: The results on the photodissociation spectra and the *ab initio* calculations of the geometrical structures for these clusters clearly demonstrate that the first solvation shell around the Mg^+ ion is closed with three water molecules [10,14]. Although these intracluster reactions are not exactly the half-collision analogs of those occurred in the cluster source as discussed later, it still provides us a wealth of insights into the intrinsic nature of the cluster reactions. As noted above, the excited-state channel is not predominant for the intracluster reactions, because the reaction mechanism is considered to be an insertive one and the relative orientation of Mg^+ and water molecule is essential for the reaction to take place; the water molecules ligate to the metal ion through the oxygen atom, and as a result, the excitation of a bending vibrational mode seems to be necessary for the system to reach an insertion-type transition state followed by the H-atom elimination. The results on the intracluster reaction also suggest that the second shell water molecules may play some role in switching the reaction mechanism: The degrees of freedom of the clusters increase rapidly with the number of water molecules, and as a result, the internal conversion and vibrational relaxation rates are rapidly enhanced. It is worth to note that the reaction to produce the hydrated $MgOH^+$ ions is found to be predominant for n=4 and 5 and the evaporation of

water molecules is the minor process. These results imply that the second shell water may not play the role of a solvent cage in the H-atom elimination as far as the cluster size is up to five water molecules. This is partly due to the fact that the reaction occurs mainly on the higher vibrational levels in the ground state; a hot chemistry takes place in the cluster.

In the present experimental setup, the reaction occurs at the region wherein the density of the carrier gas is still high enough to partially thermalize the metal ions before collision with water clusters. Moreover, water clusters having a wide size distribution take part in the reactions, in which a long-lived collision complex is expected to mediate. As for the smaller water clusters, the reaction after forming the collision complex is expected to be similar to those for the photoinduced intracluster reactions mentioned previously. On the other hand, the features of the reaction for the larger clusters may be much different from those for the intracluster reactions. In this case, a large amount of energy released by the solvation of metal ion in addition to the initial collision energy may accelerate the reaction as well as the evaporation of water molecules. The mechanism of these reactions should be quite complex and it is difficult to get further insight into these mechanism with the present experimental data alone. However, the critical sizes of the product switchings are not affected by the experimental conditions as mentioned previously. In the following sections, I will discuss the mechanisms of the product switchings with considering these reaction features.

VI-4.2. First Product Switching

As shown in Figure VI-4a, the $Mg^+(H_2O)_n$ ions are produced exclusively for n up to 5, while the $MgOH^+(H_2O)_{n-1}$ ions are the unique products for n larger than 5. Although a small amount of $MgOH^+$-cored

clusters is also observed for the smaller size, these clusters may be formed by the laser ablation of MgOH deposited on the surface of the Mg rod; the fact that these cluster ions are not detected in the crossed beam experiment may support this conclusion. The above results indicate that the formation of the $MgOH^+(H_2O)_n$ requires at least five water molecules. As mentioned previously, the critical size is not affected by the reaction conditions, and thus, the product switching may be caused not by the reaction dynamics but by the thermodynamical stability of the product ions.

The photodissociation study of the mass-selected $Mg^+(H_2O)_n$ ions provides us important information on the binding energy of the $MgOH^+$ ion with water molecules. As seen in Figures VI-6, VI-8 and VI-9, the $MgOH^+$-cored cluster ions exhibits the threshold behaviors. From these results, we determine the binding energies of the $MgOH^+$ and $MgOH^+(H_2O)$ ions with a water molecule as 47 and 51.7 kcal/mol, respectively; the reversed trend is due to the overestimation of the $Mg^+(H_2O)_{n-1}$-H_2O binding energies as mentioned previously. Iwata *et al.* also performed the theoretical calculations for the geometrical structures and the binding energies for the $MgOH^+(H_2O)_n$ (n=1-6) clusters. The calculated binding energies for the $MgOH^+$-H_2O and $MgOH^+(H_2O)$-H_2O are 59.1 and 46.2 kcal/mol, respectively, and are in reasonably good agreement with the experimental results. Interestingly, these binding energies are much larger than those for the Mg^+-H_2O and $Mg^+(H_2O)$-H_2O ions; the calculated binding energies are 39.9 and 33.4 kcal/mol, respectively, as shown in the preceding section. According to the theoretical calculations, the $MgOH^+$ ions polarize significantly and the effective charge on the Mg atom is predicted to be more than +1.6. This polarization enhances the bonding with water and the $MgOH^+(H_2O)_n$ ions may be stabilized much faster than those for $Mg^+(H_2O)_n$ with increasing n . Consequently, the former ions become the ground state of the system at a certain cluster size as

schematically shown in Figure VI-10. In fact, these expectations are confirmed by the theoretical calculations for the larger water clusters containing Mg^+ and $MgOH^+$ as reported in Ref. 14. Therefore, the first product switching observed in the mass spectrum is ascribed to the difference in hydration energies for the Mg^+ and $MgOH^+$ ions; the reaction,

$$Mg^+(H_2O)_n \rightarrow MgOH^+(H_2O)_{n-1} + H \qquad \text{(VI.6)}$$

becomes thermodynamically feasible for $n \geq 6$ [16]. Needless to say, the amount of the effective charge mentioned above indicates that the partial oxidation of the Mg^+ ions occurs through the reaction (VI.6).

As seen in Figure VI-4b, the critical size for the product switching for Mg^+ shifts to n=6 and the feature of the switching becomes rather obscure by the deuterium substitution; the similar tendency is also observed for the Ca^+-water clusters as discussed below. As the origin of the isotope effect, one might consider a dynamical effect such as a caging of the H-atom elimination, however, these shifts seem to be ascribed to a thermodynamical origin as follows. The zero-point energies of the reactant and product in the reaction (VI.6) should be altered by the deuterium substitution; the vibrational degrees of freedom for the clusters decreases by 3 upon the reaction takes place. The contribution of an O-H stretching vibrational mode is the largest among these degrees of freedom. In fact, the theoretical calculations predict that the decrease in enthalpy of the reactant $Mg^+(H_2O)_5$ by substitution is calculated to be 3 kcal/mol larger than that for the product $MgOH^+(H_2O)_4$ [14]. In addition to these results, the differences in the solvation enthalpies for Mg^+ and $MgOH^+$-cored clusters are much small for n=6-8, as expected from the fact that a small amount of the $Mg^+(H_2O)_n$ ions coexist with $MgOH^+(H_2O)_{n-1}$ for these sizes as seen in Figure VI-4a. Therefore, if a thermal equilibrium is

attained in these clusters, the small decrease in enthalpy change arised from the isotope substitution may shift the equilibrium in reaction 6 to the left.

The author also observe the similar product switching for the Ca^+-water cluster reaction. As shown in Figure VI-5d, the critical size of the first product switching shifts to the smaller size from Mg^+ (n=5) to Ca^+ (n=4). The origin of this product switching is expected to be the same as that for Mg^+. In contrast to the case of Mg^+, the $Ca^+(D_2O)_n$ cluster ions are also detected even for $n \geq 5$: Both $Ca^+(D_2O)_n$ and $CaOD^+(D_2O)_{n-1}$ are the stable products for $5 \leq n \leq 12$, while the former ions are exclusively produced for $n \geq 13$. The large deuterium substitution effect on the product distributions for Ca^+ may be ascribed to weaker bindings for both Ca^+ and $CaOH^+$ [17]. Since the bondings for these clusters are mostly electrostatic in nature and the ionic radius of the Ca^+ ion (1.18 Å) is much larger than that for the Mg^+ ion (0.82Å), the differences in the enthalpies for $Ca^+(H_2O)_n$ and $CaOH^+(H_2O)_{n-1}$ ($5 \leq n \leq 12$) are expected to be smaller than those for $Mg^+(H_2O)_n$ and $MgOH^+(H_2O)_{n-1}$. On the other hand, the enthalpy changes due to the deuterium substitution may be almost the same for both systems because it originates mainly from the ligated water molecules. These arguments seem to be consistent with the observation that the substitution effect on the product distribution is much larger for Ca^+ than that for Mg^+. The above results indicate that the differences in energy for $Ca^+(H_2O)_n$ and $CaOH^+(H_2O)_{n-1}$ ($5 \leq n \leq 12$) are close to the aforementioned enthalpy change due to the deuterium substitution (ca. 3 kcal/mol for the Mg^+ system). This small difference may suggest that the enthalpies of solvation for larger clusters are determined mostly by the hydrogen bonding energy among ligated water molecules.

VI-4.3. Second Product Switching

For $n \geq 15$, the $Mg^+(H_2O)_n$ ions again become the stable products as mentioned previously (see Figure VI-4a). The similar product switchings are also observed for $Mg^+(D_2O)_n$ at $n=14$, for $Ca^+(H_2O)_n$ at $n=13$, and for $Ca^+(D_2O)_n$ at $n=12$ as shown in Figures VI-4b, VI-5a, and VI-5b, respectively. Because of the observations that the critical size for the second switching is affected by the deuterium substitution, an origin is expected to stem from the reaction dynamics related to a tunneling process. For the reaction with such a large water clusters, water molecules surrounding the metal ions may play the role of solvent cage, which may cause an energy barrier along the reaction path. Thus, the trapping probability of the ejected H-atom upon the reaction may increase with increasing cluster size, and as a result, the reaction may be suppressed for the larger clusters. If this is the case for the second switching, the reaction, in which the tunneling process may intervene, is affected by deuterium substitution. However, this mechanism seems to be inconsistent with the observations that the critical sizes are not affected by the initial KE of metal ions and the experimental configurations for the cluster production as noted previously. These arguments suggest that the second product switching originates not from the reaction dynamics but from some thermodynamical factors.

As for the thermodynamical origins for this "reversed" product switching, the author can consider at least three possibilities. One of the candidates may be the involvement of a H-Mg^+-OH ions. This ion was proposed to be a short-lived intermediate for an insertion-type reaction observed in the photodissociation of the Mg^+-alcohol complexes [18]. The preliminary results for the H–$MgOH^+$ calculations predict that this ion locates 77 kcal/mol above the stable $Mg^+(H_2O)$ ion and the H–$MgOH^+$ binding energy is 4.3 kcal/mol [14]. In the photodissociation study for $Mg^+(H_2O)_n$,

$n \leq 5$, the author could not observe any indication for the involvement of this ion as the products; this ion seems to be short-lived because the vibrationally excited products are formed in the intracluster reactions and the weaker Mg^+–H bond may easily be broken. However, for the clusters with more than ten water molecules, the author could expect that the heat bath becomes huge enough to stabilize the H-Mg^+-OH ions before the bond breaking. In the case of $MgOH^+$, the successive hydration energies are much larger than those for Mg^+ because of its large polarization. As a result, the hydrated $MgOH^+$ ions become lower in energy than the hydrated Mg^+ ions as mentioned previously. This is not the case for H-Mg^+-OH, where the positive charge delocalizes over the whole ion, but its successive hydration energies are expected to be smaller than those for Mg^+ because of its large effective ion radius. Therefore, the hydrated H-Mg^+-OH ions may not become the ground state of the system and are ruled out as the possible origin for the second product switching.

They found that the ^2P-^2S transition of Sr^+ ion shifts to the red as large as 17000 cm^{-1} with n up to 6. On the basis of the spectral moment analysis of the cross sections, the spectral shifts were ascribed to increasing ion-pair character in the ground and excited state wave functions of the metal ion with increasing cluster size; they predicted a large increment of the square of the electronic radial distribution in the ground state with increasing n. I also examined the photodissociation spectra for the mass-selected cluster ions $Ca^+(H_2O)_n$ (n=1-6) as mentioned in Chapter V[19]. The spectra for this entire series of clusters show similar large redshifting as much as 18000 cm^{-1} with respect to the atomic resonance lines of the free Ca^+ near 395 nm. Although we might consider a contribution of the mixing of the ^2P state and the low-lying ^2D states in the spectral shifts, a rapid stabilization of solvated ion-pair states with increasing cluster size as in the case of $Sr^+(NH_3)_n$ is also the

possible mechanism for the large spectral redshifting. These arguments encourage us to propose the ion-pair state as the origin for the second product switching. As was discussed by Farrar *et al.*, the $M^{2+}(H_2O)_n^-$ state stabilizes much faster than the ground state of $M^+(H_2O)_n$ because the size-dependent stabilization of the former state is dominated by the solvation of the doubly charged M^{2+} species. Moreover, the electron affinities of water clusters were found to be positive for the clusters as small as n=11 in contrast to the case of ammonia clusters, which were reported to be negative for $n \leq 34$ [20]. Thus the ion-pair state lowers in energy and may becomes the ground state of the system as shown schematically in Figure VI-12. As seen in Figures VI-4a and VI-5a, the critical size for Mg^+ is observed at n=15, while that for $Ca^+(H_2O)_n$ is n=13. These numbers are consistent with the IPs of these metal ions: The IPs, 15.0 eV for Mg^+ and 11.9 eV for Ca^+, respectively, suggest that the number of water molecules to stabilize M^{2+} as low as the hydrated M^+ ions should be smaller for Ca^{2+}. These results may also support the ion-pair character of the ground-state $M^+(H_2O)_n$ for larger clusters. Therefore the change in the electronic character of the ground state is the plausible mechanism for the second product switching of the metal ion-water cluster reaction.

The mechanism involving the ion-pair state is important in analogy with the solvation process of metal ions in bulk solution because it includes the fundamental issue on how the electron on the metal atom delocalizes with increasing the degree of hydration. Relating to this issue, Kebarle and his co-workers succeeded to produce the water clusters containing double-charged alkaline-earth metal atoms such as $Mg^{2+}(H_2O)_n$ and $Ca^{2+}(H_2O)_n$ (n=7-13) using an electrospray method [21]. Since the second IPs of M, Mg and Ca, are close to or larger than the IP of water (12.6 eV), the collisional association of M^{2+} and water used generally for the hydrated metal ions production

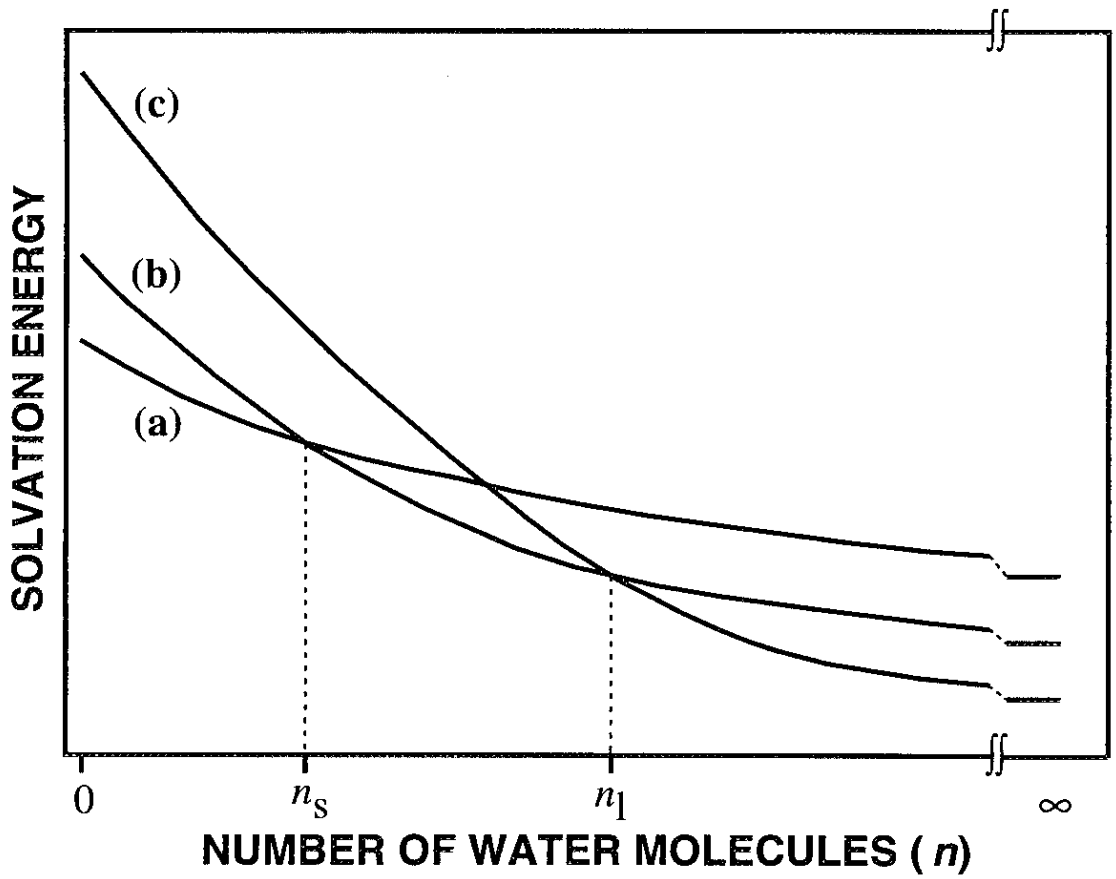

Figure VI-12. Schematic energy diagram for $M^+(H_2O)_n$ (a), $MOH^+(H_2O)_{n-1}$ (b) and the ion-pair states $M^{2+}(H_2O)_n^-$ (c), as a function of cluster size (n). n_S and n_I represent the crossing points between these curves, which correspond to the critical sizes of the first and second product switchings, respectively.

causes a charge reduction to produce $M^+ + H_3O^+$. To overcome this situation, they used the method in which the hydrated doubly charged ions are transferred from the liquid to the gas phase. Their results clearly indicate that, if the method to produce hydrated metal ions is mild, doubly charged metal ions having much larger IP than that of water are possible to trap in water clusters without charge reduction as in the case of bulk aqueous solution. These hydrated doubly-charged metal ions should have a positive electron affinity. Therefore the Rydberg-like ion-pair state mentioned above is expected to exist if the screening effect of water molecules ligated to the metal ion is enough effective to prevent charge recombination.

On the other hand, the present method to produce hydrated metal ions is the other extreme and the chemical reaction path might be possible to surmount the ion-pair state formation even for larger clusters: The third possibility is the product formed by the reaction which follows reaction (VI.6). As mentioned previously, the partial oxidation of Mg^+ to produce $MgOH^+$ takes place in reaction (VI.6), which corresponds to the first product switching. This fact suggests us that the full oxidation of Mg^+ through the chemical reaction may take place for large clusters; the products are, for instance, such as $MgOH{\cdot}H_3O^+(H_2O)_{n-2}$. Since no experimental and theoretical data are available for this kind of ion, we cannot expect whether the ions are stabilized as much as the $MgOH^+$ ions by hydration. However, we might not rule out this mechanism as the origin of the second product switching.

At the present stage, it is difficult to conclude whether the ion-pair state formation or the new reaction product having the same mass to charge ratio as that for $Mg^+(H_2O)_n$ is responsible for the second product switching. In order to get further insight into the origin of this product switching, information on the electronic structures for the larger product ions are indispensable. For

Mg^+, the author cannot extend the photodissociation experiment for $n \geq 6$ because these ions are not stable products as noted previously. While, the $Ca^+(D_2O)_n$ ions for $n \geq 6$ are stable and the similar experiments for these cluster ions are currently underway in our laboratory.

VI-5. Conclusion

In this chapter, the reactions of the alkaline-earth metal ions such as Mg^+ and Ca^+ with the $(H_2O)_m$ and $(D_2O)_m$ clusters were examined. Both $M^+(H_2O)_n$ and $MOH^+(H_2O)_{n-1}$ are found to be formed with characteristic size distributions: The product ions switch at two critical sizes (n~5 and ~14). In order to clarify the origins for these product switchings, the author reexamined the photodissociation processes of $Mg^+(H_2O)_n$ ($n \leq 5$), which correspond to the half collision process of the cluster reactions. The photoexcitation was found to induce the evaporation of water molecules as well as the H-atom elimination reaction to generate the hydrated $MgOH^+$ ions: This reaction corresponds to the oxidation reaction of Mg^+. The reactive fraction as a function of the excitation energy exhibits the threshold behaviors for the evaporation of water molecules, from which the author determined the successive hydration energies of $MgOH^+$. The $MgOH^+$ binding energies are found to be much higher than those for Mg^+ because of its large polarization. Based on these results, the origin of the first product switching for n~5 was ascribed to the difference in the successive hydration energies of M^+ and MOH^+; the product, $MOH^+(H_2O)_{n-1}$ + H lowers much faster in energy than $M^+(H_2O)_n$ with increasing cluster size, and it becomes the ground state of the system for n~5. The critical size for the first product switching was also found to be affected by the deuterium substitution for both

Mg^+ and Ca^+ systems. This isotope effect was explained in terms of the difference in the zero-point energies for the reactant and product ions.

As for the second product switching for n~15, the origin is not self evident. Two possible mechanisms are proposed: such as the participation of the Rydberg-type ion pair state $M^{2+}(H_2O)_n^-$ and the formation of the new reaction product such as $MgOH{\cdot}H_3O^+(H_2O)_{n-2}$. The former mechanism is based on the results for the photodissociation spectra of $Ca^+(H_2O)_n$ and is an interesting candidate in relation to the solvation process of metal ion in bulk water. The latter mechanism stems from the chemical analogy. At present, the former mechanism is considered to be much plausible to understand the switching, however the author could not rule out the latter mechanism within the present experimental data. To confirm the mechanism, the photodissociation study for much larger clusters is indispensable.

The this study is one of the first experimental works which unveil the microscopic solvation dynamics of metal ions including the redox reactions in the gas phase clusters. The studies in this direction are considered to be important to gain the fundamental understandings for the many-body interactions of electrons and metal ions with ligands as well as for the solvation dynamics in bulk solution. The theoretical studies on the physical and chemical properties for large water clusters containing alkaline-earth metal ions are also helpful to get further insight into these issues.

References for Chapter VI

[1] P. Kebarle, *Ann. Rev. Phys. Chem.* **28**, 445 (1977).

[2] R. G. Keeseen and A. W. Castleman, Jr., *J. Phys. Chem. Ref. Data* **15**, 1011 (1986).

[3] P. B. Armentrout, *Ann. Rev. Phys. Chem.* **41**, 313 (1990).

[4] I. V. Hertel, C.Hüglin, C. Nitsch, and C. P. Schulz, *Phys. Rev. Lett.* **67** 1767 (1991).

[5] (a) F. Misaizu, K. Tsukamoto. M. Sanekata, and K. Fuke, *Chem. Phys. Lett.* **188**, 241 (1992). (b) K. Fuke, M. Misaizu, K. Tsukamoto, and M. Sanekata, In *Physics and Chemistry of Finite Systems*; edited by P. Jena, S. N. Khanna, and B. K. Rao, Vol. **II**, pp 925 (Kluwer: Dordrecht, 1992).

[6] R. N. Barnett and U. Landman, *Phys. Rev. Lett.* **70**, 1775 (1993).

[7] K. Hashimoto, S. He, and K. Morokuma,*Chem. Phys. Lett.* **206**, 297 (1993).

[8] (a) M. H. Shen, J. W. Winniczek, and J. M. Farrar, *J. Phys. Chem.* **91**, 6447 (1987). (b) M. H. Shen and J. M. Farrar, *J. Chem. Phys.* **94**, 3322 (1991). (c) S. G. Donnelly and J. M. Farrar, *J. Chem. Phys.* **98**, 5450 (1993).

[9] (a) F. Misaizu, M. Sanekata, K. Tsukamoto, K. Fuke, and S. Iwata, *J. Phys. Chem.* **96**, 8259 (1992). (b) K. Fuke, F. Misaizu, M. Sanekata, K. Tsukamoto, and S. Iwata, *Z. Phys.* D**26**, S180 (1993). (c) F. Misaizu, M. Sanekata, K. Fuke, and S. Iwata, *J. Chem. Phys.* **100**, 1161 (1994).

[10] (a) C. W. Bauschlicher, Jr. and H. Partridge, *J. Phys. Chem.* **95**, 9694 (1991). (b) C. W. Bauschlicher, Jr., M. Sodupe, and H. Partridge, *J. Chem. Phys.* **96**, 4453 (1992).

[11] C. A. Schmuttenmaer, J. Qian, S. G. Donnelly, M. J. DeLuca, D. F. Varley, L. A. DeLouise, R. J. D. Miller, and J. M. Farrar, *J. Phys. Chem.* **97**, 3077 (1993).

[12] P. Jégou, C. Granier, M. L. Chanin, and G. Mégie, *Ann. Geophys.* **3**, 163 (1985).

[13] (a) C. S. Yeh, K. F. Willey, D. L. Robbins, J. S. Pilgrim, and M. A. Duncan, *Chem. Phys. Lett.* **196**, 233 (1992). (b) K. F. Willey, C. S. Yeh, D. L. Robbins, J. S. Pilgrim, and M. A. Duncan, *J. Chem. Phys.* **97**, 8886 (1992).

[14] H. Watanabe, S. Iwata, H. Nakamura, K. Hashimoto, F. Misaizu, and K. Fuke, submitted in *J. Am. Chem. Soc.*

[15] A. A. Radzig and B. M. Smirnov, In *Reference Data on Atoms, Molecules, and Ions*, Springer Series in Chemical Physics **31** (Spring-Verlag: Berlin, 1985).

[16] Just before submitting this paper, Purnell, et al. reported the study on the dehydrogenation reactions in $Mg^+(H_2O)_n$ clusters to explain our earlier findings on the characteristic product distribution (*J. Chem. Phys.* **100**, 3540 (1994)). They reached to the same conclusion for the mechanism of the first product switching on the basis of the results for ligand switching reactions.

[17] E. Kochanski and E. Constantin, *J. Chem. Phys.* **87**, 1661 (1987).

[18] L. Operti, E. C. Tews, T. J. MacMahon, and B. S. Freiser, *J. Am. Chem. Soc.* **111**, 9125 (1989).

[19] M. Sanekata, F. Misaizu, and K. Fuke, to be published.

[20] H. Haberland, C. Ludewigt, H. -G. Schindler, and D. R. Worsnop, *Surf. Sci.* **156**, 157 (1985).

[21] A. Blades, P. Jayweera, M. G. Ikonomou, and P. Kebarle, *J. Chem. Phy.* **92**, 5900 (1990).